Mechanism of phytoplankton outbreaks in the western part of the inner Ariake Sea during winter

南浦, 修也

Mechanism of phytoplankton outbreaks in the western part of the inner Ariake Sea during winter

Department of Earth System Science and Technology
Interdisciplinary Graduate School of Engineering Sciences
Kyushu University

Naoya Minamiura

February 2023

Acknowledgements

Firstly, in carrying out my research, I would like to appreciate to Professor Yuji Sugihara and Assistant Professor Soichi Yamaguchi for their great supervision and support. I am also grateful to Professor Naoki Hirose for his constructive comments. I would like to express my gratitude to Professor Nobuya Hayashi for his valuable comment. Also, I would like to appreciate the secretary Ms. Arizumi for teaching and helping my laboratory work.

I would like to thank the members of my laboratory for their kind helping my laboratory life.

I would like to appreciate for Saga Prefectural Ariake Fisheries Research and Development Center for providing observation data and supporting field observation. My thanks are also presented to Dr. Kei Kimura and Dr. Kazuhiro Yoshida at Saga University for their invaluable advice on my study and providing the information on *Skeletonema* spp. in Ariake Sea.

Finally, I am especially grateful to my parents for their support my student life.

Table of contents

Chapter 1
Introduction

1.1 Background

Phytoplankton play an important role as primary producers supporting marine ecosystems, and this primary production accounts for about 50% on Earth (Field et al. 1998). However, some phytoplankton species lead to phytoplankton outbreaks which damage fisheries and aquaculture resources in the world (Burkholder 1998; Sellner et al. 2003), being called red tide or Harmful Algal Bloom (HAB). The phytoplankton outbreaks have been occurred in Japan, especially in coastal areas, such as Tokyo Bay (Yoshida et al. 2011), Seto Inland Sea (Imai et al. 2006) and Yatsushiro Sea (Onitsuka et al. 2015). Thus, investigation of the environmental factors related to the phytoplankton outbreaks is important for conservation and management of the resources.

The Ariake Sea, the target sea area of this thesis, located in the northwestern part of Kyushu island, Japan, is a semi-enclosed sea with size of 18 km wide, 96 km length, 1700 km^2 in area, and 20 m depth in average (Fig. 1.1a). The eastern coast in Ariake Sea has seven first-class rivers (Chikugo, Kase, Rokkaku, Yabe, Kikuchi, Shira, and Midori river in Fig. 1.1a). The inner area, which is the field of this research, is a very shallow sea area with depth of 10 m or less in a wide range. Here tidal amplitude is large, reaching a maximum of 6 m at spring tide. Along with that, the tidal flow is very strong, so the water is very turbid due to the resuspension of seabed mud. This environment generates vertically uniform water temperature and salinity, and low transparency in water column by the suspended sediment (Koh et al. 2006).

In the Ariake Sea, a large-scale aquaculture of seaweed, *Porphyra yezoensis* (named “Nori”

in Japanese) has been conducted on a large-scale from autumn to winter in shallow coastal area (Fig. 1.1a). During the period, Fig. 1.1b shows a certain group of nets on which the seaweed grows and poles that support the nets are spaced by about 100 m or less apart from each other (photographs of the seaweed aquaculture spreading in the mouth of the Rokkaku River). This seaweed is one of the important fishery resources and has been traditionary used in many Japanese foods for a long time in Japan. The seaweed has been cultivated in coastal regions by aquaculture other area in Japan, such as Seto Inland Sea, Mikawa Bay and Tokyo Bay. The production volume is 60% of the total production volume in Japan, which is the largest (Ministry of Agriculture, Forestry and Fisheries 2016). Therefore, it is recognized as an important aquaculture area for seaweed. There are two ways of conducting this seaweed aquaculture in the Ariake Sea (Fig. 1.2). Type-A seaweed aquaculture which is consisted of pole, rope and seaweed net have been conducted in shallow coastal areas including tidal flat (dark gray area in Fig. 1.1a), and Type-B seaweed aqua-culture which is consisted of small buoy, rope and seaweed net have been conducted in deeper sea areas off the coast (light gray area in Fig. 1.1a).

Since about 30 years ago, phytoplankton outbreaks have been frequently occurred in the seaweed aquaculture field of the inner Ariake Sea from autumn to winter (Matsubara et al. 2011), which cause color bleaching of the seaweed due to nutrient depletion and economic damage to the seaweed farming industry (Yamaguchi et al. 2014; Matsubara et al. 2022). These phytoplankton outbreaks have been mainly dominated by diatom and often occurred in the western area of the inner Ariake Sea (red hatched-area in Fig. 1.1a, Matsubara et al. 2011) at the first neap tide after the annual minimum water temperature dropped below 10.0 ℃ (Katano et al. 2013; Matsubara et al. 2016, 2018). Some studies have reported that the mechanism of

these phytoplankton outbreaks have resulted from such as improvement in light environment in water column during neap tide by field observation (Tanaka et al. 2004; Ito et al. 2013; Matsubara et al. 2018), stratification associated with river discharge or weakening of vertical mixing during neap tide (Matsubara et al. 2018), and advection of water mass including high concentration of phytoplankton cell from Shiota and Kashima River estuary (Yamaguchi et al. 2017, 2019, 2020). However, the mechanism of phytoplankton outbreaks in the western part of the inner Ariake Sea during winter remains unclear. Revealing this mechanism is an important issue that provide useful information for the conservation and management of aquaculture resources.

In order to investigate the generation mechanism of phytoplankton outbreaks in the western part of the inner Ariake Sea, field observations have been conducted by using vessels (Ito et al. 2013; Yamaguchi et al. 2017, 2019, 2021; Matsubara et al. 2018). However, a lot of efforts and cost are required for the vessel observations to capture the phytoplankton dynamics spatially and temporally. Additionally, the existence of the seaweed aquaculture facilities (the nets and poles) makes it difficult for research vessels to navigate at high speed. Thus, in-situ vessel observations should be carried out in combination with other more detailed observations. One of the observation methods satisfying this requirement is a continuous mooring observation (Wihsgott et al. 2019). This observation makes possible to capture phytoplankton dynamics during short term period.

The continuous mooring observation provide high-resolution temporal information but hardly provide spatial one. Satellite observations for sea surface chlorophyll-a concentration have often been used to spatially grasp phytoplankton outbreaks (Mathews 2011; Odermatt et al. 2012; Blondeau-Patissier et al. 2014). However, for satellite observation, since the seaweed

has almost the same chlorophyll-a pigment as that of phytoplankton (Ariga 1974) and, as mentioned above, seaweed nets are laid out at spatially short intervals, the satellite observations, if used, must have very high data resolution of 100 m or less (equal to the width of the ship navigation route) to separate the phytoplankton-derived chlorophyll-a pigment concentration from that of the seaweed. At present, the satellite observation with the highest resolution of 250 m and short observation frequency of a few days is made by Second generation GLobal Imager (SGLI) aboard the Global Change Observation Mission-Climate (GCOM-C) satellite (Urabe et al. 2018; Tanaka et al. 2018). Therefore, it is difficult to spatially grasp the phytoplankton distribution even with this satellite observation during the aquaculture season. There are satellites having much higher spatial resolution, such as Landsat (30 m) and Sentinel (10 m), however, they are designed basically for land observations and have a revisit time of 5-16 days. Thus it is not satisfactory for these satellite sensors to have reliable measurements of the ever-changing phytoplankton outbreaks. This suggests that we need the establishment of a new high spatial resolution observation technique to replace satellite observations.

Environmental data obtained from field observations are usually limited, so other approach should to be combined to investigate mechanism of phytoplankton outbreaks. As an effective approach, numerical simulation has been used in some area (e.g., Sohma et al. 2022). The numerical simulation can evaluate in detail the physical and biochemical processes involved in phytoplankton growth, which are difficult to evaluate by field observations. Thus, numerical simulations are also effective to clarify the physical and biochemical environments relating to the phytoplankton outbreaks in the western area of the inner Ariake Sea.

1.2 Purpose and outline of this thesis

The phytoplankton outbreaks that occur in the western part of the inner Ariake Sea during winter cause serious economic damage by color bleaching of the seaweed. Some studies have investigated the mechanism of phytoplankton outbreaks, but this mechanism is still unclear. It seems necessary to use not only the conventional method but also a new observation method to clarify this mechanism. The purpose of this study is to reveal the mechanism of phytoplankton outbreaks in the western part of the inner Ariake Sea by using both of field observations and numerical simulations. In order to clarify the mechanism, we established a new observation approach to grasp the detailed spatial distribution of phytoplankton outbreaks, and developed a numerical ecosystem model to estimate such phenomena accurately.

The structure of this thesis is as follows. Chapter 1 described the background, purpose and structure of this thesis. Chapter 2 investigates the mechanism of phytoplankton outbreaks which occurred at the first neap tide after the annual minimum water temperature by continuous mooring observation in the western part of the inner Ariake Sea during winter. Chapter 3 newly establishes a high spatial resolution observation for sea surface chlorophyll-a concentration by the use of a Fixed-wing type Unmanned Aerial Vehicles (FUAV) equipped with two multi-spectral radiometer sensors capable of being on board for detection of upward radiance and downward irradiance in an estuary under high human influence. Chapter 4 investigates the physical environment for chronical high concentration of phytoplankton cell in the western part of the inner Ariake Sea through the numerical simulation. Chapter 5 applies an ecosystem model to investigate the chemical-biological environments favorable for the phytoplankton growth in the western part of the inner Ariake Sea during winter. Finally, we describe the summary and conclusions of this thesis in Chapter 6.

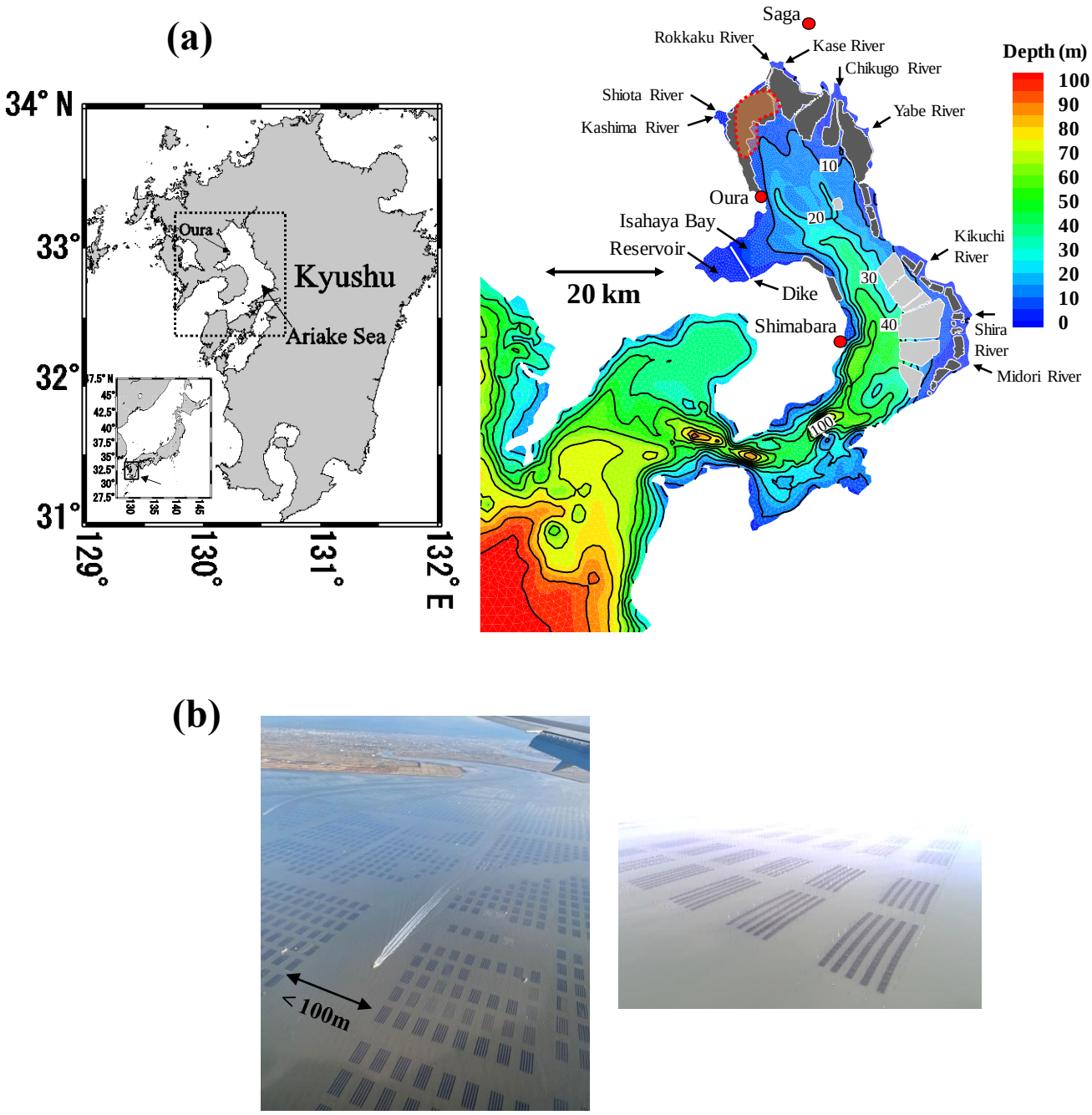

Fig. 1.1 (a) Location of Ariake Sea, seaweed aquaculture field and bottom geometry of Ariake Sea. Red hatched-area is phytoplankton outbreaks area frequently (Matsubara et al. 2011). Dark gray area indicates Type-A aquaculture facility area and light gray area indicates Type-B aquaculture facility area. (b) Aerial photos of the seaweed aquaculture.

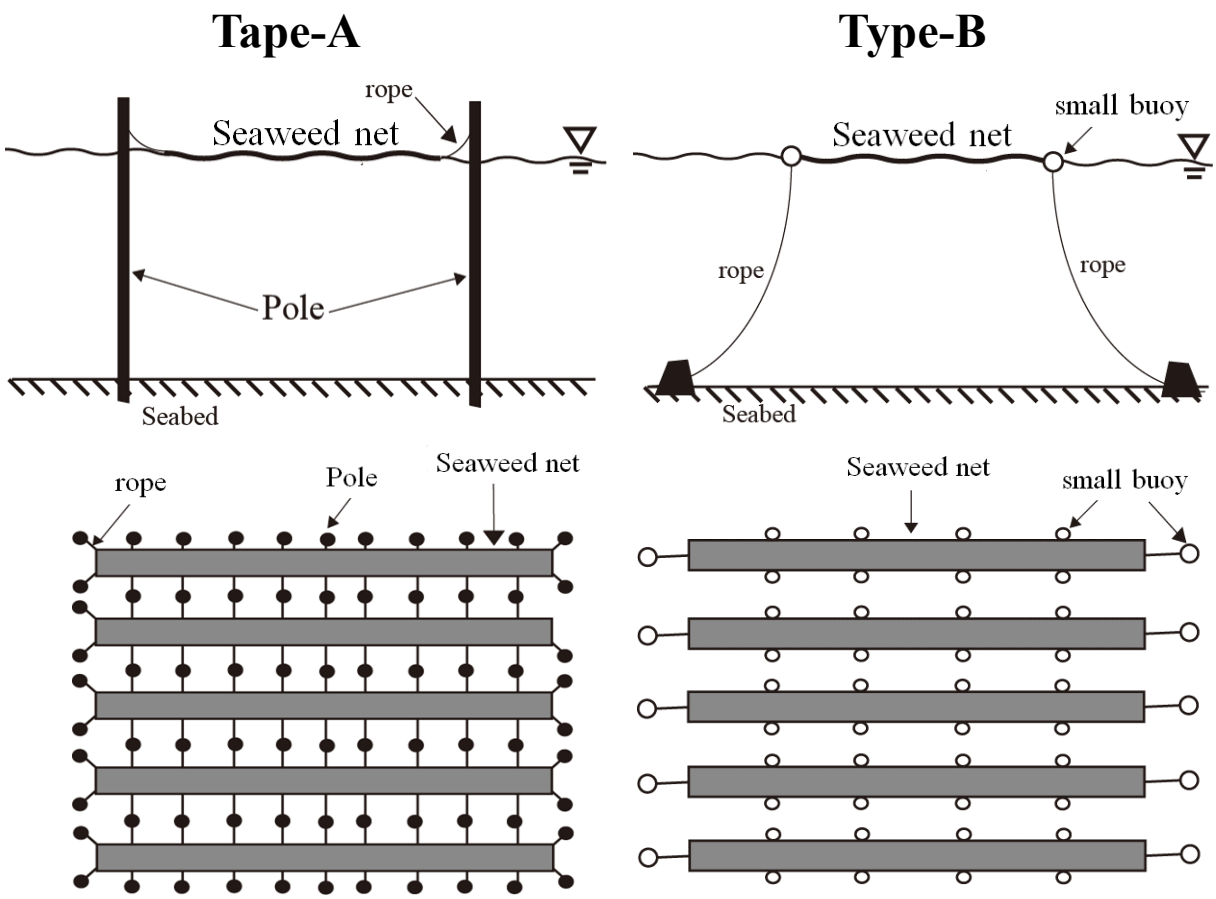

Fig. 1.2 Schematic view of the seaweed aquaculture (left panels: Type-A, right panels: Type-B). Upper panels show cross section and lower panels show overhead view for the seaweed aquaculture facilities.

References

Ariga Y (1974) Color of cultured seaweed. Our nori research 23:1-14 (**Japanese**)

Blondeau-Patissier D, Gower JFR, Dekker AG, Phinn SR, Brando VE (2014) A review of ocean color remote sensing methods and statistical techniques for the detection, mapping and analysis of phytoplankton blooms in coastal and open oceans. Prog. Oceanogr. 123:123-144. https://doi.org/10.1016/j.pocean.2013.12.008

Burkholder JM (1998) Implications of harmful microalgae and heterotrophic dinoflagellates in management of sustainable marine fisheries. Ecological Applications 8(sp1):37-62

Field CB, Behrenfeld MJ, Randerson JT, Falkowski P (1998) Primary production of the biosphere: integrating terrestrial and oceanic components. Science 281(5374):237-240

Imai I, Yamaguchi M, Hori Y (2006) Eutrophication and occurrences of harmful algal blooms in the Seto Inland Sea, Japan. Plankton and Benthos Research 1:71-84

Ito Y, Katano T, Fujii N, Koriyama M, Yoshino K, Hayami Y (2013) Decreases in turbidity during neap tides initiate late winter blooms of *Eucampia zodiacus* in a macrotidal embayment. Journal of Oceanography 69(4):467-479

Katano T, Yoshino K, Ito Y, Hayami Y (2013) Seasonal changes in phytoplankton community in the inner part of Ariake Sea: occurrence of harmful blooms in summer and winter with reference to environmental conditions. Bulletin on Coastal Oceanography 51(1):53-64 (**Japanese with English abstract**)

Koh CH, Khim JS, Ariki H, Yamanishi H, Mogi H, Koga K (2006) Tidal resuspension of microphytobenthic chlorophyll a in a Nanaura mudflat, Saga, Ariake Sea, Japan: flood-ebb and spring-neap variations. Marine Ecology Progress Series 312:85-100

Mathews MW (2011) A current review of empirical procedures of remote sensing in inland and

near-coastal transitional waters, Int. J. Remote Sens. 32:6855-6899 DOI: 10.1080/01431161.2010.512947

Matsubara T, Yoshida Y, Shuto T (2011) Trends in occurrence of phytoplankton in the Ariake Sea off Saga Prefecture during a *porphyra* (nori) cultivation period (1989-2010). Study Report of Saga Prefectural Ariake Fisheries Research and Development Center 25:21-35 (**Japanese with English abstract**)

Matsubara T, Mine T, Ito S (2016) Prediction of peak timing of blooms of *Asteroplanus karianus*, a causative organism in the bleaching of cultured nori (*Pyropia*). Nippon Suisan Gakkaishi 82(5):777-779 (**Japanese**)

Matsubara T, Mine T, Ito S (2018) Population dynamics of harmful phytoplankton causing bleaching of cultured nori in the Shiota River estuary in innermost Ariake Sea, Japan. Bulletin on Coastal Oceanography 55(2):139-153 (**Japanese with English abstract**)

Matsubara T, Shikata T, Sakamoto S, Ota H, Mine T, Yamaguchi M (2022) Effects of temperature and salinity on rejuvenation of resting cells and subsequent vegetative growth of the harmful diatom *Asteroplanus karianus*. Journal of Experimental Marine Biology and Ecology 550:151719

Ministry of Agriculture, Forestry and Fisheries (2016) The 90th Statistical Yearbook of Ministry of Agriculture, Forestry and Fisheries Japan. http://www.maff.go.jp/e/data/stat/90th/ (**Japanese**)

Odermatt D, Gitelson A, Brando VE, Schaepman M (2012) Review of constituent retrieval in optically deep and complex waters from satellite imagery. Remote Sens. Environ. 118:116-126 https://doi.org/10.1016/j.rse.2011.11.013

Onitsuka G, Aoki K, Shimizu M (2015) Meteorological conditions preceding *Chattonella*

bloom events in the Yatsushiro Sea, Japan, and possible links with the East Asian monsoon. Fisheries Science 81:123-130

Sellner KG, Doucette GJ, Kirkpatrick GJ (2003) Harmful algal blooms: causes, impacts and detection. Journal of Industrial Microbiology and Biotechnology 30:383-406

Sohma A, Imada R, Nishikawa T, Shibuki H (2022) Modeling the life cycle of four types of phytoplankton and their bloom mechanisms in a benthic-pelagic coupled ecosystem. Ecological Modelling 467:109882

Tanaka K, Kodama S, Kumagae K, Fujimoto N (2004) Variation in in situ fluorescence of phytoplankton pigments and turbidity during winter in the Chikugo River estuary, Ariake Bay, Japan. Oceanography in Japan 13(2):163-172 (**Japanese with English abstract**)

Tanaka K, Okamura Y, Mokuno M, Amano T, Yoshida J (2018) First year on-orbit calibration activities of SGLI on GCOM-C satellite, Proc. SPIE 10781, Earth Observing Missions and Sensors: Development, Implementation, and Characterization V, 107810Q (23 October 2018). DOI: 10.1117/12.2324703

Urabe T, Okamura Y, Tanaka K, Mokuno M (2018) In-orbit commissioning activities results of GCOM-C /SGLI", Proc. SPIE 10785, Sensors, Systems, and Next-Generation Satellites XXII, 107850N (25 September 2018); https://doi.org/10.1117/12.2325572

Wihsgott JU, Sharples J, Hopkins JE, Woodward E Malcolm S, Hull T, Greenwood N, Sivyer DB (2019) Observations of vertical mixing in autumn and its effect on the autumn phytoplankton bloom. Progress in Oceanography 177:102059

Yamaguchi H, Minamida M, Matsubara T, Okamura K (2014) Novel blooms of the diatom *Asteroplanus karianus* deplete nutrients from Ariake Sea coastal water. Marine Ecology Progress Series 517:51-60

Yamaguchi A, Matsubara T, Masuda Y, Mine T, Ito S (2017) The role of a high nutrient and high chlorophyll water mass in the Kashima estuary on the dynamics of winter diatom blooms in coastal areas in the inner western part of Ariake Bay. Bulletin on Coastal Oceanography 54(2):193-201 (**Japanese with English abstract**)

Yamaguchi A, Ota H, Mine T (2019) Growth environment of diatoms in turbid water in the inner western part of Ariake Bay during winter. Journal of Oceanography 75(5):463-473

Yamaguchi A, Ota H, Tsujo K, Mine T (2021) Effects of the physicochemical environment on the development and maintenance of winter diatom blooms in turbid water in the inner western part of Ariake Bay. Bulletin on Coastal Oceanography 59(1):1-10 (**Japanese with English abstract**)

Yoshida K, Chiba S, Ishimaru T (2011) Long-term variation in the wintertime diatom community structure in Tokyo Bay, Japan (1981-2000). Plankton and Benthos Research 6:195-205

Chapter 2
Investigation of phytoplankton outbreaks at the first neap tide after the annual minimum water temperature by continuous mooring observation

2.1 Introduction

The phytoplankton outbreaks have been often occurred in the western area of the inner Ariake Sea (Matsubara et al. 2011) at the first neap tide after the annual minimum water temperature (Katano et al. 2013; Matsubara et al. 2016, 2018). To reveal this mechanism, high-resolution temporal field observation by continuous mooring observation is effective. The purpose of this Chapter is to investigate the mechanism of phytoplankton outbreaks at the first neap tide after the annual minimum water temperature by continuous mooring observation in the western part of the inner Ariake Sea during winter. The structure of this Chapter is as follows. In Section 2.2, we describe the mooring continuous observation method and the data analysis method in detail. In Section 2.3, we describe the observed changes in sea conditions during the phytoplankton outbreaks after reaching the minimum water temperature, and then discuss the causes of phytoplankton outbreaks at this timing in the following Section 2.4. Finally, this Chapter finishes with a conclusion in Section 2.5.

2.2 Methods

Continuous mooring observation was carried out at Sta. H (Fig. 2.1) where phytoplankton outbreaks occurs frequently. Observed items were water temperature and salinity (INFINITY ACTW-USB by JFE Advantec Co.) at 1 m below the sea surface at 10-minute intervals from

September 29, 2020 to May 10, 2021, and turbidity (INFINITY ACLW-USB by JFE Advantec Co.) at 1 m below the sea surface from January 6, 2021 to May 10, 2021. Turbidity variation in the inner part of the Ariake Sea is dominated by the suspended sediment (SS) concentration (Hayami et al. 2015), so the turbidity value at 1 m below the sea surface (*Turb*) was converted to SS concentration (mg l^{-1}) at the sea surface using the relationship of $SS = 1.12 \times Turb + 1.67$. This formula was obtained from relationship between the turbidity value by the installed equipment and the SS concentration in the seawater sampled periodically at Sta. H. SS in water samples was filtered through a dried and weighed filter (Whatman GF/F 47 μm), and the weight of the filter with SS was measured after drying at 60 degrees for 24 hours. Then SS concentration was obtained by subtracting the weight of filter from the total weight of both the filter and SS. Vertical profiles of current in horizontal and vertical direction were measured every 10 minutes at 0.5 m intervals from the sea surface to the seabed at Sta. H from September 29, 2020 to June 17, 2021 (Aquadopp by Nortek Co.). Significant wave height was measured every 30 minutes from September 29, 2020 to June 17, 2021 (INFINITY AWH-USB by JFE Advantec Co.) and PAR intensity in the air was measured every 5 seconds from September 29 to December 16, 2020 and from February 2 to April 23, 2021 (DEFI2-L by JFE Advantec Co.) at Sta. S (Fig. 2.1). Additionally, weekly monitoring data of phytoplankton cell number of *Skeletonema* spp., *Asteroplanus karianus* and *Chaetoceros* spp., main algal species causing the discoloration of the seaweed, and dissolved inorganic nitrogen (DIN) at stations from Sta. 1 to Sta. 8 in Fig. 2.1 from October, 2020 to March, 2021 was used in the present study. Weather data including hourly wind speed and direction, air temperature and rain fall at Sta. Shimabara (32°45.3’N, 130°21.7’E in Fig. 1.1a), and air pressure, humidity, solar radiation and vapor pressure at Sta. Saga (33 ° 15.9’N, 130 ° 18.3’E in Fig. 1.1a) observed by Automated

Meteorological Data Acquisition System of Japan Meteorological Agency. The amount of cloud is obtained from the Japan Meteorological Agency's grid-point value by meso-scale model (GPV/MSM). Using the meteorological data and the sea-surface water temperature and salinity at Sta. H, net heat flux through the sea surface was calculated by the Coupled Ocean-Atmosphere Response Experiment version 3.0 (COARE 3.0; Fairall et al. 2003).

Several studies (Tanaka et al. 2004; Ito et al. 2013; Matsubara et al. 2018) reported that the improvement of the underwater light environment was important for phytoplankton proliferation. In this study, for the evaluation of that, the depth of the euphotic layer (ELD, Sverdrup 1953) was estimated based on the observational data as follows. Light intensity in the underwater was estimated by following the law of Lambert-Beer equation:

$$I_z = I_0 \cdot exp(-K_d \cdot Z) \tag{2.1}$$

where I_z, I_0 are photosynthetic active radiation (PAR) (μmol m^{-2} s^{-1}) at depth Z (m) and the sea surface, respectively. K_d is light attenuation coefficient (m^{-1}). ELD was defined as depth where the I_z equals to the threshold value of the minimum PAR intensity (μmol m^{-2} s^{-1}) required for the phytoplankton growth by photosynthesis. The sea-surface PAR intensity I_0 is converted from the solar radiation (SR) by $I_1 = 2.027 \times SR$ (r = 0.74, ANOVA, $p < 0.01$, n = 1350), where SR is global solar radiation (W m^{-2} s^{-1}) at Sta. Saga. This formula was derived from relationship between the PAR intensity in the air at Sta. S and the SR from September 29 to December 16, 2020 and from February 2 to April 23, 2021. PAR extinction coefficient K_d was calculated by the following equation using mean SS concentration from 0m to 1m below the sea surface (Fig. 2.2).

$$K_d = 0.0484 \cdot SS + 0.6501 \quad (2.2)$$

This equation was obtained from the dataset described below. The field observation was conducted at eight stations (open circle in Fig. 2.1) on April 26, 2021, April 29, and May 6 and 10, 2021. Vertical profiles of turbidity ($Turb_{RINKO}$) and PAR intensity were measured with RINKO Profiler (JEF Advantech Co.) and DEFI2-L (JEF Advantech Co.), respectively. Turbidity data was converted to SS concentration at the sea surface using the relationship of $SS = 1.69 \times Turb_{RINKO} + 1.2$. K_d was calculated by applying the exponential approximation (Eq. 2.1) to the vertical profile of the PAR intensity. As a result, Eq. (2.2) was obtained from relationship between the SS concentration and the K_d (Fig. 2.2). Wind stress (τ_w) was calculated by $\tau_w = c_d \rho_a W^2$ (Simpson and Bowers 1981) where c_d is a drag coefficient (Mitsuyasu and Honda 1982), ρ_a is air density (1.22 kg m^{-3}), and W is wind speed (m s^{-1}) at Sta. Shimabara (Fig. 1.1a). Tidal stress (τ_t) was calculated by $\tau_t = k_b \rho |u| u$, where k_b is bottom drag coefficient (= 0.0025), ρ is sea water density (kg m^{-3}) calculated with the sea-surface water temperature and salinity at Sta. H, and u is velocity (m s^{-1}) in horizontal direction vertically averaged from 1 m below the sea surface to the lowest observed layer (0.9 m at above the seabed) at Sta. H.

2.3 Results

During the mooring observation, rapid phytoplankton outbreak by *Skeletonema* spp. was confirmed at the minimum water temperature. Fig. 2.3 showed the cell number of three phytoplankton species (a: *Skeletonema* spp., b: *Chaetoceros* spp. and c: *Asterplanus karianus*)

in the surface layer, all of which were known to cause the discoloration of the seaweed, (d) surface DIN concentration, (e) PAR at the sea surface, (f) water temperature and salinity at 1 m below the sea surface, (g) water depth, (h) net heat flux at the sea surface (black line: daily running mean value; red line: average value for the last 7 days), (i) significant wave height, (j) wind stress and (k) tidal stress. Phytoplankton cell number of the three species remained low until mid-December. Thereafter *Skeletonama* spp. showed a rapid increase in mid-January, reaching over 15,000 cells ml^{-1} (Fig. 2.3a). Similar growth was not confirmed for the other two phytoplankton species (Fig. 2.3b, c). DIN concentration, limiting nutrients for phytoplankton growth (Kawaguchi et al. 2005; Katano et al. 2013), was maintained at high level of about 10 μM compared to half saturation constant for NO_3-N uptake for *Skeletonema* spp. (0.4 to 0.5 μM, Eppley et al. 1969; Lomas and Glibert 2000) before this large proliferation (Fig. 2.3d). DIN concentration decreased as the cell number increased. The intensity of PAR at the sea surface decreased toward mid-January, and then turned to increase (Fig. 2.3e). There was no particular increase in PAR prior to the increase in cell number. The salinity was stable without large fluctuations before and after the phytoplankton outbreak (Fig. 2.3f). The water temperature reached its lowest on around January 10 and thereafter started to rise (Fig. 2.3f). It can be seen that the period of increase in the cell number of *Skeletonema* spp. was close to the lowest water temperature period and the cell number reached its peak at the first neap tide immediately after the minimum water temperature. Several studies (Katano et al. 2013; Matsubara et al. 2016, 2018) reported the phytoplankton outbreaks at this timing. Present study observed such a typical occurrence pattern of phytoplankton outbreak during winter at the head of the Ariake Sea. Looking at the variation of the heat flux on the sea surface, before the water temperature reached its minimum, it frequently showed large negative values, indicating that

the sea surface was being cooled strongly (Fig. 2.3f, h). On the other hand, after reaching the minimum water temperature, the heat flux often showed positive values. This indicates a switch from sea surface cooling to heating and the phytoplankton outbreak seems to occur with this switching.

Next, we examine the relationship between phytoplankton outbreak and changes in the underwater light environment. Fig. 2.4 showed time series of the surface cell number of *Skeletonema* spp., SS concentration at the sea surface and water depth and ELD calculated by Eq. (2.1) from January to March, 2021. The dominant specie was *Skeletonema dohrnii* in *Skeletonema* spp. (Yoshida K. personal communication), so 5.4 ($\mu mol\ m^{-2}\ s^{-1}$) was used as the threshold value of the minimum PAR intensity (I_z in Eq. 2.1, Kaeriyama et al. 2011). SS concentration increased during every spring tide and decreased during neap tide (Fig. 2.4b, c). With the ELD fluctuated at M2 tidal period of about 12.4 hours, it decreased to much shallower than the water depth during spring tide (Fig. 2.4c) due to the increase in SS concentration (large extinction coefficient in Eq. 2.2). On the other hand, during neap tide, it increased to almost the same as or exceeded the water depth with the decrease of SS concentration (small extinction coefficient). Thus, this result indicates that sufficient light for the growth of *Skeletonema* spp. did not reach deep into the water column during spring tide, but did reach the depth of the water column during neap tide.

2.4 Discussion

2.4.1 Winter bloom initiation during neap tide

We observed that the phytoplankton outbreak occurred during the neap tide after reaching the minimum water temperature (Fig. 2.3). The timing of its occurrence was the same as those

reported in this field by the previous studies (Katano et al. 2013; Matsubara et al. 2016, 2018). Thus, it is likely that we observed a typical pattern of the red tide occurrence in winter. Characteristic environmental changes observed in relation to the increase in phytoplankton cell number include the change in the net heat flux from negative values to positive (switching from surface water cooling to heating) and deepening of the ELD up to water depth during the neap tide (improvement in the underwater light environment). Here we evaluate whether or not the water column was really stable during the red tide development from the temporal fluctuation of the vertical current measured by ADCP. Although the observed vertical current is not quantified, it can become a qualitative indicator of whether or not the vertical movement is active (Nortek Co., personal communication). The vertical current by upward-looking ADCP was sometimes used as an indicator of water column stability (e.g. Rippeth et al. 2001). Fig. 2.5 showed the time series of the vertical current speed at 1 m below the sea surface at high tide. Positive values indicate the velocity in downward direction. Though the current measurement near the sea surface by upward-looking ADCP are likely to be adversely affected by the sidelobe effect, we confirmed that its effect on the current at 1 m blow the sea surface was negligible (see Appendix 2.A for details). The vertical current velocity fluctuated greatly. During the phytoplankton outbreak, it settled down stably to low level (a black arrow in Fig. 2.5). To investigate the controlling factor of this variation, the relationship between net heat flux, tidal stress and wind strength (Fig. 2.3h, j, k, respectively) and the vertical current velocity were shown in Fig. 2.6. There was a statistically significant correlation between the vertical current velocity and the net heat flux ($r = -0.4$, ANOVA, $p < 0.01$, $n = 333$), but no significant correlation between the vertical current velocity and the wind/tidal stress. This result shows that the major driving force of the vertical current velocity was the heat flux at the sea surface, and the strong

vertical current observed by ADCP was considered to be intensification of thermal convective flow associated with the cooling of the sea surface. The vertical current was stably weak during the phytoplankton outbreak since the net heat flux then switched from negative to positive. Tidal and wind stresses were not correlated with the vertical flow and not specifically weakened during the phytoplankton outbreak. This fact shows that the change in the sea surface heat flux from negative to positive brought about the stability of the water column, creating a favorable condition for phytoplankton to proliferate by allowing it to stay long in the surface layer with strong light intensity.

Next, we examine why the phytoplankton outbreak occurred during the neap tide. As noted above, the water column stability was the important factor for the phytoplankton outbreak at the minimum water temperature, but this factor alone did not fully explain the phytoplankton outbreak during the neap tide. In fact, the weakening period of vertical current (a black arrow in Fig. 2.5) included spring tide (Fig. 2.3g, h), but then no rapid increase in the cell number was observed (Fig. 2.3a-c). As previous studies have already reported (Tanaka et al. 2004; Ito et al. 2013; Matsubara et al. 2018), the reason for this was the improvement of the underwater light environment at the neap tide. At the spring tides, the ELD (Fig. 2.4c) was shallow and sufficient PAR reached only the surface layer, whereas at the neap tides, the ELD deepened to or exceeded the water depth, and sufficient PAR reached the whole water column. Since the extinction coefficient of PAR was governed by the SS concentration (Eq. 2.2), the ELD fluctuation can be explained by spring-neap variation of the SS concentration (Fig. 2.4b). During the spring tide, strong tidal currents stirred up the sea bottom sediment and reduced water transparency. Therefore, even if vertical thermal convection was weak during the spring tide, phytoplankton were unlikely to proliferate. On the other hand, since the tidal current weakened during neap

tide and SS settled down to the seabed, the underwater light environment improved. Therefore, it is thought that phytoplankton was able to proliferate using sufficient light energy. The phytoplankton outbreaks during the neap tide in mid-winter occurred because two conditions (water column stability and appropriate light enviroment) were both met.

Other environmental factors that may affect phytoplankton growth includes water temperature and nutrient concentrations. The water temperature was ranged from 6.3 to 10.5 ℃ at Sta. H during the phytoplankton outbreak (Fig. 2.3e). The dominant specie was *Skeletonema dohrnii* (Yoshida K. personal communication). This specie can grow at 10.0 ℃, but the optimum water temperature was reported to be 25.0 ℃ (Kaeriyama et al. 2011). This indicates that the water temperature at the timing of phytoplankton outbreak was not necessarily suitable for phytoplankton growth. DIN concentration, limiting nutrient in winter, was maintained at around 10 μM before the cell number increased, and no temporary increase was observed before the phytoplankton outbreak (Fig. 2.3d). Since half saturation constant of *Skeletonema* spp. for NO_3-N uptake is reported to be 0.4 to 0.5 μM (Eppley et al. 1969; Lomas and Glibert 2000), the DIN concentration was kept sufficiently high for phytoplankton growth from December to just before the occurrence of the phytoplankton outbreak. It is unlikely that the variation in the DIN concentration played a role in triggering the red tide occurrence. Thus, water temperature and DIN allowed phytoplankton growth, but were not a triggering factor for the phytoplankton outbreak.

2.4.2 Phytoplankton outbreaks in the recent past and the two factors

We investigated consistency of the results of this study with the phytoplankton outbreaks occurred near the lowest water temperature in the recent past. Fig. 2.7 shows time series of cell

number of *Skeletonema* spp. and water temperature at monitoring stations (Fig. 2.1), net heat flux and tidal elevation at Sta. Oura (32°59'N, 130°13'E in Fig. 1.1a) during the aquaculture season (October to March) from fiscal year 2014 to 2018. Net heat flux was calculated in the same method using sea surface water temperature and salinity measured weekly and those in between were linearly interpolated. Though the heat flux varied annually, it often became negative toward January to early February in common. Around the minimum water temperature period (black arrows in Fig. 2.7), the heat flux became close to zero or positive and the water temperature began to rise. Then, phytoplankton cells increased in the similar manner to that observed in FY2020. This common response of the phytoplankton supports the conclusion of this study.

2.4.3 Early switching of heat flux from negative to positive

The positive/negative switching of the surface heat flux occurred in the inner Ariake Sea in the mid-winter of mid-January to early February when the water temperature was considerably low (Fig. 2.7). In the open ocean, it usually occurs from late winter to early spring (Huisman et al. 1999; Dutkiewicz et al. 2001; Follows and Dutkiewicz 2002; Waniek 2003; Taylor and Ferrari 2011; Ferrari et al. 2015; Ruiz-Castillo et al. 2019; Hopkins et al. 2021). Though our results were in common with these reports in that the phytoplankton outbreak occurred with the switching from sea surface cooling to heating (Fig. 2.3h), the timing of its occurrence was different, much earlier than those in the open ocean. Here, the factors for this difference in the switching time are discussed.

First, we discussed controlling factors of the sea surface heat flux. Time series of daily net heat flux (Q) and fluxes due to short-wave radiation (SW), long-wave radiation (LW), sensible

heat (SE) and latent heat (LA) were shown in Fig. 2.8. In most cases the net heat flux showed large negative values from October to March, the latent heat flux contributed most (i.e., enhancement of evaporation). SW decreased gradually from autumn to winter, and switched to an increase after mid-January. LW and SE showed no significant long-term trend. Next, we examined in detail the phenomenon that governed the latent heat flux. Latent heat flux (LA) is defined as follows (Fairall et al. 2003):

$$LA = \rho_a LCV(q_s - q_a) \tag{2.3}$$

where ρ_a is the air density, L is the latent heat of evaporation, C is the bulk coefficient, V is the wind strength, q_s is the sea surface specific humidity, and q_a is the atmospheric specific humidity. C is defined according to the stability of the grounding boundary layer over the sea, proportional to the difference between sea-surface water temperature (SST) and air temperature, becoming particularly small value when the air is stable (SST ≤ air temperature), and large when unstable (SST > air temperature) (Hodur 1997). Fig. 2.9 shows the time series of the LA, q_s, q_a and their difference ($q_s - q_a$), C and V, SST and air temperature, respectively. There was a good correspondence between the LA and $q_s - q_a$, C, and V. The negative LA increased with increasing specific humidity difference, wind strength, and C. Among these parameters, $q_s - q_a$ has the highest correlation with LA (r = -0.80), indicating that the specific humidity difference was most important for the LA fluctuations. The difference in the specific humidity increased with a rapid decrease in q_a, which indicated that the decrease in atmospheric water vapor pressure due to the decrease in air temperature was the cause for the negative LA. The parameter with the second highest correlation was V (r = -0.61). Decrease in q_a often occurred

with increase in wind speed. Therefore, the main controlling factors of the sea surface cooling due to LA were the decrease in atmospheric water vapor pressure due to the decrease in air temperature and the simultaneous intensification of the wind.

The inner part of the Ariake Sea is a very shallow sea area with the development of tidal flats, and during the vertical mixing period, the depth of surface mixed layer equal to the water depth at the deepest. Therefore, the heat capacity of the surface mixed layer is small, and the water temperature likely responds to heat supply in a short period of time (Fig. 2.3f, h). Since the water temperature change due to heat transport by horizontal advection was small at the observation point (Appendix 2.B), the water temperature decreased to follow the air temperature fluctuation through the enhancement of the LA (Fig. 2.9c). When the air temperature reached its lowest, the water temperature also reached its lowest value at almost the same time (Appendix 2.C). Thereafter, the air temperature often exceeded the water temperature, and then the atmosphere stabilized (decrease in C value of Eq. 2.3). This resulted in the weakening of sea surface cooling due to the LA to near zero. With the increase in SW, the heat flux turned to positive, resulting in the water column stabilization in the middle winter. Under such condition, the ELD increased during neap tides, providing a favorable light environment. Therefore, phytoplankton species such as *Skeletonema dohnii* which could grow at low temperature led to the phytoplankton outbreak. In open oceans (Dutkiewicz et al. 2001; Follows and Dutkiewicz 2002; Waniek 2003) and shelf waters (Ruiz-Castillo et al. 2019; Wihsgott et al. 2019; Hopkins et al. 2021), phytoplankton blooming associated with the stabilization of water column developed in late winter to spring (March to April, that is, spring bloom). In these sea areas, the depth of the surface mixed layer was one or two order of magnitude larger than that in the inner part of the Ariake Sea (e.g. Waniek, 2003; Ferrari et al.

2015), and thus its heat capacity was large. The water temperature variation in response to heat flux there is blunted and stabilization of the water column (switching from sea surface cooling to heating) lags from mid-winter until late winter or spring. Early switching of heat flux from negative to positive and its induced occurrence of the phytoplankton outbreak in the inner Ariake Sea reflect the difference in response characteristics of water temperature to the external heat flux.

2.5 Conclusions

In this Chapter, continuous mooring observation was conducted in the western part of the inner Ariake Sea from autumn to winter of fiscal year 2020 to reveal the mechanism of phytoplankton outbreak during the neap tide at around the minimum water temperature. As a result, it was clear that there were two important factors that played a triggering role in the phytoplankton outbreak. One is the enhancement of the water column stability along with the transition from sea surface cooling to heating after the minimum water temperature. The second is the improvement of underwater light environment due to the decrease of the suspended sediments during the neap tide. There have already been several reports on the phytoplankton outbreaks at similar time of the year (Katano et al. 2013; Matsubara et al. 2016, 2018) and the phytoplankton outbreaks confirmed in the recent past were associated with these two changes in the sea conditions. Therefore, in the inner Ariake Sea, the phytoplankton outbreak of this pattern is likely to be a typical occurrence pattern, and may be a seasonal phenomenon that can be called a winter bloom.

Appendix 2.A

Current measurement errors due to acoustic doppler reflections on the sea surface (Sidelobe phenomenon) are well known in measurements by upward-looking current meters using ultrasonic waves like ADCP used in this study. Its influence is generally remarkable within 10% of the water depth from the sea surface. To examine the sidelobe effects, the velocity data obtained by ADCP was compared with the velocity data obtained at Sta. H by an electromagnetic current meter (Compact-EM by JFE Advantec Co.). Fig. 2.10 was the comparison results of the current velocity in principle axis of M2 tidal current ellipse (counterclockwise rotation by 117.75 deg. from the east-west direction) at 1 m below the sea surface from May 5 to 10 2021. The main stream velocity obtained by ADCP was almost the same in magnitude and phase as that by Compact-EM, and it can be said that the influence of side lobe was very small at this depth.

Appendix 2.B

Here, we evaluated the effect of heat flux due to the horizontal advection on water temperature. Since there was no data that can evaluate it directly from horizontal advection flow and water temperature gradient in horizontal direction without such dataset, we investigated the effect of horizontal heat flux by evaluating the water temperature fluctuation due only to sea surface heat flux. In particular, we focused on short-term water temperature fluctuations based on the fact that phytoplankton proliferation occurred on a short time scale less than a week. We compared the sea-surface water temperature observed at Sta. H (SST_Obs) with that estimated by only sea-surface heat flux using the observed SST as its initial value. Temperature change due to sea-surface heat flux was evaluated as follows:

$$\Delta T = \frac{NHF}{\rho_0 c_p H} \tag{2.4}$$

where ΔT is water temperature fluctuation (deg hour^{-1}), *NHF* is the sea surface heat flux calculated in the same method as in Section 2.2, and ρ_0 the reference density (= 1020 kg m^{-3}), c_p the heat capacity (= 4000 J kg^{-1} deg^{-1}) and H the mixing layer depth (= water depth in this case), respectively. Fig. 2.11 showed the comparison with the water temperature after 25 hours and 50 hours (SST_25hour and SST_50hour, respectively), estimated only by the net surface heat flux, with SST_Obs as the initial value from December 10, 2020 to February 9, 2021. SST_25hour and SST_50hour agreed well with SST_Obs (MAE was 0.32 and 0.46 degree, respectively). The same result was obtained even if the estimation period was extended to 150 hours (MAE = 0.73 degree), indicating that the heat flux through the sea surface was dominant in the water temperature variation during the study period. In other words, this result indicated that the effect of heat flux due to the horizontal advection was very small.

Appendix 2.C

Here, we evaluated the synchronism of water and air temperature. Fig. 2.12 showed the time variation of water temperature at Sta. H and air temperature at Sta. Shimabara. The thick dash lines in the figures represent a curve approximated by a sine function. In order to improve the approximation accuracy of the sine curve, the data obtained in fiscal year 2021 were added to the data of FY2020 for the analysis. An inset in the figure is an enlarged view of the approximated curves of air and water temperature around their minimum values. It can be seen that the water temperature reached its lowest value almost at the same time as the air

temperature reached its lowest value.

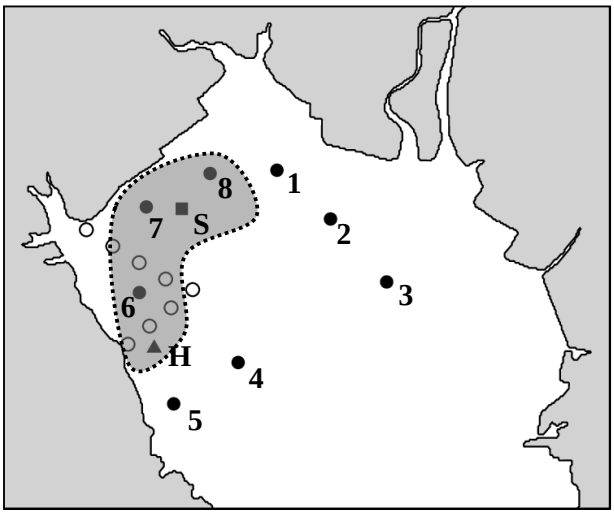

Fig. 2.1 Continuous mooring station H (black triangle) and monitoring stations of the Saga prefectural Ariake fisheries promotion center (black solid points). The open circles indicate the observation points of the SS concentration and PAR observation performed to obtain the extinction coefficient as a function of SS. Area in grey is the sea area where phytoplankton outbreaks have frequently occurred (Matsubara et al. 2011).

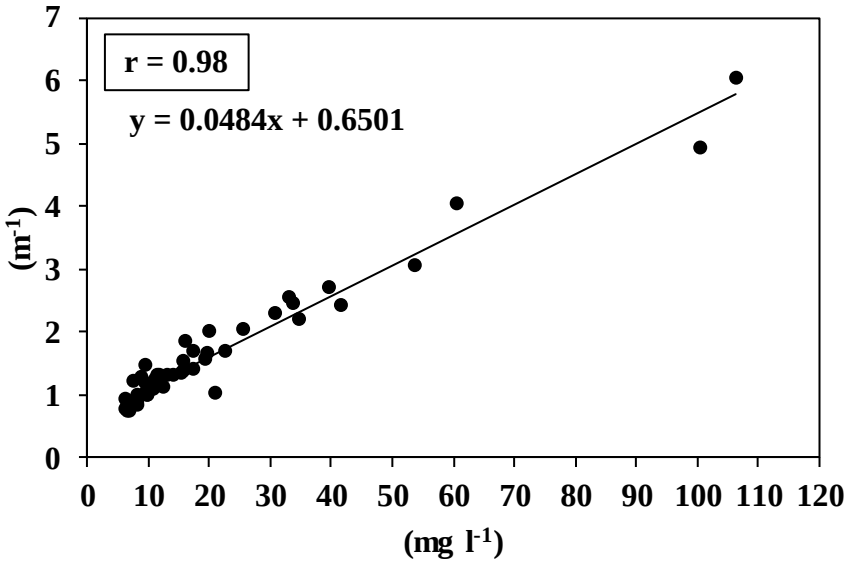

Fig. 2.2 Relationship between the SS concentration at the sea surface and the PAR extinction coefficient.

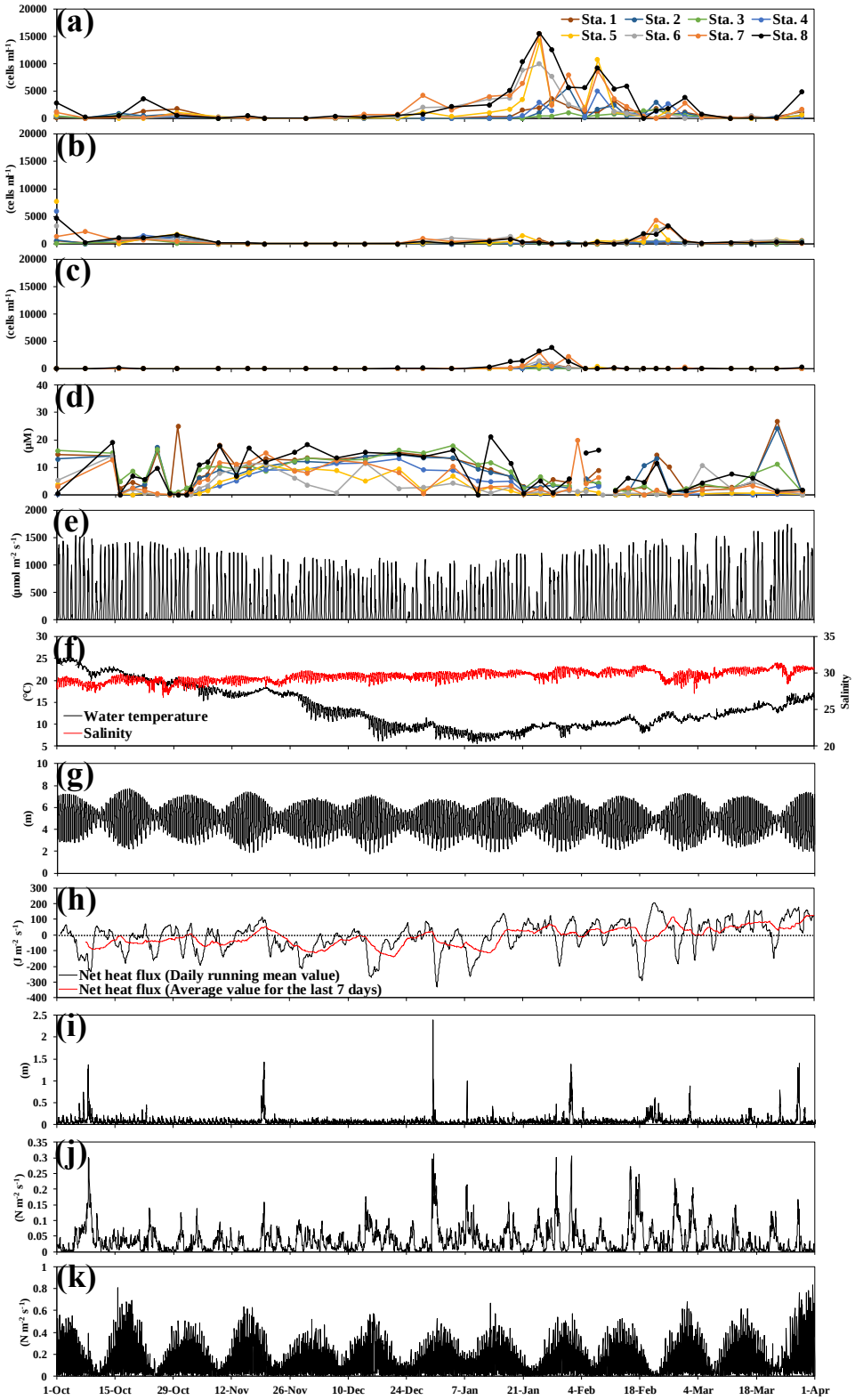

Fig. 2.3 Time series of the cell number of three phytoplankton species in the surface layer (a: *Skeletonema* spp., b: *Chaetoceros* spp. and c: *Asteroplanus karianus*), (d) surface DIN concentration, (e) PAR at the sea surface, (f) water temperature (black line) and salinity (red line) at 1 m below sea surface, (g) water depth, (h) net heat flux (black line is daily running mean value and red line is average value for the last seven days) at the sea surface, (i) significant wave height, (j) wind stress and (k) tidal stress from October, 2020 to March,

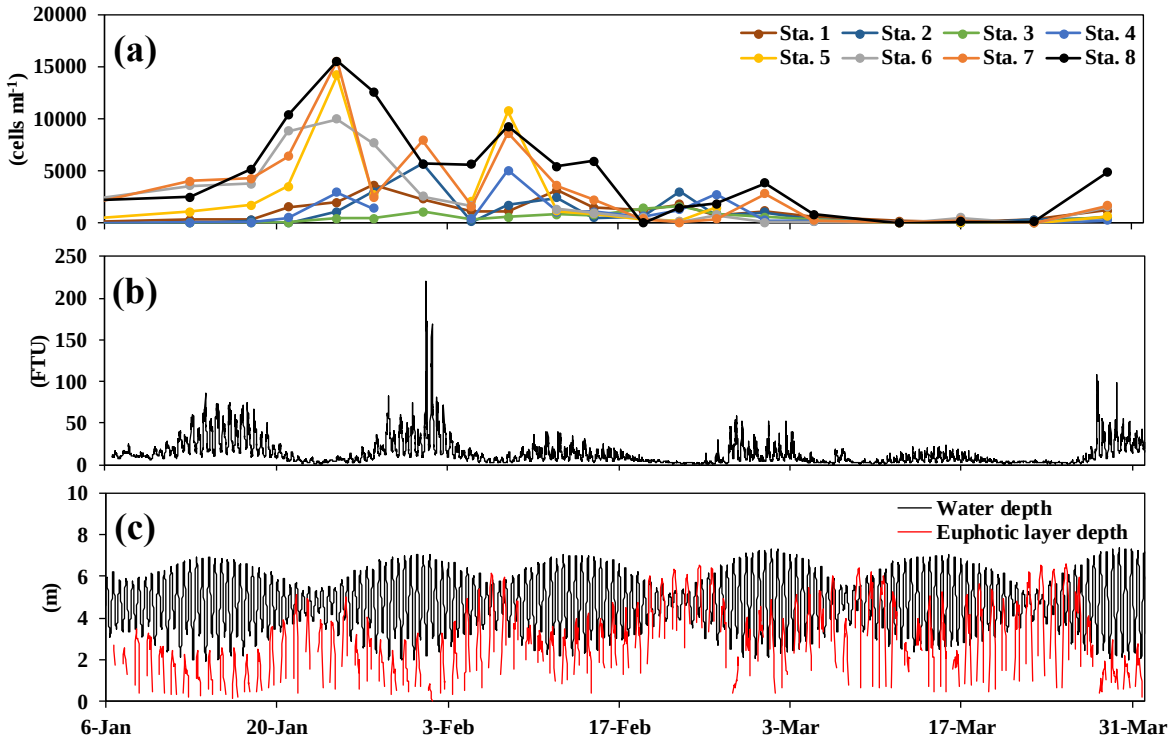

Fig. 2.4 Time series of (a) the cell number of *Skeletonema* spp., (b) SS concentration at the sea surface, (c) water depth (black line) and euphotic layer depth (red line) calculated by Eq. (2.1) from 6 January to 31 March, 2021.

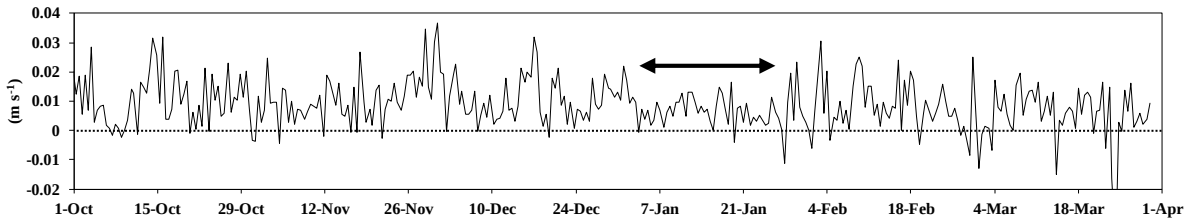

Fig. 2.5 Time series of the vertical current velocity at 1 m below the sea surface at high tide from October, 2020 to March, 2021. The period indicated with the black arrow indicates that the vertical current was weakened.

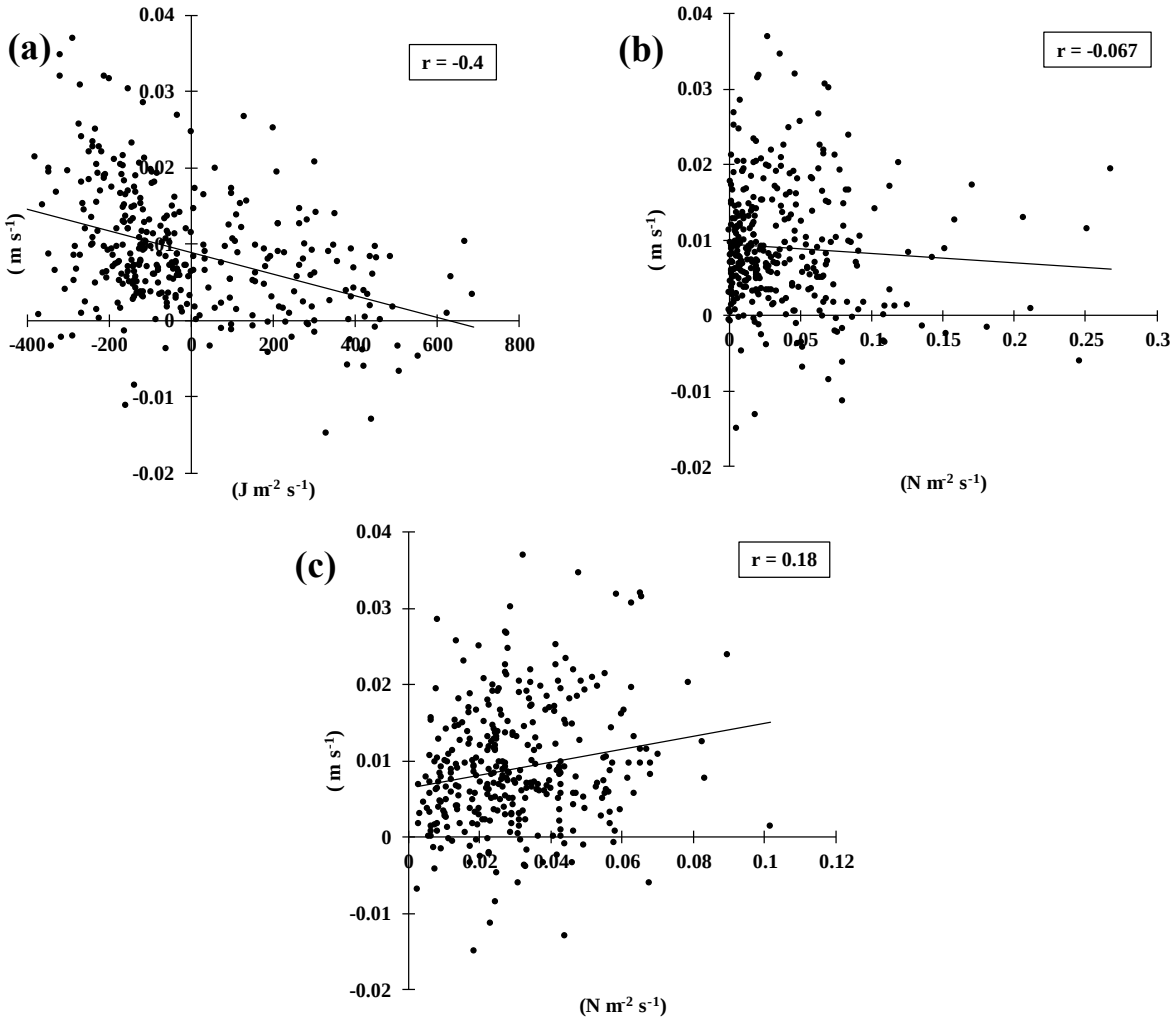

Fig. 2.6 Relationship between the vertical velocity at 1 m below the sea surface observed by upward-looking ADCP and (a) the hourly net heat flux, (b) wind stress and (c) tidal stress.

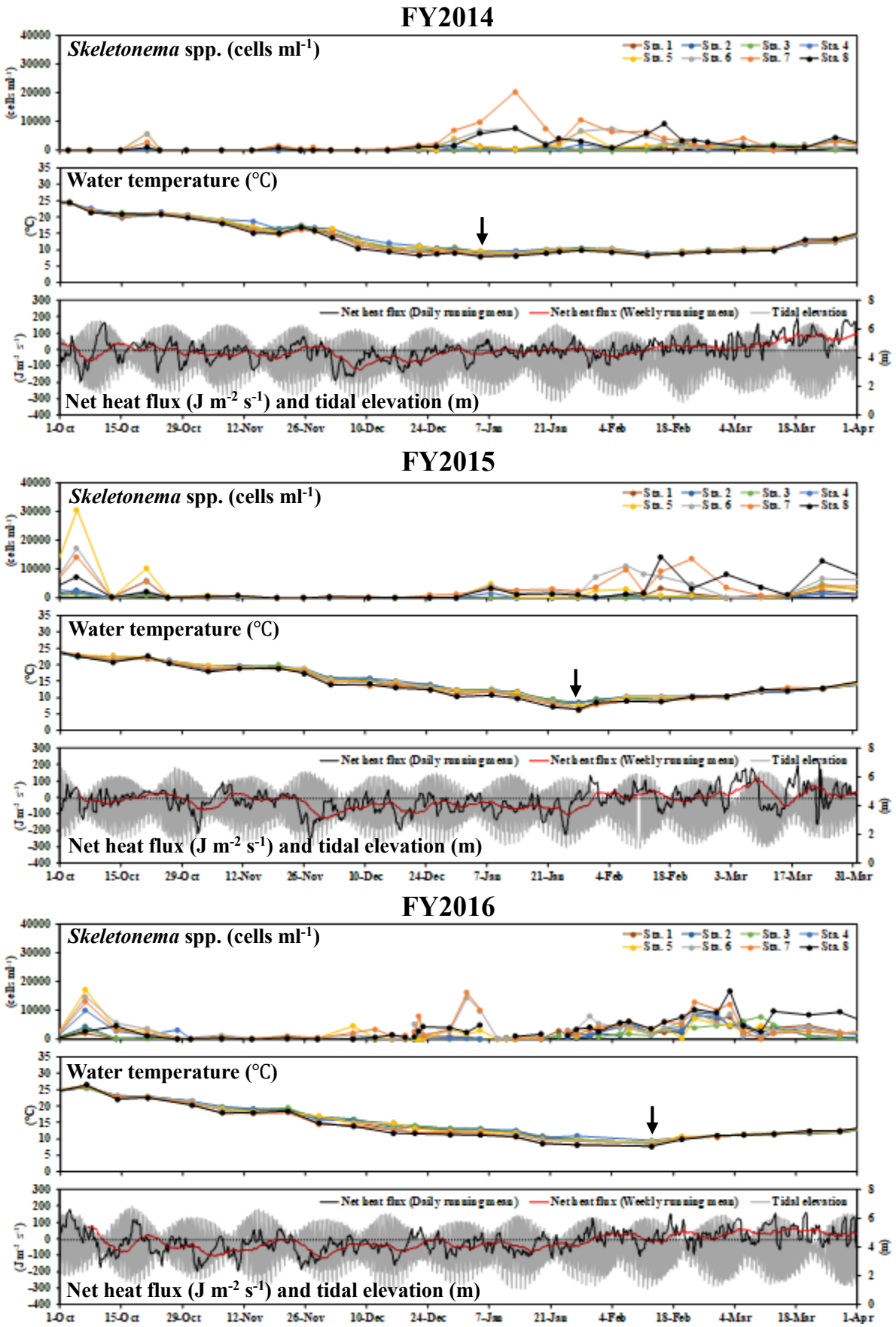

Fig. 2.7 Time series of cell density of *Skeletonema* spp., water temperature, net heat flux and tidal elevation during the aquaculture season (October to March) of five fiscal years from 2014 to 2018 (FY2014 to FY2018). Black arrows are the minimum water temperature.

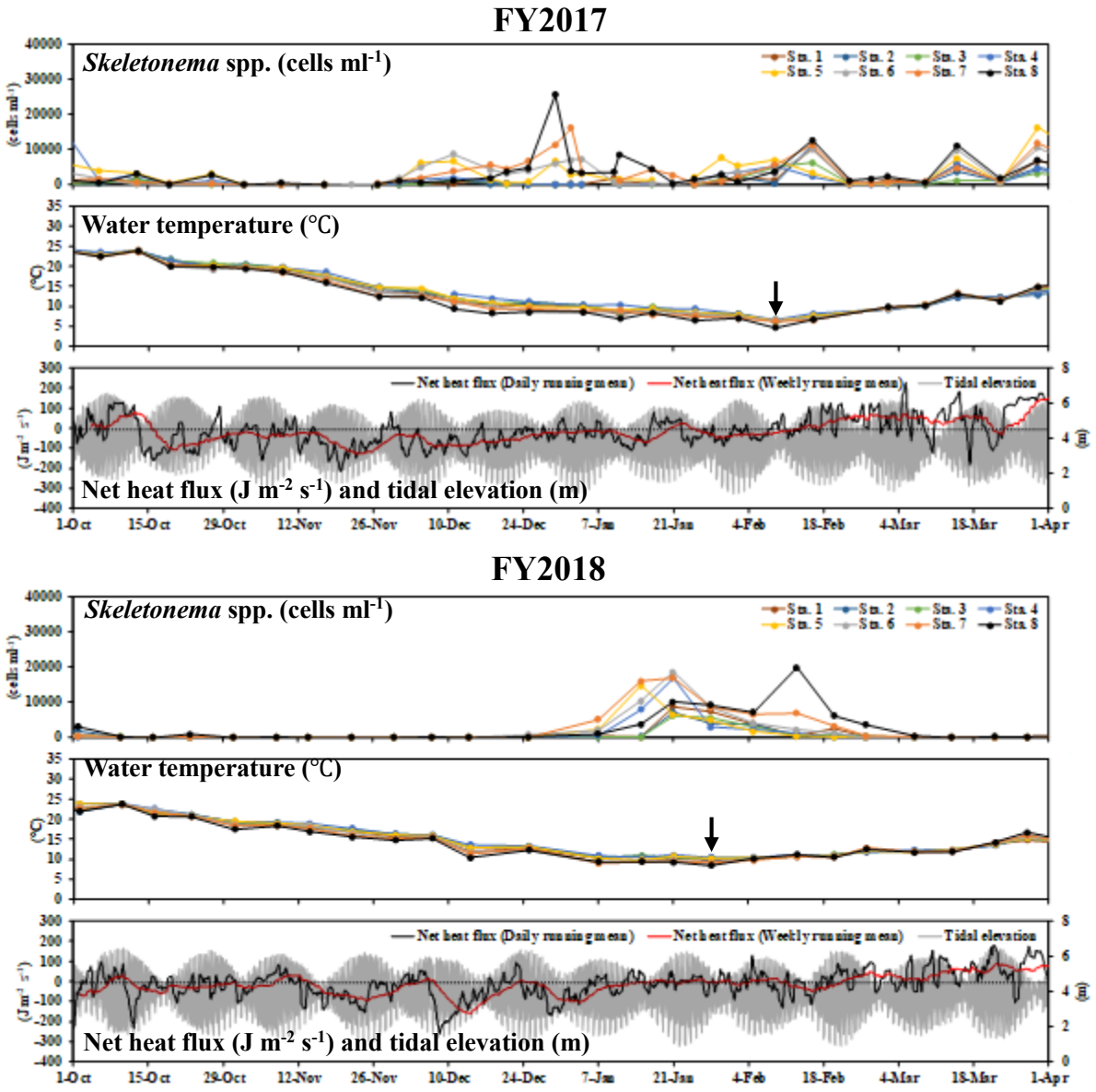

Fig. 2.7 (continued)

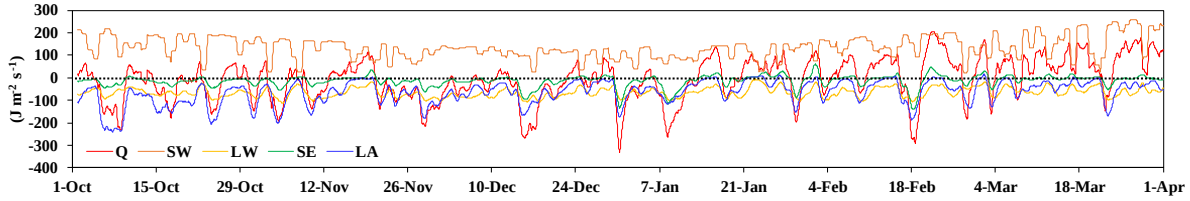

Fig. 2.8 Time series of daily net heat flux (Q) and fluxes due to short-wave radiation (SW), long-wave radiation (LW), sensible heat (SE) and latent heat (LA) from October, 2020 to March, 2021.

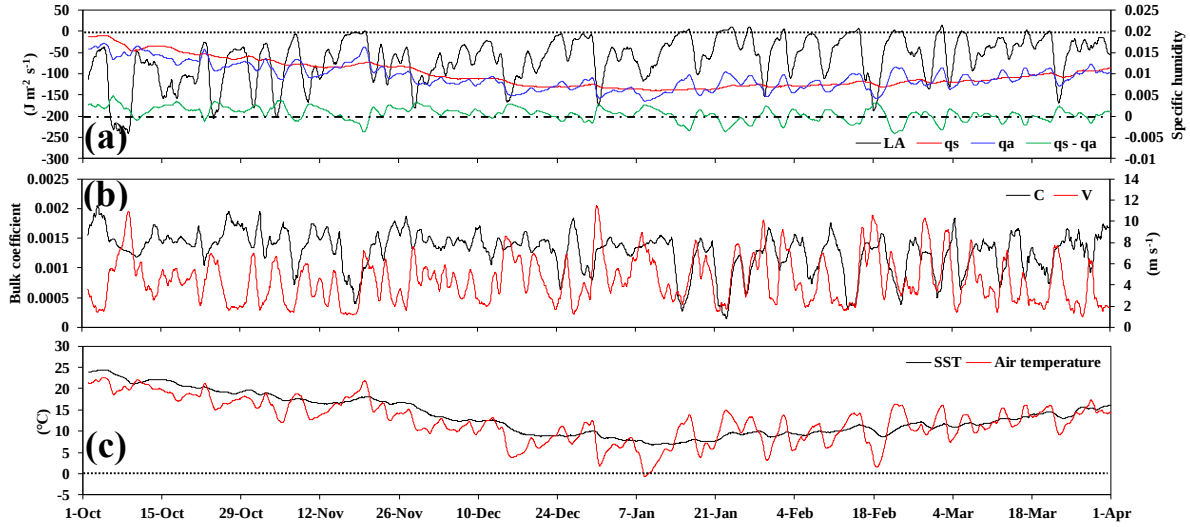

Fig. 2.9 Time series of (a) the LA, q_s, q_a and their difference ($q_s - q_a$), (b) C and V, (c) SST and air temperature from October, 2020 to March, 2021.

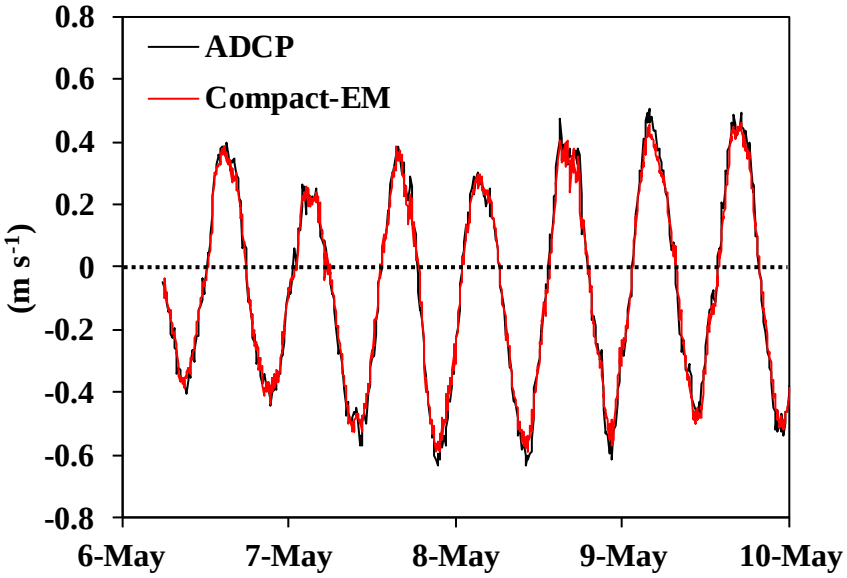

Fig. 2.10 Time series of the current velocity for ADCP and Compact-EM in principle axis of M2 tidal current ellipse (counterclockwise rotation by 117.75 deg. from the east-west direction) at 1 m below the sea surface at Sta. H from May 5 to 10 2021.

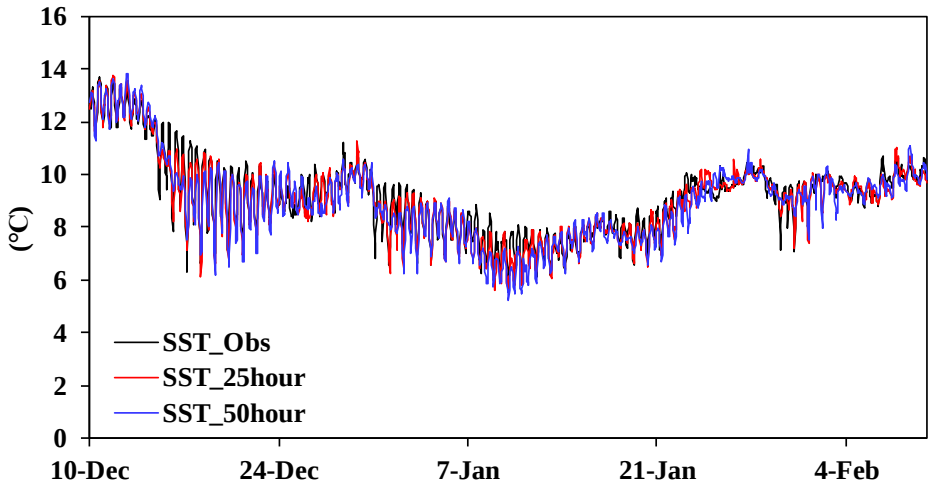

Fig. 2.11 Time series of SST_Obs, SST_25hour and SST_50hour from December 10, 2020 to February 9, 2021.

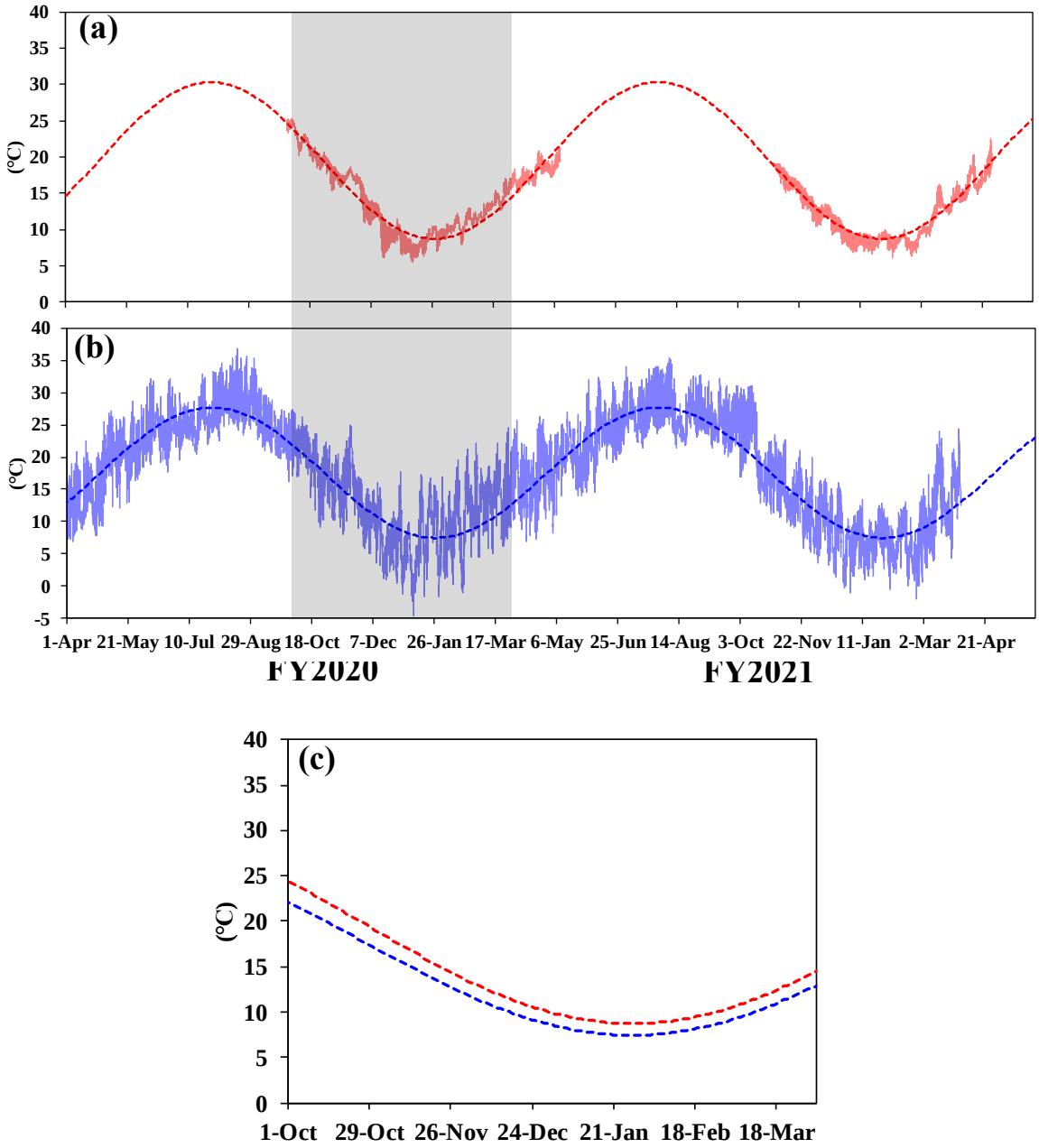

Fig. 2.12 Time series of (a) the water temperature at Sta. H, (b) air temperature at Sta. Shimabara (solid lines are raw data and thick dashed lines are curves approximated by sine function), and (c) an enlarged view of the approximated curves of the air and water temperature around their respective minimum value.

References

Dutkiewicz S, Follows M, Marshall J, Gregg W (2001) Interannual variability of phytoplankton abundances in the North Atlantic. Deep-Sea Research II 48:2323–2344

Eppley RW, Rogers JN, McCarthy JJ (1969) Half-saturation constants for uptake of nitrate and ammonium by marine phytoplankton. Limnology and Oceanography 14:912-920

Fairall CW, Bradley EF, Hare JE, Grachev AA, Edson JB (2003) Bulk parameterization of airsea fluxes: updates and verification for the COARE Algorithm. Journal of Climate 16:571-591

Ferrari R, Merrifield ST, Taylor JR (2015) Shutdown of convection triggers increase of surface chlorophyll. Journal of Marine Systems 147:116-122

Follows M S. Dutkiewicz S (2002) Meteorological modulation of the North Atlantic spring bloom. Deep-Sea Research II 49:321–344

Hayami Y, Maeda K, Hamada T (2015) Long term variation in transparency in the inner area of Ariake Sea. Estuarine, Costal and Shelf Science 162:290-296

Hodur RM (1997) The Naval Research Laboratory's Couples Ocean/Atmosphere Mesoscale Prediction System (COAMPS). Monthly Weather Review 125:1414-1430

Hopkins JE, Palmer MR, Poulton AJ, Hickman AE, Sharples J (2021) Control of a phytoplankton bloom by wind-driven vertical mixing and light availability. Limnology and Oceanography 66:1926-1949

Huisman J (1999) Critical depth and critical turbulence: Two different mechanisms for the development of phytoplankton blooms. Limnology and Oceanography 44(7):1781-1787

Ito Y, Katano T, Fujii N, Koriyama M, Yoshino K, Hayami Y (2013) Decreases in turbidity during neap tides initiate late winter blooms of *Eucampia zodiacus* in a macrotidal embayment. Journal of Oceanography 69(4):467-479

Kaeriyama H, Katsuki E, Otsubo M, Yamada M, Ichimi K, Tada K, Harrison PJ (2011) Effects of temperature and irradiance on growth of Strains belonging to seven *Skeletonema* species isolated from Dokai Bay, southern Japan. European Journal of Phycology 46(2):113-124

Katano T, Yoshino K, Ito Y, Hayami Y (2013) Seasonal changes in phytoplankton community in the inner part of Ariake Sea: occurrence of harmful blooms in summer and winter with reference to environmental conditions. Bulletin on Coastal Oceanography 51(1):53-64 (**Japanese with English abstract**)

Kawaguchi O, Yamamoto T, Matsuda O, Hashimoto T (2005) Evaluation of various environmental factors on the nutrient uptake competition between nori laver and planktonic diatoms in Ariake Bay, Japan. Oceanography in Japan 14(3):411-427 (**Japanese with English abstract**)

Lomas MW, Glibert PM (2000) Comparisons of nitrate uptake, storage, and reduction in marine diatoms and flagellates. Journal of Phycology 36:903-913

Matsubara T, Yoshida Y, Shuto T (2011) Trends in occurrence of phytoplankton in the Ariake Sea off Saga Prefecture during a *porphyra* (nori) cultivation period (1989-2010). Study Report of Saga Prefectural Ariake Fisheries Research and Development Center 25:21-35 (**Japanese with English abstract**)

Matsubara T, Mine T, Ito S (2016) Prediction of peak timing of blooms of *Asteroplanus karianus*, a causative organism in the bleaching of cultured nori (*Pyropia*). Nippon Suisan Gakkaishi 82(5):777-779 (**Japanese**)

Matsubara T, Mine T, Ito S (2018) Population dynamics of harmful phytoplankton causing bleaching of cultured nori in the Shiota River estuary in innermost Ariake Sea, Japan. Bulletin on Coastal Oceanography 55(2):139-153 (**Japanese with English abstract**)

Mitsuyasu H, Honda T (1982) Wind-induced growth of water waves. Journal of Fluid Mechanics 123:425-442

Rippeth TP, Fisher NR, Simpson JH (2001) The cycle of turbulent dissipation in the presence of tidal straining. Journal of Physical Oceanography 31(8):2458-2471

Ruiz-Castillo E, Sharples J, Hopkins J (2019) Winddriven strain extends seasonal stratification. Geophysical Research Letters 46:13244–13252

Simpson JH, Bowers D (1981) Models of stratification and frontal movement in shelf seas. Deep-Sea Research I 28(7):727-738

Sverdrup HU (1953) On conditions for the vernal blooming of phytoplankton. ICES Journal of Marine Research 18(3):287-295

Tanaka K, Kodama S, Kumagae K, Fujimoto N (2004) Variation in in situ fluorescence of phytoplankton pigments and turbidity during winter in the Chikugo River estuary, Ariake Bay, Japan. Oceanography in Japan 13(2):163-172 (**Japanese with English abstract**)

Taylor JR, Ferrari R (2011) Shutdown of turbulent convection as a new criterion for the onset of spring phytoplankton blooms. Limnology and Oceanography 56(6):2293-2307

Waniek J (2003) The role of physical forcing in initiation of spring blooms in the northeast Atlantic. Journal of Marine Systems 39:57–82

Chapter 3

Establishment of a new remote chlorophyll-a retrieval approach and grasping spatially phytoplankton outbreaks by a fixed-wing type unmanned aerial vehicle

3.1 Introduction

Matsubara et al. (2011) reported that phytoplankton outbreaks have been often occurred in the western area of the inner Ariake Sea (red hatched-area in Fig. 1.1a). However, detailed information about the spatial spread of phytoplankton has been unclear in this area. Such spatial information is important for revealing mechanism of phytoplankton outbreaks. Satellite observation of sea surface chlorophyll-a concentration often used to spatially grasp phytoplankton outbreaks is an effective method, but this method is difficult to apply in the inner Ariake Sea (see Chapter 1). Thus, establishment of a new high spatial resolution observation to replace satellite observation is needed.

Unmanned Aerial Vehicles (UAVs or drones) have been rapidly developed in recent years, and emerged to be a practical remote sensing method for environmental monitoring. The advantages of UAV include low cost, flexibility in space and time unaffected by cloud coverage (Hassan et al. 2019; Cheng et al. 2020; Li et al. 2021), and high resolution from the low altitude undisturbed by atmospheric scattering (Del Pozo et al. 2014; Zeng et al. 2017). Therefore, the UAV application extends to fields such as environment protection (Fallati et al. 2019, Kako et al. 2020), disaster relief (Erdelj et al. 2017) and agricultural production (Kim et al. 2019). These advantages suggest that UAVs would provide an alternative appropriate for the remote monitoring of phytoplankton outbreaks from low altitudes. As an example of application to the

marine environment, some studies that employed a digital camera directly used the recorded pixel values from UAV images to develop their water quality estimation model (e.g. Su and Chou 2015). In these studies, multicopter-type (rotory wing) consumer UAVs were used. While multicopter-type UAVs can fly very stably, such as being able to fly in a stationary state, it should be noted that they have the weakness in their flight ability that they cannot fly long distances and long hours necessary to capture the spatial map of the phytoplankton outbreak with horizontal scale of O (>10 km) in coastal waters. Apart from the multicopter-type UAVs, fixed-wing type UAVs (FUAV, hereinafter) enable longer distances and longer flight times than those of multicopter-type UAVs. However, there are only a few examples of its application in the sea areas to grasp the spatial map of phytoplankton outbreaks (Shang et al. 2017; Cheng et al. 2020). Furthermore, previous FUAV studies in estuaries are supported by scant coincident direct field measurements. Then, the generality of the models developed for chlorophyll-a concentration estimation is questionable and there is no validated model in coastal waters from FUAVs. Because of the water quality complexity of high-turbid and high productive estuarine/coastal waters such as the Ariake Sea, retrieving biogeochemical variables with reasonable accuracy using FUAV is a challenging task.

The purpose of this Chapter is to establish a new high spatial resolution observation of sea surface chlorophyll-a concentration by the use of a FUAV equipped with two multi-spectral radiometer sensors capable of being on board for detection of upward radiance and downward irradiance in an estuary under high human influence, and grasp spatially detailed information for phytoplankton outbreaks in the western part of the inner Ariake Sea during winter. The structure of this Chapter is as follows. In Section 3.2, the planning of FUAV flight and the methodology for spectroscopic radiation data treatment are then given. In Section 3.3, the

development of the chlorophyll-a estimation algorithm with concurrent field observations are presented. Section 3.4 discuss the relationship between error factors and the estimation accuracy in remotely estimating the chlorophyll-a concentration. Section 3.5 provides conclusion from this Chapter.

3.2 Methods

3.2.1 Evaluation of the seaweed effect on spectral radiance

In this study, we measure spectral irradiance from the sky and spectral radiance from the water (described in detail later). When the cultured seaweed enters the field of view of the sensors onboard the FUAV, since the seaweed has various pigments (including chlorophyll-a) and unique absorption characteristics for various wavelength components of light (Ariga 1974), it should affect the reflectance of spectral water-leaving radiance and then the accuracy of estimating the phytoplankton-derived chlorophyll-a concentration. In order to evaluate the effect of the seaweed on the upward spectral radiance, we measured the downward spectral irradiance and upward spectral radiance 1 m above the sea surface with/without the seaweed net on February 12 and 19, 2020 at stations shown in Fig. 3.1 (closed black circles).

3.2.2 Fixed-wing type UAV

In this study, a fixed-wing type UAV, named OPTiM Hawk V2 (Fig. 3.2), developed by OPTiM Corporation (https://www.optim.com/) was used. Flight performance is briefly described in Table 3.1. OPTiM Hawk V2 has maximum speed of 140 km hour^{-1}, maximum altitude of 3000 m, maximum loadable weight of 2000 g, and maximum flight time of 90 minutes. This type of UAV allows for long flight duration and high speed, which makes it

possible to investigate the phytoplankton outbreak in a wide area of the inner bay size on the order of 10 km or larger.

There were a total of five flights, all of which took place during the aquaculture season (December 7 and 18, 2020, January 5, 2021, February 10 and 24, 2022). Weather and sea conditions at the time of the flights (solar zenith angle, significant wave height at Sta. S (Fig. 3.1) observed with INFINITY-WH of JFE Advantec Co., LTD, daylight hour, wind speed at Sta. Shiroishi observed by Automated Meteorological Data Acquisition System: AMeDAS of Japan Meteorological Agency) was shown in Table 3.2. The sky was sunny on December 7 and 18, 2020, February 24, 2022 and cloudy on January 5, 2021 and February 10, 2022. Waves on all the flights was calm with no white cap observed in the field. The flight was carried out within two hours at high tide. OPTiM Hawk V2 can automatically fly along the preset GPS (Fig. 3.1) after takeoff. As will be described later, sensors mounted on the FUAV optically measures the upward water-leaving radiance affected by absorptive constituents in the underwater including chlorophyll-a pigment of phytoplankton. Since the cultivated seaweed also has the similar chlorophyll-a pigment to that of phytoplankton (Ariga 1974), it should affect the characteristics of upward water-leaving radiance (described in detail in the next section). To avoid the effect of the seaweed-derived chlorophyll-a pigment on the radiance, we set the flight route to over sea routes laid in the aquaculture field for the navigation of the aquaculture vessels (Fig. 1.1b, Fig. 3.1) where the seaweed aquaculture was not conducted. Its width is about 100 m or smaller. The FUAV took off and landed at the airfield in Shiroishi (marked with a cross in Fig. 3.1). A land base station was set up here to operate the FUAV. Fig. 3.3 shows a conceptual diagram of the FUAV observation during five flights. The flight altitude was set to about 100 m above the sea level during the flights considering obstacles such as observation towers and based on the

local regulation of maximum flight-altitude (<150 m). The flight speed was set to about 20 m sec^{-1}. Notification was given to fishermen and related parties regarding the implementation of the overflight observations with the FUAV.

3.2.3 Spectral radiance/irradiance observation

Spectral characteristics of water-leaving radiance were used to estimate the chlorophyll-a concentration in the sea-surface layer. To detect it, we used two spectral photosynthetically active radiation (PAR) meter (UPRtek's PG200N) onboard the FUAV. One was placed on the back of the FUAV and the other on the abdomen with the sensors facing vertically to measure upward radiance and downward irradiance (mW m^{-2}) in the visible light and near infrared range (350 nm to 800 nm, 1 nm resolution) at 5-second interval.

The integration time for the two sensors could be automatically adjusted according to light intensity in a range of 100 μs–1000 ms with default setting of 60 ms determined. It conforms to JIS C 1609-1: 2006 general type AA class (DIN 5032 Part 7 Class B), and was well calibrated by the manufacturer before the observation. Measurement accuracy is ± 5%. It is compact and lightweight (190 mm long, 81.7 mm wide, 29.5 mm high, and weighs about 280 g), making it suitable for mounting on the FUAV. With flight speed of 20 m s^{-1} and 5-second observation interval, present observation method obtained the data of ground resolution of 100 m. Horizontal distance of the FUAV movement during one observation of spectral irradiance/radiance in 60 ms was 1.2 mm.

The upwelling radiance detected by PG200N includes not only the water-leaving radiance, but direct reflection light at the air-sea interface (sun glint; Sathyendranath and Morel 1983; Sathyendranath et al. 1987; IOCCG 2000) and scattered irradiance from the atmosphere (Fig.

3.4). In order to reduce the influence of sun glint, an opaque plastic cylinder with inner diameter of 16 mm and a length of 57 mm was attached to the upward and downward-looking sensors (Fig. 3.5). An absorption sheet of light (Super Black IR by Systems Engineering Inc.) was attached to the inside of the cylinder to prevent light scattering inside the cylinder. This sheet can absorb 98.5% of incident light intensity at spectral wavelengths from 250 nm to 380 nm and 99.0% from 380 nm to 780 nm. Opening angle (viewing angle of the sensor) was adjusted to about 22.8 degrees. Based on this angle and the flight height (100 m), the observation range of the sea surface was about 40 m in diameter centered on the sensor. Considering the sun zenith angle during the FUAV flights shown in Table 3.2 and the suppression of direct incident of the sea-surface reflected light by this cylinder with the absorption sheet, it is noteworthy that the effect of the sun glint on the observation accuracy is considered to be negligible in all our FUAV dataset. Water-leaving radiance is almost unaffected by the scattered irradiance from the atmosphere as a little atmosphere is between the sensor and the sea surface because of the low altitude flights (Del Pozo et al. 2014; Zeng et al. 2017; Shang et al. 2017). These settings possibly lead to the acquisition of high quality data of the spectral reflectance.

In the actual flights, it is quite conceivable that the aircraft may deviate from the preset route or be greatly tilted by temporary strong winds. In addition, large floating objects and ships on the flight route may enter the sensor's field of view. Outliers may be measured in such cases. To exclude such outliers when deriving the estimation algorithm of chlorophyll-a and drawing a spatial map of the sea surface chlorophyll-a concentration, the following post processing for the obtained data was carried out. First, the mean value and standard deviation (σ) were calculated using the spectral data at each wavelength within 30 seconds from the targeting time. When the target data were separated by more than $\pm$ 3σ from the mean value, they were

discarded from the analysis (so-called 3σ cut treatment).

3.2.4 Derivation of conversion algorithm

Using the radiance/irradiance data after removing the outliers, the conversion algorithm for estimating the sea-surface chlorophyll-a concentration was developed as follows. In near-shore waters like the Ariake Sea with total suspended particulate matter (TSM) in large quantity, high TSM would strongly affect the spectral reflectance (*Rrs*) signal in the blue-green band because of its strong light absorption (Tzortziou et al. 2007). Then, large errors are expected in retrieval of chlorophyll-a concentration based on the algorithm developed for open ocean using this color band (e.g. Gordon and Morel 1983). This study adopted regional and specific algorithms based on red and near-infrared (NIR) wavelengths proposed for improving chlorophyll-a retrievals in highly turbid, coastal and inland waters (e.g.; Dall'Olmo and Gitelson 2006; Tzortziou et al. 2007; Gitelson et al. 2009) as follows.

$$\text{Chl-a} \propto [R_{rs}^{-1}(\lambda_1) - R_{rs}^{-1}(\lambda_2)] \cdot R_{rs}(\lambda_3) \tag{3.1}$$

Rrs is the spectral reflectance of three specific wavelengths $(\lambda_1, \lambda_2, \lambda_3)$ and calculated as follows:

$$R_{rs}(\lambda) = \frac{L_w(\lambda)}{E_s(\lambda)} \tag{3.2}$$

where $L_w(\lambda)$ and $E_s(\lambda)$ are the upward radiance of wavelength λ from the sea water and the downward irradiance from the sky, respectively. *Rrs* reflects the spectral reflection of

characteristics of underwater substances. In terms of physical meaning, λ_1 is the wavelength at which absorption of light by phytoplankton is maximum and should be in the red range around 670 nm. λ_2 is the wavelength strongly related to TSM concentration as well as to absorption by all materials except chlorophyll-a and should be in the range around 710 nm. λ_3 is the wavelength in the near-infrared red range of the spectrum around 750 nm which is closely related to back-scattering by suspended particles (Gitelson et al. 2009). This algorithm was tested and validated in estimating chlorophyll-a in turbid productive waters such as lakes with variable optical properties (Dall'Olmo and Gitelson 2006) and estuarine waters where chlorophyll-a varied widely (Gitelson et al. 2008, 2009). To select the optimal three wavelengths to estimate the surface chlorophyll-a concentration using the three-wavelength model, for the wavelength (350 nm to 800 nm) measured by PG200N, all combinations were applied to the three-wavelength model, and the correlation coefficients between the values calculated by the Eq. (3.1) and the chlorophyll-a concentration contained in the sea-surface water obtained by the field observation were calculated. Finally, the three wavelengths with the highest correlation were selected. To assess the consistency between the estimated chlorophyll-a concentration by the three-wave length model and the in-situ measured values, in addition to the correlation coefficient (r), the root mean squared error (RMSE) and averaged unbiased absolute percentage difference (UPD, Hooker et al. 2002) were calculated. In this study, the data obtained in fiscal year 2020 (December 7 and 18, 2020, January 5, 2021) was used to develop the three-wave length model, and those in fiscal year 2021 (February 10 and 24, 2022) were used to validate the model.

3.2.5 Marine survey by ships with the FUAV overflights

Simultaneous ship surveys were carried out with the FUAV overflights. The observation stations on the flight route were shown with open circles in Fig. 3.1. Sea surface water was sampled using a bucket with handle by three research vessels as soon as the FUAV passed the stations. A total of 65 water samples were collected and analyzed immediately for chlorophyll-a and TSM concentration on the same day. The chlorophyll-a concentration was determined using a spectroscope after extraction with DMF (dimethylformamide). The measured chlorophyll-a concentration ranged from 2.0 to 38.1 μg l^{-1}. To measure the amount of TSM, water samples with the TSM was filtered through a dried and weighed filter (Whatman GF/F 47 μm), and the weight of the filter with TSM was measured after drying at 60 degrees for 24 hours. The amount of TSM was obtained by subtracting the weight of filter from the total weight of both the filter and TSM. TSM concentration was in the range of 3.6 to 104.8 mg l^{-1}. Vertical profiles of water temperature, salinity, fluorescence intensity, and turbidity were measured using RINKO Profiler / AAQ-RINKO (JEF Advantech Co., Ltd, hereinafter referred to as CTD observation) at the time of the sea-surface water sampling.

3.3 Results

3.3.1 Effect of seaweed on spectral radiance

First, we show the effect of the cultivated seaweed on the water-leaving spectral radiance. Fig. 3.6 shows changes in the spectral reflectance due to the seaweed on February 12, 2020 at stations shown in Fig. 3.1 (closed circles). The spectral reflectance in the sea area without the seaweed (solid lines) had a peak at around 580 nm and gradually decreased toward shorter and longer wavelength band, which were quite similar in magnitude and shape to typical reflectance spectra collected in turbid waters (Dall'Olmo and Gitelson 2006; Gitelson et al. 2000; Schalles

2006). The reflectance spectrum above the seaweed (broken lines) was totally different from the ones without the sea weed. The reflectance was greatly reduced in the range of 350 nm to 700 nm, which means that PAR was strongly absorbed by the seaweed. On the contrary, the light reflectance over 700 nm (near infrared band, NIR) became larger over the seaweed than those without the seaweed. The cultured seaweed (*Porphyra yezoensis*) here has four kinds of pigments (chlorophyll-a, beta carotene, phycoerythrin, phycocyanin), and each prefers to absorb different wavelength bands of light (Ariga 1974). Then, the seaweed strongly absorbed the light at the wavelength shorter than 700 nm. Regarding the strong reflection at the wavelength band above 700 nm over the seaweed, Mumby et al. (1997), Dekker et al. (2005) and Pasqualini et al. (2005) reported that seagrasses had high reflectance in NIR part of the spectrum. Therefore, strong reflection over 700 nm shown in Fig. 3.6 was due to the seaweed having such reflection properties. It can be easily imagined from these results that when the observation field of view of the sensor includes the seaweed aquaculture area, the observed water-leaving spectral radiance characteristics change significantly compared to that without the seaweed and then it should be difficult to optically estimate the phytoplankton-derived chlorophyll-a concentration from such data. This is the reason for setting FUAV's flight route to the seaweed-free ship navigation roots in this study (Fig. 3.1). The FUAV's performance and high degree of freedom in the route selection made such observations of the present study possible.

3.3.2 Chlorophyll-a concentration estimation using the three-wavelength model

An estimation algorithm for the sea surface chlorophyll-a concentration was developed

based on the three-wavelength model (Eq. 3.1) with the spectral radiance and irradiance data observed three times in fiscal year 2020. Fig. 3.7 shows the frequency distribution of chlorophyll-a concentration, TSM concentration and salinity in seawater samples collected by the research vessels during the FUAV flights. The sampled waters contained wide-range of chlorophyll-a and TSM concentration (mean chlorophyll-a: 8.8 μg l^{-1}, TSM: 20.8 mg l^{-1}) that varied by a factor of about 10. Fig. 3.8 shows the priority rate and cell number of four representative phytoplankton (*Skeletonema* spp., *Cheatoceros* spp., *Asteroplanus karianus* and *Akashiwo sanguinea*) on the days closest to the FUAV flight dates at Sta. H and Sta. S (Fig. 3.1). It can be seen that the dominant species of phytoplankton changes on each flight day.

The spectral irradiance, spectral radiance, and its reflectance (*Rrs* in Eq. 3.2) on January 5, 2021 at four stations (Sta. C1 to Sta. C4 in Fig. 3.1) were shown in Fig. 3.9. Values in parentheses next to each station name indicate the concentration of chlorophyll-a pigment in the surface water at each station. The downward irradiance intensity had a peak at 450 nm to 500 nm wave length, and the upward radiance at 550 nm to 600 nm, and each decreases toward the shorter and longer wavelength. Differences in reflectance (*Rrs*) between these stations were small up to wavelength of about 550 nm and appeared around the wavelength over 550 nm. There was a large valley around 670 nm to 680 nm, especially at the Sta. C2 and C4 with high chlorophyll-a concentration. This wavelength corresponds to the wavelength preferably absorbed by the chlorophyll-a pigment (Gurlin et al. 2011; Odermatt et al. 2012).

Conversion algorithm from the spectral reflectance to chlorophyll-a concentration is derived as follows. The three wavelengths ($\lambda_1, \lambda_2, \lambda_3$) in Eq. (3.2) most highly correlated with the surface chlorophyll-a concentration were 672 nm, 691 nm and 722 nm, respectively. The following equation was established between the values (*X*) calculated by Eq. (3.2) with the *Rrs*

at the three wavelengths and the chlorophyll-a concentration in the sea-surface water.

$$Chl\text{-}a\_e = 134.91 \cdot X + 4.21 \quad (3.3)$$

Here, *Chl-a_e* is an estimated chlorophyll-a concentration based on the three-wavelength model. Fig. 3.10 shows comparison result between the *Chl-a_e* and the chlorophyll-a concentration in the sea-surface water in fiscal year 2020 (black circles). The red dashed line in the figure is one-to-one straight line. A high correlation was obtained between the two (r = 0.85, RMSE = 3.35 μg l^{-1}, UPD = 29.1), indicating that the chlorophyll-a concentration in the surface water was successfully estimated by the remote sensing method with FUAV using the three-wavelength model. Also shown with blue triangles was the comparison result for the dataset obtained two times in fiscal year 2021 using the reflectance at the same three wavelengths and Eq. (3.2). Similar estimation accuracy was confirmed for the dataset also in this year 2021 under different sea conditions and species dominance (Table. 3.2, Fig. 3.8), proving the validity of this estimation method (RMSE = 3.48 μg l^{-1}, UPD = 19.0).

3.3.3 Horizontal distribution of chlorophyll-a concentration

We succeeded in capturing the patchy phytoplankton distribution by the FUAV overflights in the inner part of the Ariake Sea under the large-scale seaweed aquaculture environment.

The spatial distributions of sea-surface chlorophyll-a concentration on December 7 and 18, 2020, and January 5, 2021, February 24, 2022 are shown in Fig. 3.11. On December 7, 2020, we captured the patchy distribution of high chlorophyll-a concentration in the west dominated by *A. sanguinea* (Fig. 3.8), and on December 18, the distribution of high concentration

dominated by *Skeletonema* spp. instead of *A. Sanguinea* appeared almost in the same area and on January 5, 2021, it expanded further along the northern coast. It was confirmed later that the chlorophyll-a concentration further increased and the phytoplankton outbreak was occurred, leading to the discoloration of the seaweed. The distribution shown in Fig. 3.11b, c seems to capture the initial distribution of the phytoplankton outbreak. On February 24, 2022, the chlorophyll-a concentration dominated by *Chaetoceros* spp. is particularly high off the Shiota River mouth. Matsubara et al. (2018) reported based on long-term field monitoring data of phytoplankton cells that the cell number in the western part of the head of Ariake Sea tended to be high even if the dominant species were different. The spatial distributions in Fig. 3.11 are consistent with this report. The present method succeeded in estimating chlorophyll-a concentration with high accuracy regardless of the difference in the dominant species.

3.3.4 Representative layer of the water-leaving radiance

We examined which layer of underwater with chlorophyll-a concentration was mainly observed by the present method. For that, the correlation coefficients (r) between the fluorescence intensity vertically measured by the CTD observation and the estimated chlorophyll-a concentration by Eq. (3.3) were calculated. Fig. 3.12 shows the vertical profile of the correlation coefficients every 0.5 m from 0.5 m to 4 m below the sea surface. Up to 2 m depth, r was very high value exceeding 0.8. In layers deeper than 2 m, the correlation gradually weakened. Fig. 3.13 shows the vertical distribution of chlorophyll fluorescence intensity obtained at Sta. D1, C4 and D2 (Fig. 3.1) during three flights in fiscal year 2020. The data on December 7 at Sta. C4 was missed. At Sta. D1, which is the station closest to the shore, the distribution was almost uniform vertically, but at Sta. C4 and Sta. D2, it was almost uniform in

the surface layer up to 2 m, but in layer deeper than 2 m, it differed a little from those in the upper layer. Such characteristics of the vertical chlorophyll-a structure were reflected in the variation of the correlation coefficient in Fig. 3.12. Therefore, the spatial distribution shown in Fig. 3.11 was considered to reflect the chlorophyll-a concentration in the layer from 0 m to 2 m below the sea surface. If the chlorophyll-a concentration changes continuously or irregularly from the sea surface, attention should be paid to the underwater layer in which the obtained spectral radiance best reflect the chlorophyll-a concentration.

3.4 Discussion

Unmanned aerial vehicles (UAVs) have recently shown more and more great value for environmental monitoring, due to their spatio-temporal flexibility in time and space, low cost, and very importantly, high spatial resolution from the low flying height, to map detailed phytoplankton distributions even under heavy clouds. In this study, we adopted a fixed-wing type UAV, instead of the multicopter-type UAV that has been frequently used in the environmental monitoring programs (Del Pozo et al. 2014; Su and Chou 2015; Zeng et al. 2017). Compared to the multicopter type UAV, a fixed-wing type UAV was possible to fly for a long time and a long distance so that it was able to cover the horizontal scale of the phytoplankton outbreaks in the inner bay area. We acquired spectroscopic characteristics with resolution of 1 nm and chlorophyll-a concentration in the surface layer. Our measurements were performed over a wide range of bio-optical water characteristics (e.g. chlorophyll-a concentration in the range from 2.0 to 38.1 μg l^{-1}, TSM in 3.6 to 104.8 mg l^{-1}) with sunny and cloudy weather conditions (Table 3.2) and several phytoplankton species dominated (Fig. 3.8). The fact that we succeeded in estimating the sea surface chlorophyll-a concentration with high accuracy despite

the differences in the weather conditions and the dominant species offered an unprecedented opportunity to examine the effectiveness of the phytoplankton outbreaks remote sensing method using the fixed-wing type UAV. According to National Aeronautics and Space Administration (NASA), the desired absolute error of estimated chlorophyll-a using satellite's ocean color data is 35% for coastal waters (McClain et al. 2006; Moore et al. 2009). GCOM-C / SGLI mission also has a goal of 35%, as an estimation system for chlorophyll-a concentration (Matsuoka et al. 2021). Yang et al. (2018) utilized the available in-situ light reflectance dataset by the satellite MODIS aqua and developed a switching algorithm to reduce errors associated with the standard OC3M algorithm in the turbid waters at the head of Ariake Sea. They succeeded in reduction of the absolute error to 24.9%. The absolute error by the present method in this study was 21.4%. Compared to the estimation accuracy of these traditional methods, it was proved that the present method has sufficient estimation accuracy.

It is difficult to grasp the spatial distribution of phytoplankton outbreaks in coastal regions or inshore bays because in many cases, they have patchy or small spatial coverage in the early developmental stages, and are unpredictable and fast changing. In the Ariake Sea, phytoplankton outbreaks occur under the strong human influence of the seaweed aquaculture (Fig. 3.11), which makes it more difficult to grasp them spatially because of the restrictions on research vessel's speed and mooring points. When estimating the spatial distribution of chlorophyll-a concentration in the surface layer, ocean color information has been often used. In terms of capturing phytoplankton outbreaks in autumn and winter of the inner Ariake Sea, it is necessary to pay special attention to its spatial resolution due to the presence of the large amount of seaweed. At present, among satellites with temporal resolution of one day or several days (e.g., MERIS, MODIS, international space station), the highest spatial resolution is about

300 m, and satellites with higher spatial resolution, such as Landsat (30 m) and Sentinel (10 m) designed basically for land observations, have a revisit time of 5-16 days around Japan. Therefore, satellite data is not satisfactory for observing phytoplankton outbreaks that occur in shallow coastal areas in autumn and winter of the Ariake Sea. The application of FUAV in this study has the potential to overcome these difficulties. In this study, we succeeded in extracting phytoplankton-derived chlorophyll-a concentration with reasonable accuracy in the aquaculture area of the Ariake Sea. The method of this study can be applicable to other sea areas with various environmental problems under high human influence where high-resolution observations are required.

Error appears in remotely estimating the chlorophyll-a concentration in case 2 waters like that of the Ariake Sea using the water-leaving spectral radiance, in general, because of differences in dominant phytoplankton species and interference due to optically absorptive constituents (TSM and Colored Dissolved Organic Matter: CDOM) in the waters. In addition, substances in atmosphere (e.g., absorptive aerosol) and sea-surface reflection of sun light (sun glint) decreases the estimation accuracy of the chlorophyll-a concentration. In order to develop more sophisticated algorithms and obtain more accurate assessment of phytoplankton outbreak event using FUAVs, from next section, we will examine the relationship between these factors and the estimation accuracy.

3.4.1 Dependence on dominant species

We examined how the difference in dominant phytoplankton species would affect the results. The optical backscattering features of phytoplankton have been reported to change with different species (Feng et al. 2020). As shown in Fig. 3.8, three kinds of phytoplankton

dominant species appeared during the FUAV flight observation. Here, the data was divided according to the dominant species. By applying each data to Eq. (3.1) in the same way as described in Section 3.2, the selected three wavelengths ($\lambda_1, \lambda_2, \lambda_3$) and correlation coefficient: r were 670, 664, 718 and 0.66 for *A. sanguinea*, 675, 692, 752 and 0.94 for *Skeletonema* spp. and 689, 703, 755 and 0.91 for *Chetoceros* spp. It is very interesting that the three wavelengths selected for the genus *Chaetoceros* spp. and *Skeletonema* spp. which both belong to marine diatom were similar wavelength combinations, while λ_2 and λ_3 were different and correlation coefficient was low for the dinoflagellate *A. sanguinea*. This result infers that the optimal wavelength combination applied to the three-wavelength model may change depending on the dominant species. There have been several challenges for developing methods using satellite-based ocean color remote sensors to study phytoplankton functional types on broad spatial and temporal scales in the surface ocean (IOCCG 2014 and references therein; Bracher et al. 2017; Kramer et al. 2018). In the future, it may be necessary to selectively use the three optimal wavelengths depending on the dominant species in order to achieve more accurate estimation of the sea surface chlorophyll-a concentration. For that, more data needs to be collected to conclude.

3.4.2 Effects of TSM and CDOM

The influence of TSM and CDOM on the spectral reflectance should be considered. In open oceanic waters, in which absorptive constituents are dominated by phytoplankton and its originated materials, chlorophyll-a concentration is estimated using the blue and green spectral regions (e.g. Gordon and Morel 1983). On the other hand, in coastal waters, the quality of chlorophyll-a retrieval using blue-green spectral bands generally degrades because of the

absorption due to TSM and CDOM (Siswanto et al. 2013) contained in the sea water (e.g., Tzortziou et al. 2007; Dall'Olmo et al. 2005). In fact, Yang el al. (2018) reported that the waters in northern Ariake Sea was optically TSM-dominated. Many studies suggested the use of red to NIR band-ratios for the chlorophyll-a retrieval in such optically complex coastal waters (e.g., Gurlin et al. 2011; Tiwari and Shanmugam 2011; Odermatt et al. 2012) because the interference due to TSM and CDOM was assumed to be negligibly small in this spectral region (e.g. Tzortziou et al. 2007; Yang et al. 2018). Dall'Olmo and Gitelson (2006) and Gitelson et al. (2007, 2008) proposed the estimation model of chlorophyll-a concentration using three wave lengths of red to NIR (Eq. 3.1) for turbid productive waters. In this study, to select the optimum three wavelengths, all combinations of the observed spectral reflectance from 350 nm to 800 nm were applied to the three-wavelength model (Eq. 3.1) and compared the calculated values with the chlorophyll-a concentration in the sea surface water. As a result, selected three wavelengths 672 nm for λ_1, 691 nm for λ_2, and 722 nm for λ_3 were all red and NIR wavelengths. These wavelengths of λ_1 to λ_3 are close to the wavelengths pointed out by Gitelson et al. (2009) as already mentioned in Section 3.2.4, which is a very consistent result. Fig. 3.14a shows the relationship between the estimation error of chlorophyll-a concentration (deviation of *Chl-a_e* from a one-to-one straight line shown in Fig. 3.10) and TSM. The TSM concentration at the point where not measured was estimated based on the reflectance ratios of two wavelengths (564 nm and 731 nm by Villar et al. 2013 and Chen et al. 2015, described in detail in Appendix 3.A). Statistically significant relationship was not detected between the errors and TSM concentration. Therefore, it can be said that variation in TSM concentration has little influence on the estimation accuracy of chlorophyll-a concentration by the present three-wavelength model using red to NIR wavelengths.

Next, we examined impact of CDOM on the estimation accuracy. Keith et al. (2016) estimated the CDOM absorption of light ($\alpha_{\mathrm{CDOM}} = \alpha \times \mathrm{CDOM}$, α is a specific absorption coefficient of CDOM) using several datasets acquired in estuaries, coastal bays, and near shore waters along the U.S. East and Gulf coasts from 1999 to 2012. They suggested that α_{CDOM} was empirically estimated with ratio of reflectance at two specific wavelengths 665 nm and 489 nm as follows,

$$a_{CDOM} = C1 \cdot \frac{R_{rs}(665\ \mathrm{nm})}{R_{rs}(489\ \mathrm{nm})} - C2 \tag{3.4}$$

They also suggested that sea surface salinity (SSS) could be estimated using α_{CDOM} as follows,

$$SSS = C3 \cdot e^{-C4 \cdot \alpha_{CDOM}} \tag{3.5}$$

C1 to C4 are empirically-defined coefficients (1.3307, 0.1246, 33.686 and 0.374, respectively). Other studies also reported the similar relationship between the light absorption due to CDOM and two wavelengths reflectance (670 nm, 490 nm by Tiwari and Shanmugam 2011; 667 nm and 488 nm by Schaeffer et al. 2015). We obtained a statistically significant correlation between SSS at 1 m below the sea surface measured by CTD observation and those estimated by Eq. (3.5) (Appendix 3.B). This fact indicates that the relationship of Eq. (3.4) and (3.5) can be applicable to some extent in the northern Ariake Sea as well. Fig. 3.14b shows the relationship between the reflectance ratio at two wavelengths ($\mathrm{RR} = \frac{R_{rs}(665\ nm)}{R_{rs}(489\ nm)}$) and the estimation error of chlorophyll-a. It can be seen that there is no statistical relationship. Main source of CDOM in the inner bay area is fresh water inflow from land (Vodacek et al. 1997; Coble et al. 2004;

Bowers and Crett 2008; Keith et al. 2016). In winter, in the inner Ariake Sea, the volume of fresh water inflow is usually very low and as a result, horizontal SSS variation in the observation area during the FUAV flights was small (Fig. 3.7 and Fig. 3.17). Therefore, the spatial variation of CDOM was also probably small. Such sea conditions at the time of the present observations and the use of red to NIR wavelengths may have mitigated the effects of the CDOM, although it may be necessary in the future to actually measure CDOM concentration and evaluate the relationship with the estimation error.

3.4.3 Atmospheric correction

The reliability of the measured reflectance is generally hampered by the aerial scattering (Moore et al. 1999; Toratani et al. 2007; Odermatt et al. 2012; Wei et al. 2016), often due to absorptive aerosols floating in the atmosphere (Gordon, 1997; Kanayama et al. 2002). Most conversion algorithms for chlorophyll-a concentration using airborne hyperspectral measurements for higher-altitude flights (e.g., > 1 km) including satellite-derived light reflectance are applied with specific atmospheric correction modules (Toratani et al. 2007; Gao et al. 2007; Odermatt et al. 2012; Zhang et al. 2015). However, in turbid coastal waters, the performance of the atmospheric correction modules is generally very low (Gons et al. 2008; Wang et al. 2007, 2009; Tripathy et al. 2012; Yang et al. 2018) because the high turbidity of coastal waters causes the failure of the atmospheric correction algorithm based on the black pixel assumption in the near-infrared (NIR) bands (Siegel et al. 2000). Therefore, in coastal waters, atmospheric correction of ocean color images by higher-altitude flights is a challenging task (IOCCG 2010). In this study, the altitude of the FUAV during all flights was set to be about 100 m from the sea level. According to the report by Del Pozo et al. (2014), Zeng et al. (2017)

and Shang et al. (2017), water-leaving radiance was almost unaffected by the atmospheric disturbance with such low altitude flights as less atmosphere was between the sensor and the target. This is also one of the factors that led to the high estimation accuracy of the sea surface chlorophyll concentration.

3.4.4 Sun glint effect

Airborne remote sensing can be impeded by the effect of the light reflection at the sea surface: sun glint (Kutser et al. 2009). The reflected radiance due to the surface reflection does not contain any information on the underwater constituents, then resulting in the error of the estimated chlorophyll-a concentration. In this study, to prevent the downward sensor from detecting the sea-surface reflected light, we attached the cylinder (Fig. 3.5) to the sensor on the abdomen of the FUAV. Similarly, the same cylinder was attached to the sensor on the back of the FUAV. As a result, the viewing angles of both sensors are the same, 22.8 degrees (Fig. 3.3). Considering such viewing geometry and the sea condition with small waves during all flights (Table. 3.2), the sea-surface reflected light detected by the downward sensor can be estimated to be a part of the spectral irradiance detected by the upward sensor. Therefore, if the light reflectance rate on the sea surface is known, the influence of the sun glint on the upward radiance can be evaluated. Mobley (1999) examined the relationship between the reflectance rate and the viewing angle of the sensor, wind speed, and solar zenith angle. Applying the conditions of the present FUAV flights (Table 3.2) to his result, the reflectance rate can be estimated to be 0.026. Fig. 3.15 shows the relationship between the sea-surface reflected radiance calculated by multiplying the reflectance rate (0.026) and the spectral irradiance measured by the upward sensor and the radiance measured by the downward sensor at the three

wavelengths used in Eq. (3.1) (672 nm, 691 nm, 722 nm). According to this result, it can be said that the influence of the sun glint on the spectral reflectance was small at these wave lengths.

3.5 Conclusions

This Chapter attempted to establish a new remote sensing method for phytoplankton outbreaks in a turbid productive coastal water under high anthropogenic influence using the FUAV. Encouraging results were obtained that the present method had high accuracy in estimating the chlorophyll-a concentration in the sea-surface water using three-wavelength model of red to NIR with minimum interference from absorption due to CDOM, TSM and atmospheric disturbance. Spatial high-resolution observation by this method succeeded in capturing the patchy distribution of phytoplankton species. The spatial distributions of chlorophyll-a concentration taken for two years showed that the phytoplankton proliferated locally in the central region of the western part of the inner Ariake Sea in the early stage, and then it expanded further along the northern coast.

Appendix 3.A

Following Chen et al. (2015) and Villar et al. (2013), TSM was estimated based on the reflectance ratios of two wavelengths $\left(RR_{SS} = \frac{R_{rs}(731\ nm)}{R_{rs}(564\ nm)}\right)$. Using TSM concentration measured by in-situ water sampling (MTSM) and RRss at the same observation stations by FUAV overflights (ETSM), relationship between ETSM and MTSM was obtained as follows (Fig. 3.16):

$$ETSM = 112.77 \cdot RR_{SS} - 21.15 \tag{3.6}$$

Appendix 3.B

Keith et al. (2016) derived the optical algorithms for CDOM and SSS estimation as shown in Eq. (3.5) and (3.6). Substituting Eq. (3.5) into Eq. (3.6) yields the following equation:

$$SSS = C3 \cdot e^{-C5 \cdot \frac{R_{rs}(665\ \text{nm})}{R_{rs}(489\ \text{nm})} + C6} \tag{3.7}$$

Where *C5* (*C1*×*C4*) and *C6* (*C2*×*C4*) are coefficients. The relationship between the observed SSS and $e^{-\frac{R_{rs}(665\ \text{nm})}{R_{rs}(489\ \text{nm})}}$ is shown in Fig. 3.17. Although the variation was large, the correlation coefficient was 0.3747 which was statistically significant (p value = 0.012).

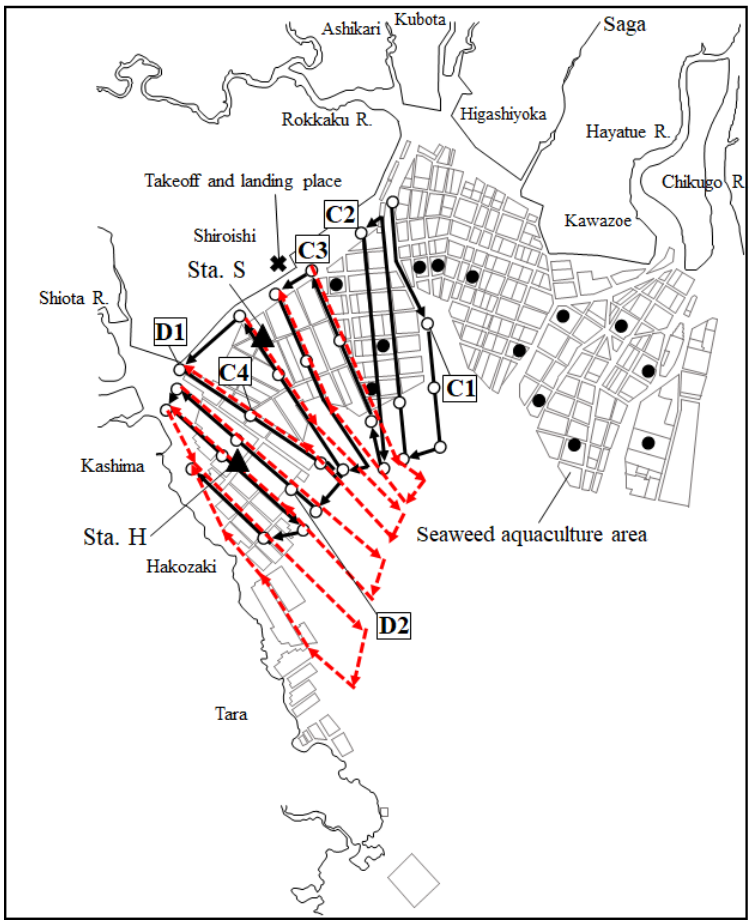

Fig. 3.1 Positional relationship between the FUAV flight routes in fiscal year 2020 and 2021 (black solid line: 2020, red dashed line: 2021) and seaweed aquaculture area. Closed black circles indicate the points where the effect of seaweed on the spectral radiance was investigated on February 12 and 19, 2020. Open circles indicate the points where water sampling and CTD observation were performed during the FUAV flights.

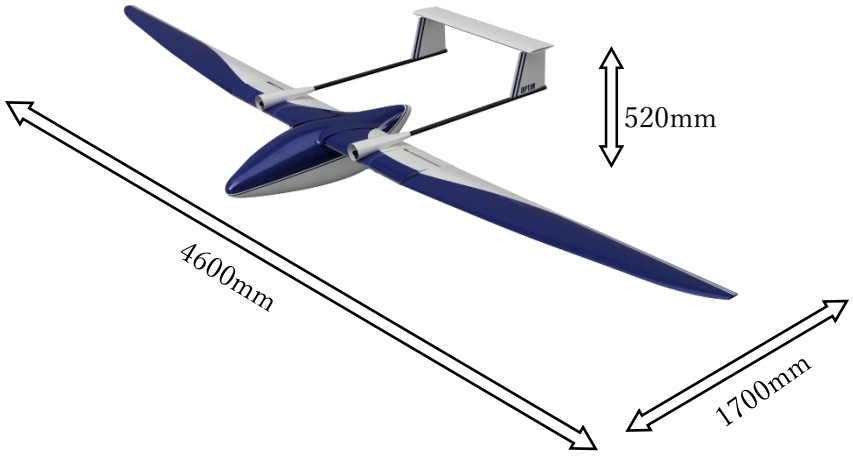

Fig. 3.2 Fixed-wing unmanned aerial vehicle used in this study: OPTiM Hawk V2 and its width, depth and height (unit: mm).

Table 3.1 Flight performance of OPTiM HAWK V2 used in this study.

	Performance
Max. speed	140 km h^{-1}
Max. altitude	3000 m
Max. mountable weight	2000 g
Max. flight time	90 min.
Flyable wind speed	< 7m s^{-1}

Table 3.2 Solar zenith angle (°), significant wave height (m), daylight hour, and wind speed (m s^{-1}) on flight time.

Date	Solar zenith angle (°)	SWH (m)	Daylight hour	Wind speed (m s^{-1})
2020/12/7 13:00	56.9	0.024	0.6	1.1
2020/12/7 14:00	61.5	0.026	0.5	1.4
2020/12/7 15:00	68.8	0.018	0.4	1.1
2020/12/7 16:00	78.0	0.025	0.6	3.1
2020/12/18 11:00	59.3	0.040	0.9	1.4
2020/12/18 12:00	56.6	0.034	1.0	1.4
2020/12/18 13:00	57.4	0.030	0.9	1.3
2021/1/5 12:00	56.0	0.054	0.4	0.8
2021/1/5 13:00	56.3	0.037	0.0	2.5
2021/1/5 14:00	60.1	0.022	0.0	4.1
2021/1/5 15:00	66.8	0.026	0.0	3.8
2022/2/10 13:00	47.8	0.083	0.0	1.3
2022/2/10 14:00	51.7	0.046	0.0	1.4
2022/2/10 15:00	58.9	0.049	0.0	4.2
2022/2/24 13:00	43.0	0.069	1.0	6.1
2022/2/24 14:00	47.3	0.070	1.0	4.6
2022/2/24 15:00	55.1	0.064	1.0	5.0

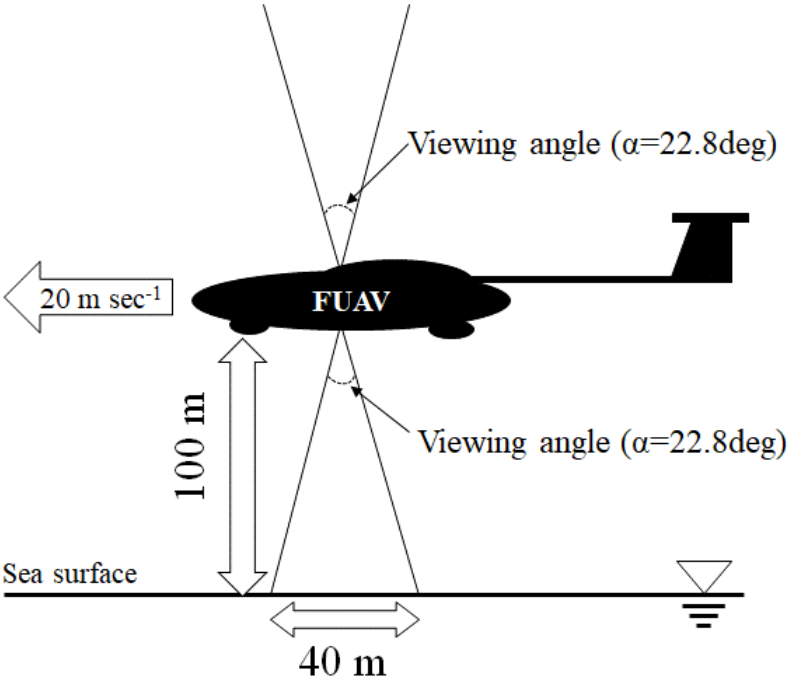

Fig. 3.3 Conceptual diagram of field observation of spectral radiance and irradiance during FUAV flights. The flight altitude was 100 m above the sea level and the flight speed was about 20 m s^{-1}. The spectral radiance and irradiance were measured every 5 seconds, so the spatial resolution of the obtained data was about 100 m. A cylinder for prevention of sun glint effect attached to the spectroradiometer sensor provides a viewing angle of 22.8 degrees, and the observation range of spectral radiance on the sea surface is about 40 m in diameter.

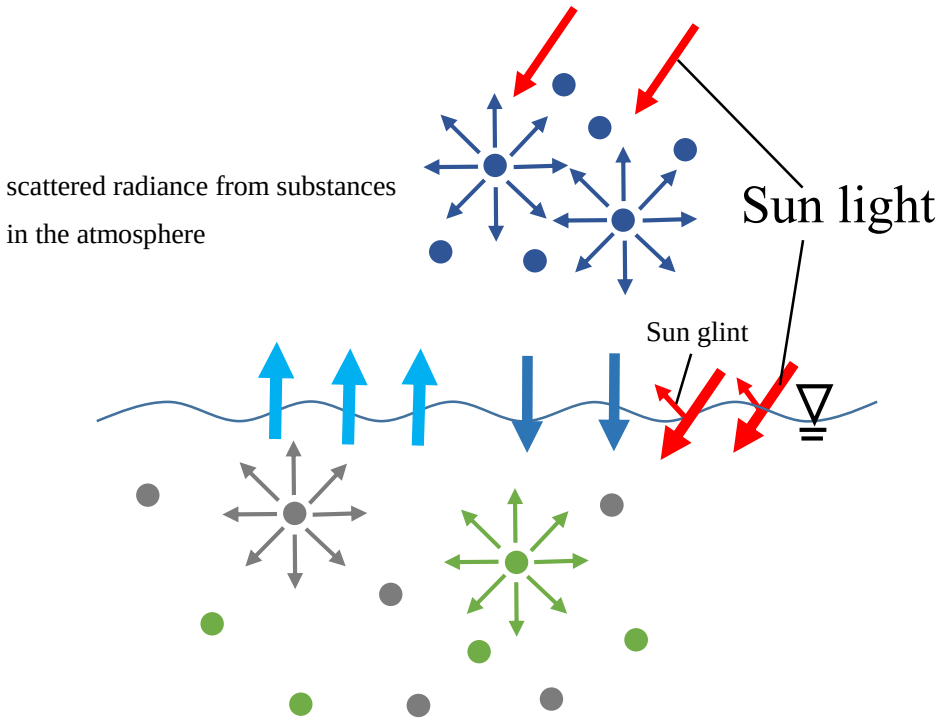

Fig. 3.4 Conceptual diagram of light behavior (absorption and scattering, radiation, etc.) in the atmosphere, sea surface, and in water.

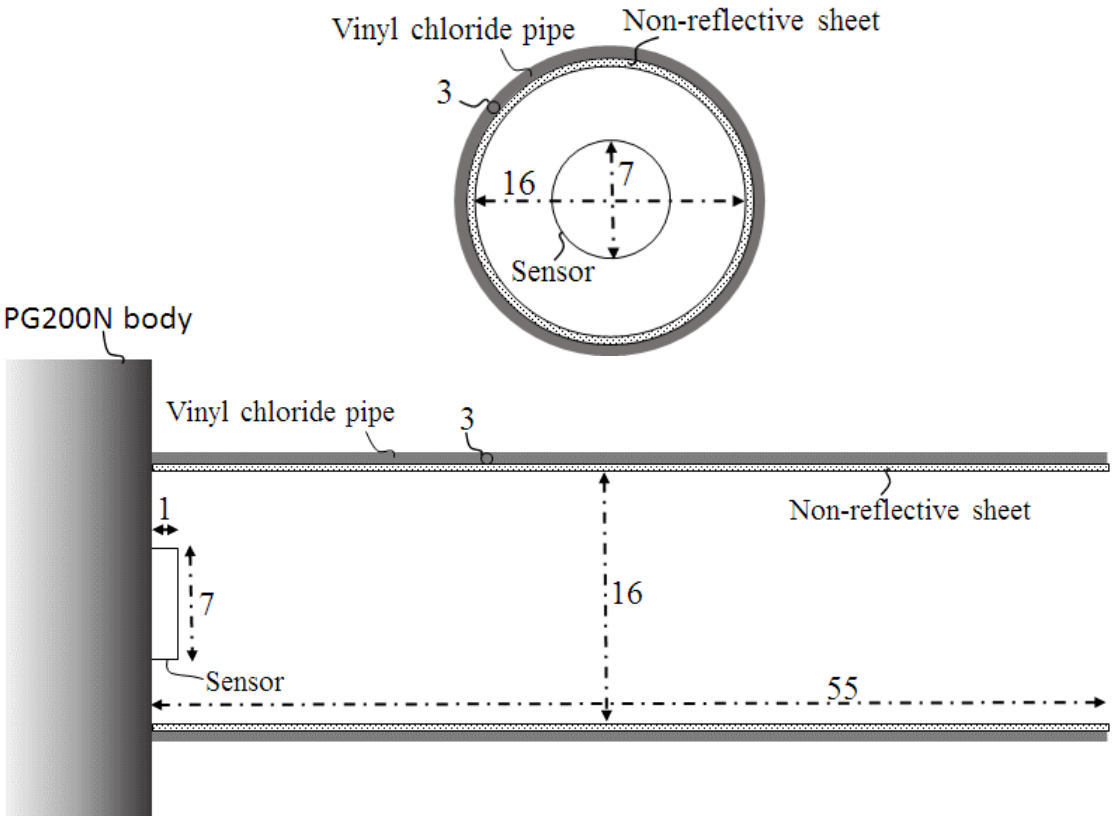

Fig. 3.5 Specifications of the cylinder attached to the spectroradiometer (PG200N). A non-reflective sheet (Super Black IR by Systems Engineering Inc.) is attached to the inside of the cylinder to prevent reflection of incident light.

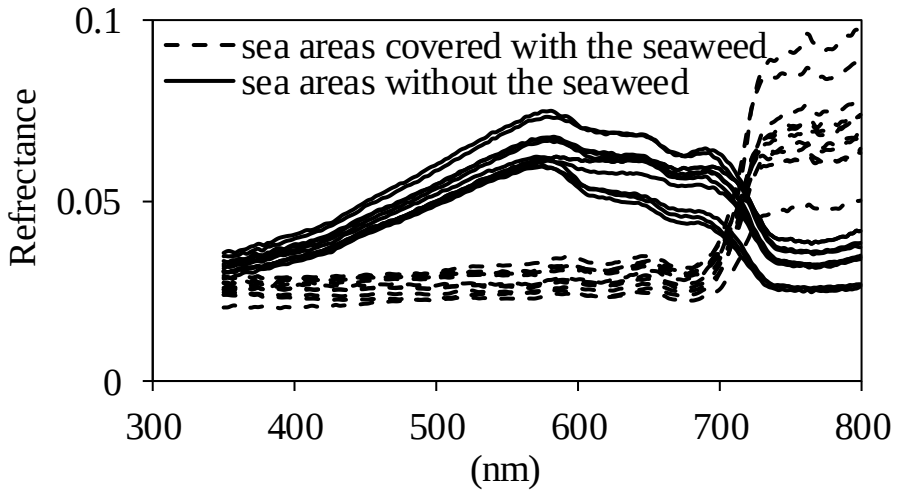

Fig. 3.6 Differences in light reflectance (*Rrs*) at each wavelength (350 nm to 800 nm) in sea areas covered with the seaweed (dashed lines) and without it (solid lines) observed at stations in Fig. 3.1.

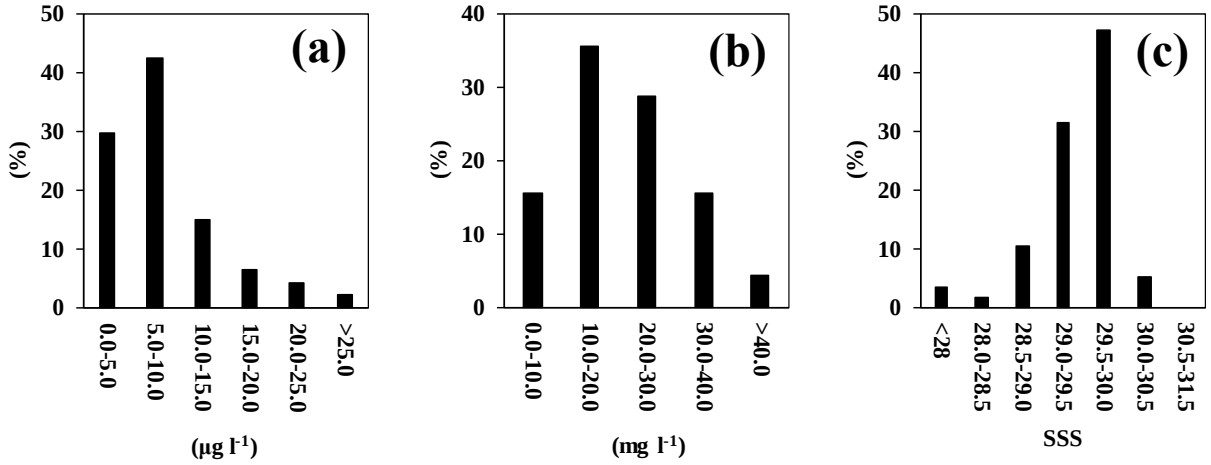

Fig. 3.7 Frequency distribution of (a) chlorophyll-a concentration, (b) TSM concentration and (c) salinity in seawater samples collected by the research vessels.

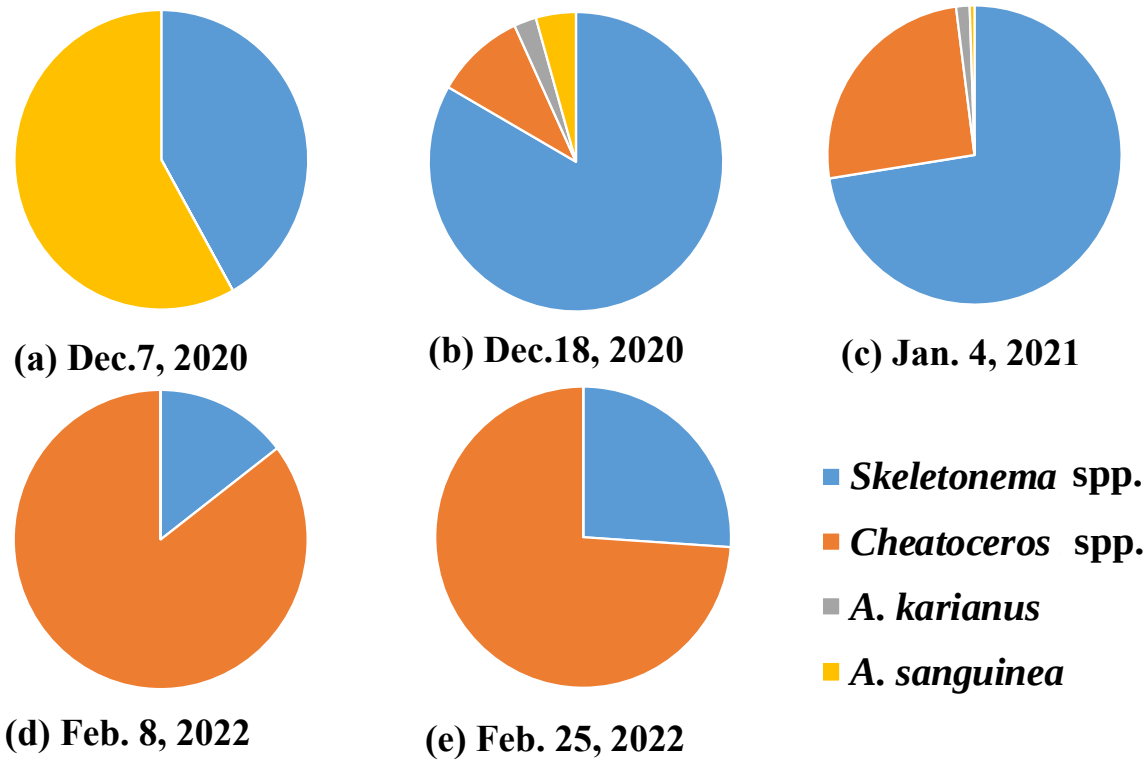

Fig. 3.8 Composition ratio of phytoplankton species at the timing closest to each observation date.

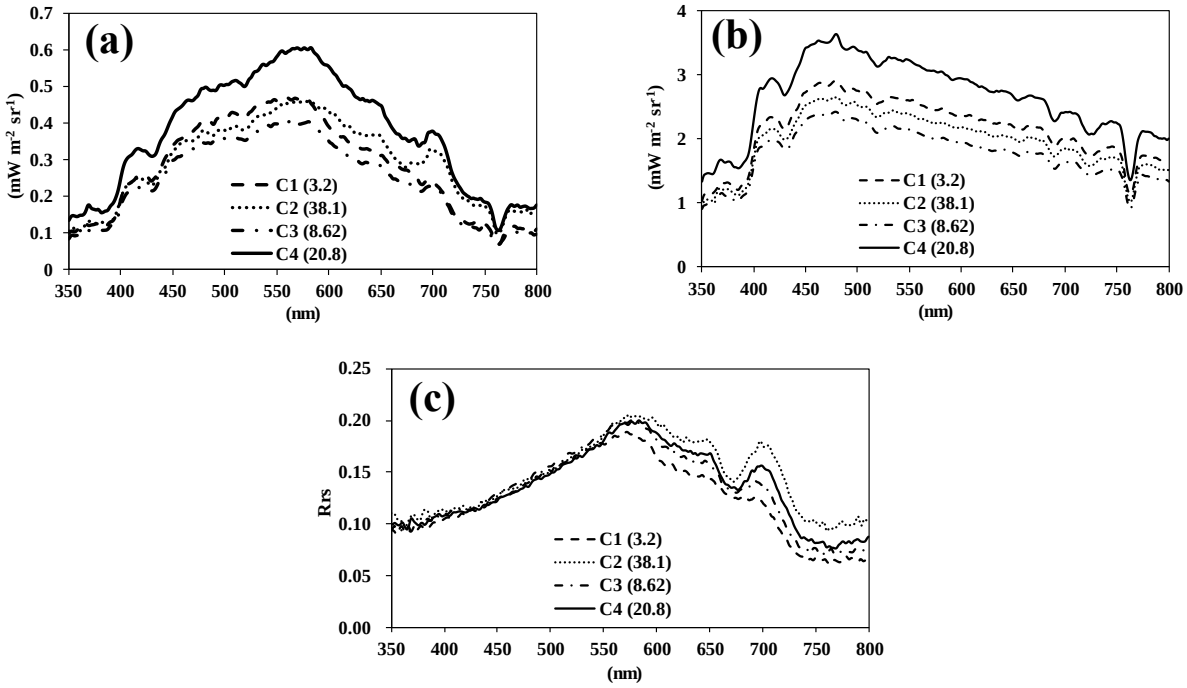

Fig. 3.9 (a) Spectral radiance, (b) irradiance and (c) reflectance ratio obtained at representative points (Sta. C1 to Sta. C4 in Fig. 3.1) on January 5, 2021. Values in parentheses next to station name are chlorophyll-a concentrations in the sea surface water.

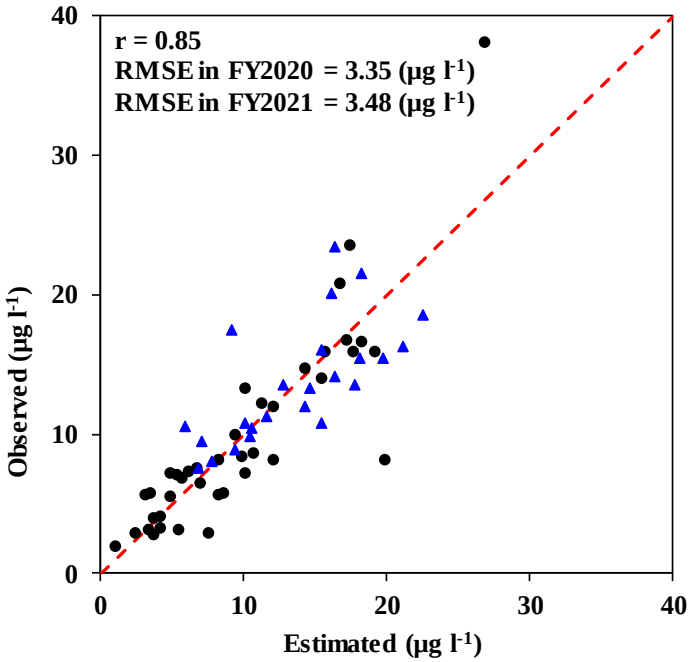

Fig. 3.10 Comparison result of chlorophyll-a concentration between estimated by Eq. (3.1) and contained in the sea-surface water in fiscal year 2020 (black circles) and 2021 (blue triangles). The red dashed line is one-to-one straight line.

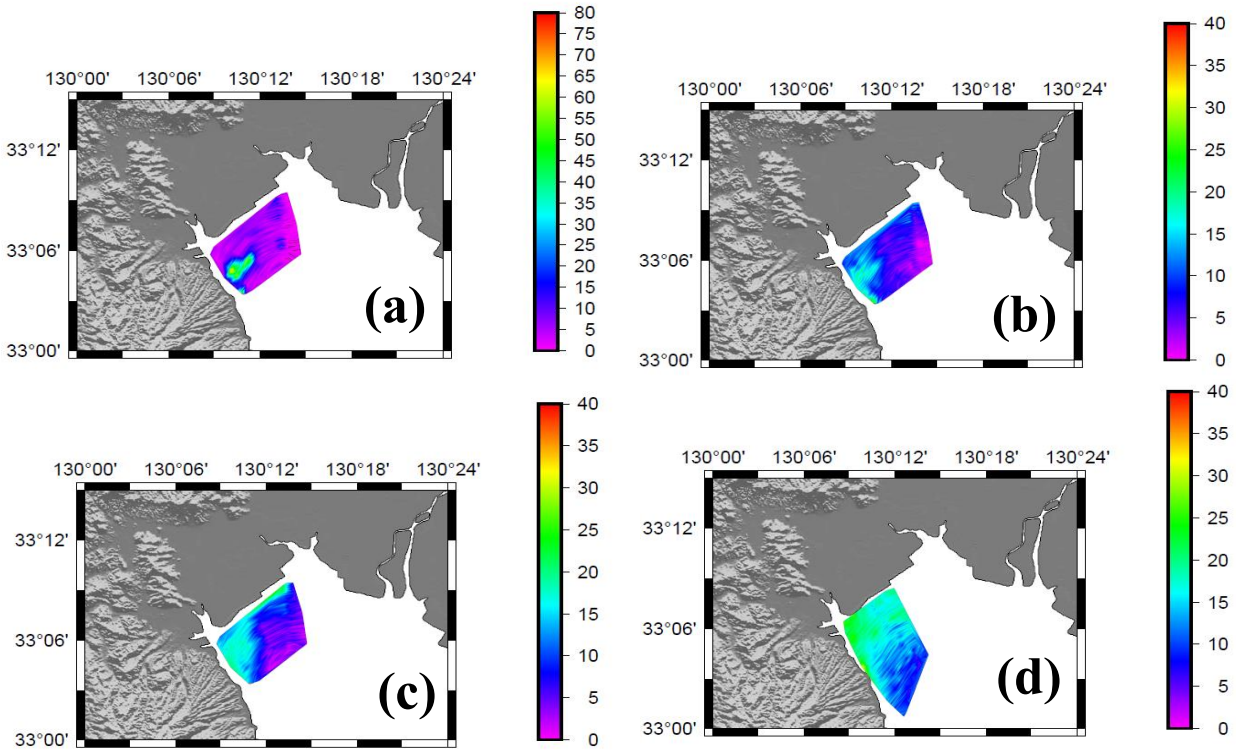

Fig. 3.11 The spatial distributions of sea-surface chlorophyll-a concentration (μg l^{-1}) on (a) December 7 and (b) 18, 2020, (c) January 5, 2021, and (d) February 24, 2022.

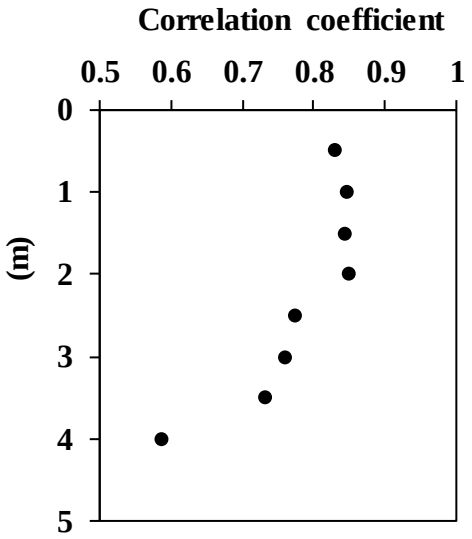

Fig. 3.12 Changes in the correlation coefficient between the chlorophyll-a concentration estimated by Eq. (3.1) and the chlorophyll fluorescence intensity obtained by CTD observation with water depth from 0.5 m to 4.0 m.

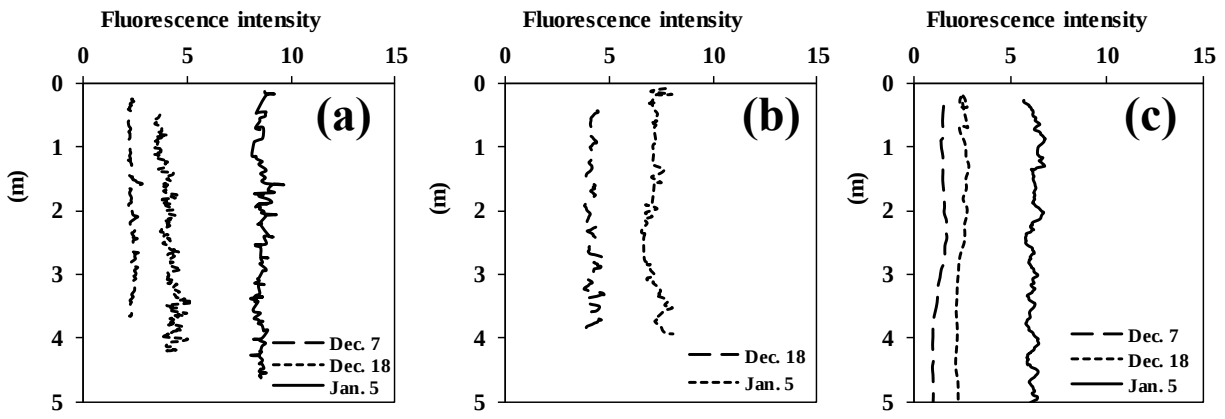

Fig. 3.13 Vertical distribution of chlorophyll fluorescence intensity obtained at (a) Sta. D1, (b) C4 and (c) D2 (Fig. 3.1) during three flights in fiscal year 2020. The data on December 7 at Sta. C4 was missed.

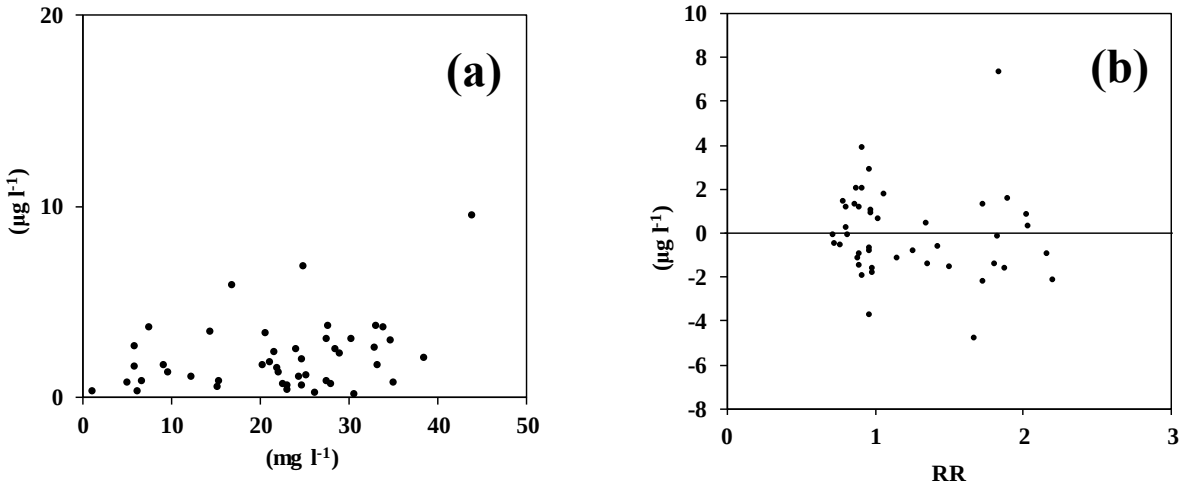

Fig. 3.14 Relationship between the estimation error of chlorophyll-a concentration (deviation from a one-to-one straight line shown in Fig. 3.10) and (a) TSM concentration and (b) the reflectance ratio at two wavelengths ($\mathrm{RR} = \frac{R_{rs}(665\ \mathrm{nm})}{R_{rs}(489\ \mathrm{nm})}$) .

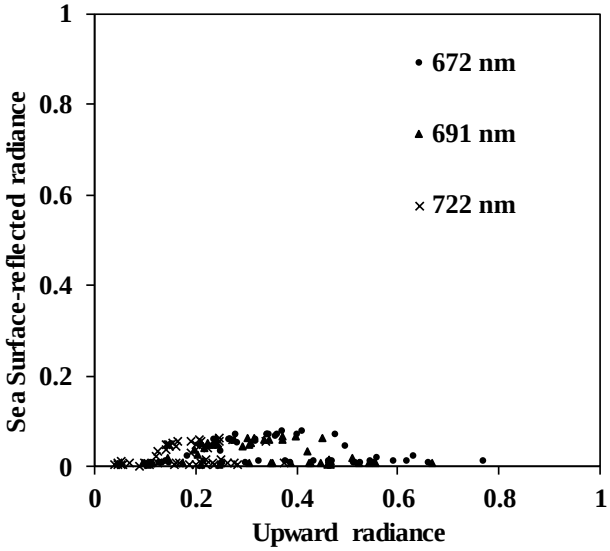

Fig. 3.15 Relationship between the sea-surface reflected radiance estimated by multiplying the reflectance rate (0.026) and the spectral irradiance measured by the FUAV-onboard upward sensor of PG200N and the radiance measured by the FUAV-onboard downward sensor at the three wavelengths (672 nm, 691 nm, 722 nm).

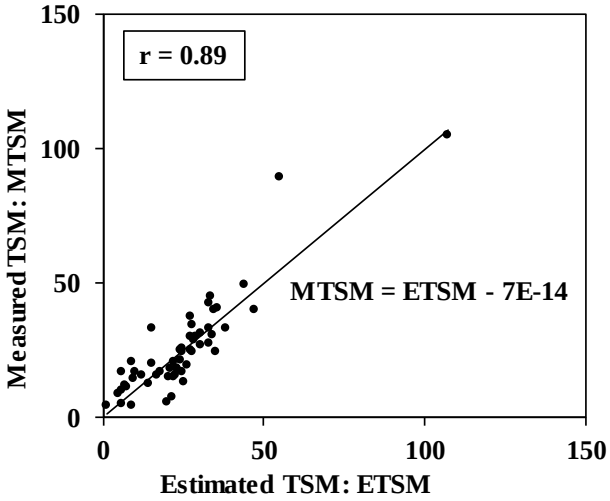

Fig. 3.16 Relationship between TSM concentration in seawater (MTSM) and those estimated from reflectance ratio of two wavelengths of 489 nm and 665 nm (ETSM).

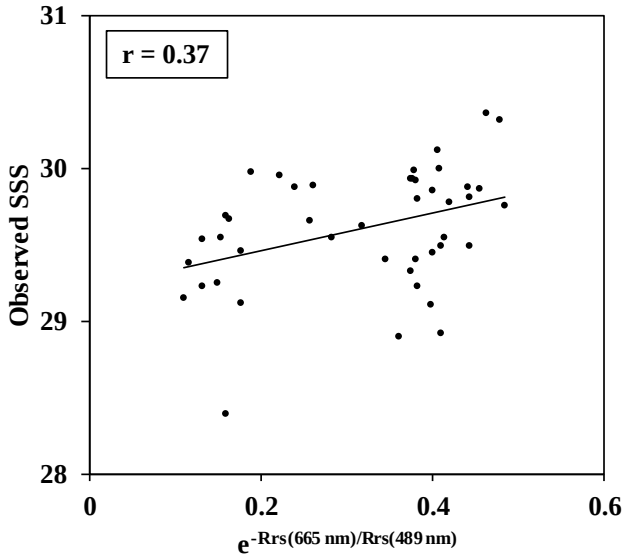

Fig. 3.17 Relationship between the observed sea surface salinity (SSS) and $e^{-\frac{R_{rs}(665\ \mathrm{nm})}{R_{rs}(489\ \mathrm{nm})}}$.

References

Ariga Y (1974) Color of cultured seaweed. Our nori research 23:1-14 (**Japanese**)

Bowers DG, Brett HL (2008) The relationship between CDOM and salinity in estuaries: An analytical and graphical solution. J. Mar. Syst. 73:1-7. https://doi.org/10.1016/j.jmarsys.2007.07.001

Bracher A, Bouman HA, Brewin RJW, Bricaud A, Brotas V, Ciotti AM, Clementson L, Devred E, Di Cicco A, Dutkiewicz S, Hardman-Mountford NJ, Hickman AE, Hieronymi M, Hirata T, Losa SN, Mouw CB, Organelli E, Raitsos DE, Uitz J, Vogt M, Wolanin A (2017) Obtaining phytoplankton diversity from ocean color: A scientific roadmap for future development. Front. Mar. Sci. 4 https://doi.org/10.3389/fmars.2017.00055

Chen S, Han L, Chen X, Li D, Sun L, Li Y (2015) Estimating wide range Total Suspended Solids concentrations from MODIS 250-m imageries: An improved method. ISPRS J. Photogramm. Remote Sens. 99:58-69 https://doi.org/10.1016/j.isprsjprs.2014.10.006

Cheng KH, Chan SN, Lee JHW (2020) Remote sensing of coastal algal blooms using unmanned aerial vehicles (UAVs). Mar. Pollut. Bull. 152:110889 https://doi.org/10.1016/j.marpolbul.2020.110889

Coble P, Hu C, Gould RW, Chang G, Michelle Wood A (2004) Colored dissolved organic matter in the coastal ocean: An optical tool for coastal zone environmental assessment and management. Oceanography 17:50–59 https://doi.org/10.5670/oceanog.2004.47

Dall'Olmo G, Gitelson AA (2006) Effect of bio-optical parameter variability and uncertainties in reflectance measurements on the remote estimation of chlorophyll-a concentration in turbid productive waters: modeling results. Applied Optics. 45(15):3577-3592. DOI: 10.1364/ao.45.003577. PMID: 16708105.

Dekker AG, Brando VE, Anstee JM (2005) Retrospective seagrass change detection in a shallow coastal tidal Australian lake. Remote Sens. Environ. 97:415–433 https://doi.org/10.1016/j.rse.2005.02.017

Del Pozo S, Rodríguez-Gonzálvez P, Hernández-López D, Felipe-García B (2014) Vicarious radiometric calibration of a multispectral camera on board an unmanned aerial system. Remote Sens. 6:1918-1937 https://doi.org/10.3390/rs6031918

Erdelj M, Król M, Natalizio E (2017) Wireless Sensor Networks and Multi-UAV systems for natural disaster management. Comput. Networks 124:72–86 https://doi.org/10.1016/j.comnet.2017.05.021

Fallati L, Polidori A, Salvatore C, Saponari L, Savini A, Galli P (2019) Anthropogenic Marine Debris assessment with Unmanned Aerial Vehicle imagery and deep learning: A case study along the beaches of the Republic of Maldives. Sci. Total Environ. 693:133581 https://doi.org/10.1016/j.scitotenv.2019.133581

Feng C, Ishizaka J, Saitoh K, Mine T, Yamashita H (2020) A novel method based on backscattering for discriminating summer blooms of the raphidophyte (chattonella spp.) and the diatom (skeletonema spp.) using MODIS images in Ariake Sea, Japan. Remote Sens. 12 https://doi.org/10.3390/RS12091504

Gao BC, Montes MJ, Li RR, Dierssen HM, Davis CO (2007) An atmospheric correction algorithm for remote sensing of bright coastal waters using MODIS land and ocean channels in the solar spectral region. IEEE Trans. Geosci. Remote Sens. 45:1835–1843 https://doi.org/10.1109/TGRS.2007.895949

Gitelson AA, Yacobi YZ, Schalles JF, Rundquist DC, Han L, Stark R, Etzion D (2000) Remote estimation of phytoplankton density in productive waters. Adv. Limnol. 55:121−136.

Gitelson AA, Schalles JF, Hladik CM (2007) Remote chlorophyll-a retrieval in turbid, productive estuaries: Chesapeake Bay case study. Remote Sens. Environ. 109:464–472 https://doi.org/10.1016/j.rse.2007.01.016

Gitelson AA, Dall'Olmo G, Moses W, Rundquist DC, Barrow T, Fisher TR, Gurlin D, Holz J (2008) A simple semi-analytical model for remote estimation of chlorophyll-a in turbid waters: Validation. Remote Sens. Environ. 112:3582–3593 https://doi.org/10.1016/j.rse.2008.04.015

Gitelson AA, Gurlin D, Moses WJ, Barrow T (2009) A bio-optical algorithm for the remote estimation of the chlorophyll-a concentration in case 2 waters. Environ. Res. Lett. 4 https://doi.org/10.1088/1748-9326/4/4/045003

Gons HJ, Auer MT, Effler SW (2008) MERIS satellite chlorophyll mapping of oligotrophic and eutrophic waters in the Laurentian Great Lakes. Remote Sens. Environ. 112:4098–4106 https://doi.org/10.1016/j.rse.2007.06.029

Gordon HR, Morel AY (1983) Remote assessment of ocean color for interpretation of satellite visible imagery: a review. https://doi.org/10.1002/9781118663707.fmatter

Gordon HR (1997) Atmospheric correction of ocean color imagery in the Earth Observing System era. J. Geophys. Res. 102:17081–17106

Gurlin D, Gitelson AA, Moses WJ (2011) Remote estimation of chl-a concentration in turbid productive waters - Return to a simple two-band NIR-red model? Remote Sens. Environ. 115:3479–3490 https://doi.org/10.1016/j.rse.2011.08.011

Hassan MA, Yang M, Fu L, Rasheed A, Zheng B, Xia X, Xiao Y, He Z (2019) Accuracy assessment of plant height using an unmanned aerial vehicle for quantitative genomic analysis in bread wheat. Plant Methods 15:1-13 https://doi.org/10.1186/s13007-019-0419-

7

Hooker SB, Lazin G, Zibordi G, Mclean S (2002) An evaluation of above- and in-water methods for determining water-leaving radiances. J. Atmos. Ocean. Technol. 19:486–515 https://doi.org/10.1175/1520-0426(2002)019<0486:AEOAAI>2.0.CO;2

IOCCG (2000) Remote Sensing of Ocean Colour in Coastal, and Other Optically-Complex, Waters. Sathyendrath, S.(ed.), Reports of the International Ocean-Colour Coordinating Group, No. 3, IOCCG, Dartmouth, Canada.

IOCCG (2010) Atmospheric Correction for Remotely-Sensed Ocean-Colour Products.Wang, M. (ed.), Reports of the International Ocean-Colour Coordinating Group, No.10, IOCCG, Dartmouth, Canada.

IOCCG (2014) Phytoplankton Functional Types from Space. Sathyendranath, S.(ed.), Reports of the International Ocean-Colour Coordinating Group, No. 15, IOCCG, Dartmouth, Canada.

Kako S, Morita S, Taneda T (2020) Estimation of plastic marine debris volumes on beaches using unmanned aerial vehicles and image processing based on deep learning. Mar. Pollut. Bull. 155:111127 https://doi.org/10.1016/j.marpolbul.2020.111127

Kanayama S, Yabuki S, Yanagisawa F, Motoyama R (2002) The chemical and strontium isotope composition of atmospheric aerosols over Japan: The contribution of long-range-transported Asian dust (Kosa). Atmos. Environ. 36:5159–5175 https://doi.org/10.1016/S1352-2310(02)00587-3

Keith DJ, Lunetta RS, Schaeffer BA (2016) Optical models for remote sensing of colored dissolved organic matter absorption and salinity in New England, Middle Atlantic and Gulf coast estuaries USA. Remote Sens. 8:1–22 https://doi.org/10.3390/rs8040283

Kim DW, Min TS, Kim Y, Silva RR, Hyun HN, Kim JS, Kim KH, Kim HJ, Chung YS (2019) Sustainable agriculture by increasing nitrogen fertilizer efficiency using low-resolution camera mounted on unmanned aerial vehicles. Int. J. Environ. Res. Public Health 16 https://doi.org/10.3390/ijerph16203893

Kramer SJ, Roesler CS, Sosik HM (2018) Bio-optical discrimination of diatoms from other phytoplankton in the surface ocean: Evaluation and refinement of a model for the Northwest Atlantic. Remote Sens. Environ. 217:126-143 https://doi.org/10.1016/j.rse.2018.08.010

Kutser T, Vahtmäe E, Praks J (2009) A sun glint correction method for hyperspectral imagery containing areas with non-negligible water leaving NIR signal. Remote Sens. Environ. 113:2267–2274 https://doi.org/10.1016/j.rse.2009.06.016

Li X, Shang S, Lee Z, Lin G, Zhang Y, Wu J, Kang Z, Liu X, Yin C, Gao Y (2021) Detection and Biomass Estimation of Phaeocystis globosa Blooms off Southern China from UAV-Based Hyperspectral Measurements. IEEE Trans. Geosci. Remote Sens. 60:1–13 https://doi.org/10.1109/TGRS.2021.3051466

Matsubara T, Yoshida Y, Shuto T (2011) Trends in occurrence of phytoplankton in the Ariake Sea off Saga Prefecture during a *porphyra* (nori) cultivation period (1989-2010). Study Report of Saga Prefectural Ariake Fisheries Research and Development Center 25:21-35 (**Japanese with English abstract**)

Matsubara T, Mine T, Ito S (2018) Population dynamics of harmful phytoplankton causing bleaching of cultured nori in the Shiota River estuary in innermost Ariake Sea, Japan. Bulletin on Coastal Oceanography 55(2):139-153 (**Japanese with English abstract**)

Matsuoka A, Campbell JW, Hooker SB, Steinmetz F, Ogata K, Hirata T, Higa H, Kuwahara VS,

Isada T, Suzuki K, Hirawake T, Ishizaka J, Murakami H (2021) Performance of JAXA's SGLI standard ocean color products for oceanic to coastal waters: chlorophyll a concentration and light absorption coefficients of colored dissolved organic matter. J. Oceanogr. 78:187–208 https://doi.org/10.1007/s10872-021-00617-2

McClain CR, Hooker S, Feldman G, Bontempi P (2006) Satellite data for ocean biology, biogeochemistry, and climate research. Eos (Washington. DC). 87:340-342 https://doi.org/10.1029/2006eo340002

Mobley CD (1999) Estimation of the remote-sensing reflectance from above-surface measurements. Appl. Opt. 38:7442-7455 https://doi.org/10.1364/ao.38.007442

Moore GF, Aiken J, Lavender SJ (1999) The atmospheric correction of water colour and the quantitative retrieval of suspended particulate matter in Case II waters: Application to MERIS. Int. J. Remote Sens. 20:1713-1733 https://doi.org/10.1080/014311699212434

Moore TS, Campbell JW, Dowell MD (2009) A class-based approach to characterizing and mapping the uncertainty of the MODIS ocean chlorophyll product. Remote Sens. Environ. 113:2424-2430 https://doi.org/10.1016/j.rse.2009.07.016

Mumby PJ, Green EP, Edwards AJ, Clark CD (1997) Measurement of seagrass standing crop using satellite and digital airborne remote sensing. Mar. Ecol. Prog. Ser. 159:51-60 https://doi.org/10.3354/meps159051

Odermatt D, Gitelson A, Brando VE, Schaepman M (2012) Review of constituent retrieval in optically deep and complex waters from satellite imagery. Remote Sens. Environ. 118:116-126 https://doi.org/10.1016/j.rse.2011.11.013

Pasqualini V, Pergent-Martini C, Pergent G, Agreil M, Skoufas G, Sourbes L, Tsirika A (2005) Use of SPOT 5 for mapping seagrasses: An application to Posidonia oceanica. Remote

Sens. Environ. 94:39-45 https://doi.org/10.1016/j.rse.2004.09.010

Sathyendranath S, Morel A (1983) Light Emerging from the Sea — Interpretation and Uses in Remote Sensing. In: Cracknell, A.P. (eds) Remote Sensing Applications in Marine Science and Technology. NATO ASI Series, 106, Springer, Dordrecht. https://doi.org/10.1007/978-94-009-7163-9_16

Sathyendranath S, Lazzara L, Prieur L (1987) Variations in the spectral values of specific absorption of phytoplankton. Limnol. Oceanogr. 32:403-415 https://doi.org/10.4319/lo.1987.32.2.0403

Schaeffer B, Conmy RN, Duffy AE, Aukamp J, Yates DF, Craven G (2015) Northern Gulf of Mexico estuarine coloured organic matter derived from MODIS data. Int. J. Remote Sens. 36:2219–2237

Schalles JF (2006) Optical remote sensing techniques to estimate phytoplankton chlorophyll a concentrations in coastal waters with varying suspended matter and CDOM concentrations, Remote Sensing and Digital Image Processing. https://doi.org/10.1007/1-4020-3968-9

Shang S, Lee Z, Lin G, Hu C, Shi L, Zhang Y, Li X, Wu J, Yan J (2017) Sensing an intense phytoplankton bloom in the western Taiwan Strait from radiometric measurements on a UAV. Remote Sens. Environ. 198:85-94 https://doi.org/10.1016/j.rse.2017.05.036

Siegel DA, Wang M, Maritorena S, Robinson W (2000) Atmospheric correction of satellite ocean color imagery: the black pixel assumption. Appl Opt. 39(21):3582-3591 doi: 10.1364/ao.39.003582. PMID: 18349929.

Siswanto E, Ishizaka J, Tripathy SC, Miyamura K (2013) Detection of harmful algal blooms of Karenia mikimotoi using MODIS measurements: A case study of Seto-Inland Sea, Japan. Remote Sens. Environ. 129:185-196 https://doi.org/10.1016/j.rse.2012.11.003

Su TC, Chou HT (2015) Application of multispectral sensors carried on unmanned aerial vehicle (UAV) to trophic state mapping of small reservoirs: A case study of Tain-Pu reservoir in Kinmen, Taiwan. Remote Sens. 7:10078-10097 https://doi.org/10.3390/rs70810078

Tiwari SP, Shanmugam P (2011) An optical model for the remote sensing of coloured dissolved organic matter in coastal/ocean waters. Estuar. Coast Shelf Sci. 93:396-402

Toratani M, Fukushima H, Murakami H, Tanaka A (2007) Atmospheric correction scheme for GLI with absorptive aerosol correction. J. Oceanogr. 63:525-532 https://doi.org/10.1007/s10872-007-0047-0

Tripathy SC, Ishizaka J, Siswanto E, Shibata T, Mino Y (2012) Modification of the vertically generalized production model for the turbid waters of Ariake Bay, southwestern Japan. Estuar. Coast. Shelf Sci. 97:66-77 https://doi.org/10.1016/j.ecss.2011.11.025

Tzortziou M, Subramaniam A, Herman JR, Gallegos CL, Neale PJ, Harding LW (2007) Remote sensing reflectance and inherent optical properties in the mid Chesapeake Bay. Estuar. Coast. Shelf Sci. 72:16-32 https://doi.org/10.1016/j.ecss.2006.09.018

Villar RE, Martinez JM, Le Texier M, Guyot JL, Fraizy P, Meneses PR, Oliveira E de (2013) A study of sediment transport in the Madeira River, Brazil, using MODIS remote-sensing images. J. South Am. Earth Sci. 44:45–54 https://doi.org/10.1016/j.jsames.2012.11.006

Vodacek A, Blough NV, DeGrandpre MD, Peltzer ET, Nelson RK (1997) Seasonal variation of CDOM and DOC in the Middle Atlantic Bight: Terrestrial inputs and photooxidation. Limnol. Oceanogr. 42:674-686 https://doi.org/10.4319/lo.1997.42.4.0674

Wang M, Shi W (2007) The NIR-SWIR combined atmospheric correction approach for MODIS ocean color data processing. Opt Express. 15:15722-15733 doi: 10.1364/oe.15.015722.

PMID: 19550856.

Wang M, Son SH, Shi W (2009) Evaluation of MODIS SWIR and NIR-SWIR atmospheric correction algorithms using SeaBASS data. Remote Sens. Environ. 113:635-644 https://doi.org/10.1016/j.rse.2008.11.005

Wei J, Lee Z, Shang S (2016) A system to measure the data quality of spectral remote-sensing reflectance of aquatic environments, J. Geophys. Res. Oceans. 121:8189-8207 doi:10.1002/2016JC012126.

Yang MM, Ishizaka J, Goes JI, Gomes H do R, Maúre E de R, Hayashi M, Katano T, Fujii N, Saitoh K, Mine T, Yamashita H, Fujii N, Mizuno A (2018) Improved MODIS-Aqua chlorophyll-a retrievals in the turbid semi-enclosed Ariake Bay, Japan. Remote Sens. 10:1-20 https://doi.org/10.3390/rs10091335

Zeng C, Richardson M, King DJ (2017) The impacts of environmental variables on water reflectance measured using a lightweight unmanned aerial vehicle (UAV)-based spectrometer system. ISPRS J. Photogramm. Remote Sens. 130:217-230 https://doi.org/10.1016/j.isprsjprs.2017.06.004

Zhang M, Hu C, English D, Carlson P, Muller-Karger FE, Toro-Farmer G, Herwitz SR (2015) Atmospheric Correction of AISA Measurements over the Florida Keys Optically Shallow Waters: Challenges in Radiometric Calibration and Aerosol Selection. IEEE J. Sel. Top. Appl. Earth Obs. Remote Sens. 8:4189-4196 https://doi.org/10.1109/JSTARS.2015.2437326

Chapter 4
Investigation of the effect of physical environment on phytoplankton growth by numerical simulation

4.1 Introduction

Chapter 2 focused on the environment for phytoplankton outbreak at the first neap tide just after reaching the minimum water temperature. The results of Chapter 3 and Matsubara et al. (2011) indicated that phytoplankton concentration was chronically high in the western part of the inner Ariake Sea regardless of dominant species. This suggests that the phytoplankton outbreaks in the western area is caused by the mechanism revealed in Chapter 2 under the conditions that phytoplankton concentration is chronically high in this area.

The purpose of this Chapter is to investigate the physical environment for chronical high concentration of phytoplankton cell in the western part of the inner Ariake Sea through the numerical simulation. The structure of this Chapter is as follows. In Section 4.2, we describe analysis method for field observation data and setup of numerical simulation in detail. In Section 4.3, we describe analysis results of field observation data and numerical simulation. Section 4.4 discusses the effect of physical environment on distributions of three phytoplankton species. Section 4.5 provides conclusion from this Chapter.

4.2 Methods

4.2.1 Analysis method for field observation data

Weekly monitoring data of three phytoplankton cell number of *Skeletonem* spp., *E. zodiacus* and *A. karianus*, emerging frequently in the western part of the inner Ariake Sea, at

stations from Sta. 1 to Sta. 8 in Fig. 2.1 from 2000 to 2017 during autumn and winter season (from September to April) was used in the present study.

To evaluate the relationship between dynamics of three phytoplankton species and sea environments, in this study, red tide index (*RI*; cells ml^{-1} *days) based on Tsutsumi et al. (2003) was defined as follows:

$$RI = cell\ number \times duration\ time \tag{4.1}$$

where *duration time* (days) is interval between observations.

4.2.2 Numerical simulation

In this study, Finite Volume Community Ocean Model (FVCOM; Chen et al. 2003) was used as a physical model in numerical simulation. Fig. 4.1 shows the numerical domain used in this study. The horizontal domain consists of an unstructured triangular mesh. Mesh size is 200 m around the seaweed aquaculture field in the inner Ariake Sea and gradually increases up to 5000 m toward the open boundary. The vertical coordinate system is multi-sigma coordinate of 13 layers (Pietrzak et al. 2002). This model considers wet-dry treatment in tidal flat areas. The effect of fluid drag by the seaweed aquaculture (nets and poles) was considered in the aquaculture field.

Weather data (air temperature, air pressure, humidity, solar radiation, rain fall, cloud cover and vapor pressure; excluding wind velocity and direction) obtained from Saga Prefecture by the Japan Meteorological Agency were used (Sta. Saga in Fig. 1.1a). Spatial distribution of wind velocity and direction were used by Meso-Scale Model (MSM, horizontal grid is 5 km)

dataset supplied by the Japan Meteorological Agency. From these weather data, heat and freshwater fluxes as a sea surface boundary condition were calculated by the Coupled Ocean-Atmosphere Response Experiment version 3.0 (COARE 3.0; Fairall et al. 2003). For the river inflow, the model considers seven first-class rivers (Chikugo, Kase, Rokkaku, Yabe, Kikuchi, Shira, and Midori) and large second-class rivers by the Ministry of Land, Infrastructure, Transport, and Tourism. Fresh water discharge was not considered from the two gates of the reservoir in the Isahaya Bay (Fig. 1.1a). For the open boundary conditions, the amplitude and phase of eight tidal components (M_2, S_2, N_2, K_2, K_1, O_1, P_1 Q_1) were forced by the NAO.99jb regional tide model (Matsumoto et al. 2000). Temperature and salinity obtained from the FRA-JCOPE2 reanalysis dataset (Miyazawa et al. 2009) were nudged at the open boundary by using a relaxation scheme (Davies 1976). This scheme was used within a range of 10 km from the open boundary and allowed to incorporate the FRA-JCOPE2 reanalysis data into the model smoothly.

The numerical simulation was initialized with resting state for water. The initial spatial distribution of temperature and salinity fields were used seasonally averaged values for January, February and December. These data in the Ariake Sea were used monthly monitoring data taken by the Saga Prefectural Ariake Fisheries Research and Development Center, Fukuoka Fisheries and Marine Technology Research Center and Kumamoto Prefectural Fisheries Research, and outside the Ariake Sea were used FRA-JCOPE2 reanalysis data (Miyazawa et al. 2009). The boundary conditions (weather and river discharge) were used seasonally averaged constant values for January, February and December.

For evaluation of water exchange characteristics in the inner area, residence time was calculated by tracer experiment. The inner Ariake Sea was divided into 13 boxes (Fig. 4.2a),

and initial tracer concentration of 1.0 was installed in whole water column of each box and subsequent this tracer concentration in each box was monitored with time. The horizontal scale of each box of tracer experiments (Fig. 4.2a) were determined by the results of cluster analysis by using weekly cell number of three phytoplankton species (*Skeletonem* spp., *E. zodiacus* and *A. karianus*) at the sea surface data. The tracer was installed at high tide of spring tide after the simulation reached a steady state, and the time series of tracer concentration was calculated. Fig.4.2b shows time series of tracer concentration in BOX B and Fig. 4.2c, d, e show the horizontal distributions of tracer concentration transported from BOX B. The tracer is transported by surrounding current and gradually decrease exponentially with time. As an indicator of water exchange rate, residence time was evaluated (Takeoka 1984). This time is defined as e-folding scale, i.e. the time when the exponential approximation line (black line in Fig. 4.2b) for time series of tracer concentration decreased to 1/e (e is number of Napiers) of initial tracer concentration. Relationship between the residence time and the *RI* in each box was analyzed. In addition, tracer experiments were conducted in case without the seaweed aquaculture, influence of seaweed aquaculture on residence time and the *RI* was also analyzed.

4.3 Results

4.3.1 *RI* distribution based on field observation data

Fig. 4.3 shows the *RI* distributions of *Skeletonema* spp., *E. zodiacus*, *A. karianus* calculated by Eq. (4.1). The *RI* distributions of these phytoplankton species were high in the north-western area of the inner Ariake Sea, especially for *Skeletonema* spp. and *A. karianus*. Therefore, as results of Chapter 3 and report of Matsubara et al. (2011), the north-western area of inner Ariake Sea is the favorable environment for phytoplankton growth.

4.3.2 Effect of physical environment on phytoplankton growth

Fig. 4.4 shows the horizontal distribution of residence time in 13 boxes. The residence time in the western area of the inner Ariake Sea was longer than that in the other areas. Fig. 4.5 shows relationship between the calculated residence time in each box and the *RI*. There was a high correlation the *RI* of *Skeletonema* spp. ($r = 0.84$, $p = 0.022$; r is correlation coefficient and p is p value) and *A. karianus* ($r = 0.96$, $p = 0.00034$). This result indicates that the strength of water exchange strongly controls the *RI*. The *RI* of *E. zodiacus* had low correlative relationship with the water exchange rate ($r = 0.77$, $p = 0.052$). Fig. 4.6 shows the contribution rate of advection and diffusion in tracer concentration flushing out of BOX B (Fig. 4.2a). It is found that the contribution rate of advection was dominant. This means that the transportation of tracer is controlled by residual current. Fig 4.7 shows the horizontal distributions of residual current in the sea surface and bottom layer (1 m above the sea bed) at neap tide by using 48-hour tide killer filter (Hanawa and Mitsudera 1985). The residual current was basically flowing offshore (southward current) in the sea surface and onshore in the bottom layer (northward current). The strength of the residual current was strong in the western area and weak in the eastern area.

The influence of seaweed aquaculture on residence time and the *RI* was examined next. Fig. 4.8 shows the change of residence time in each box (Fig. 4.2a) due to seaweed aquaculture. The residence time was prolonged in most boxes. Mean residence time in case with/without seaweed aquaculture were 84.4 hours and 75.6 hours, respectively. Fig. 4.9 shows the increase rate of the *RI* of each phytoplankton specie due to seaweed aquaculture. The value was calculated by applying the change of residence time to each correlation equation shown in Fig. 4.5. The *RI* of *Skeletonema* spp. and *A. karianus* increased by about 17% and 33%, respectively.

This means that seaweed aquaculture makes physical environment more suitable for phytoplankton growth in the western part of the inner Ariake Sea.

4.4 Discussion

The present study described that the *RI* distributions of three phytoplankton species were high in the western area of the inner Ariake Sea, so that favorable condition for phytoplankton growth was formed. The reason for this was low water exchange rate. The horizontal difference of water exchange rate was induced by the horizontal difference in the strength of residual current. In the inner Ariake Sea, density-driven current is strengthened in the eastern area because of buoyancy input from large first-class rivers (Chikugo, Yabe, Rokkaku and Kase river in Fig 1.1a), but, in the western area, density-driven current is not strengthened because there are only small second-class rivers (Shiota and Kashima river in Fig. 1.1a). Therefore, spatial differences of residual current were derived by unequally-distributed freshwater input. The seaweed aquaculture increased the residence time, so that the seaweed aquaculture formed more favorable environments for phytoplankton growth in terms of physical environment, especially for *Skeletonema* spp. and *A. karianus*. The correlation between the *RI* and residence time didn't have significance of 5% for *E. zodiacus*. Ito et al. (2013) reported that *E. zodiacus* in the bottom layer in offshore area first increased by improved light condition in the water column. This result indicates that the other factor except water exchange rate played a more important role for *E. zodaicus* growth.

Phytoplankton growth is affected also by biochemical environment such as temperature, light environment and nutrients. The effect of biochemical environment on phytoplankton growth chronically in the western part of the inner Ariake Sea during winter is investigated in

next Chapter 5.

4.5 Conclusions

This Chapter investigated the effect of physical environment on growth environment of three phytoplankton species, *Skeletonem* spp., *E. zodiacus* and *A. karianus*, causing color bleaching of seaweed by numerical simulation. The observation data indicated that the *RI* was high in the western area, so that this area was confirmed that the favorable environment for phytoplankton growth chronically. Relationship between this local high concentration and physical environment (water exchange) was investigated. There was significant relationship between the *RI* and water exchange rate, and the strength of water exchange was weak in the inner western area. The case of this was determined by undeveloped density-driven current due to buoyancy loads is low. Thus, the favorable physical environment affected phytoplankton growth in the inner western area.

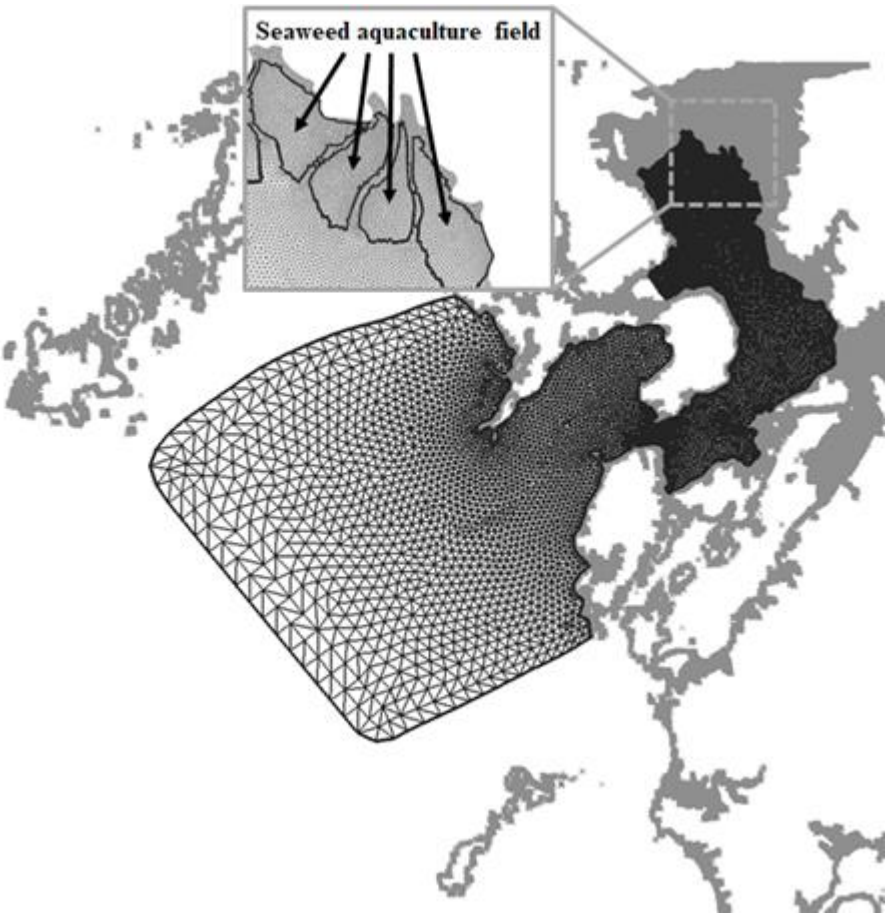

Fig. 4.1 Domain of numerical simulation and unstructured triangular mesh. Black arrows area is the seaweed aquaculture field.

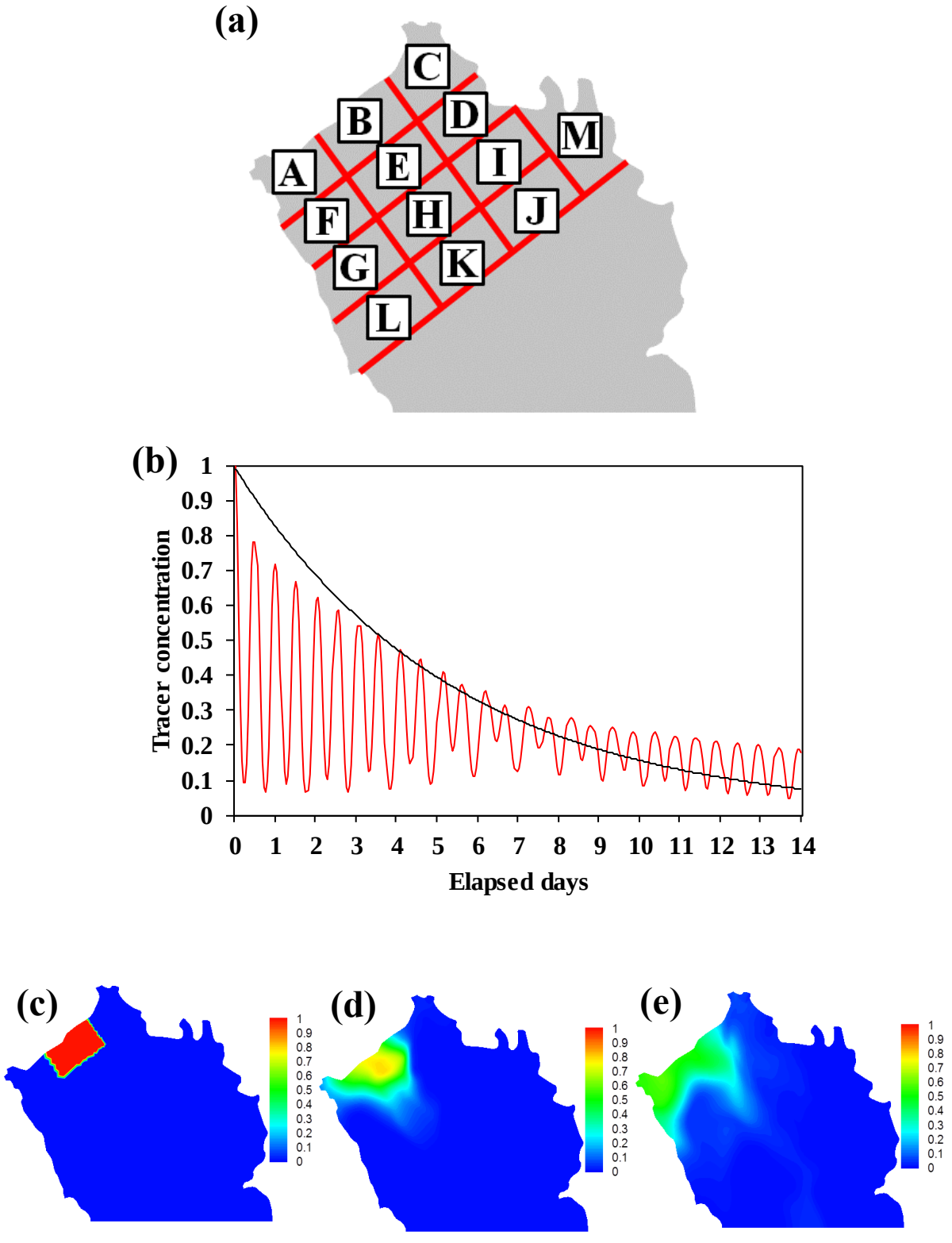

Fig. 4.2 (a) The distribution of boxes divided by 13 to conduct tracer experiments in the inner Ariake Sea, (b) time series of tracer concentration in BOX B in two weeks, (c) initial distribution of tracer concentration installed in BOX B, the distribution of tracer concentration transported from BOX B after (d) 4 days and after (e)10 days.

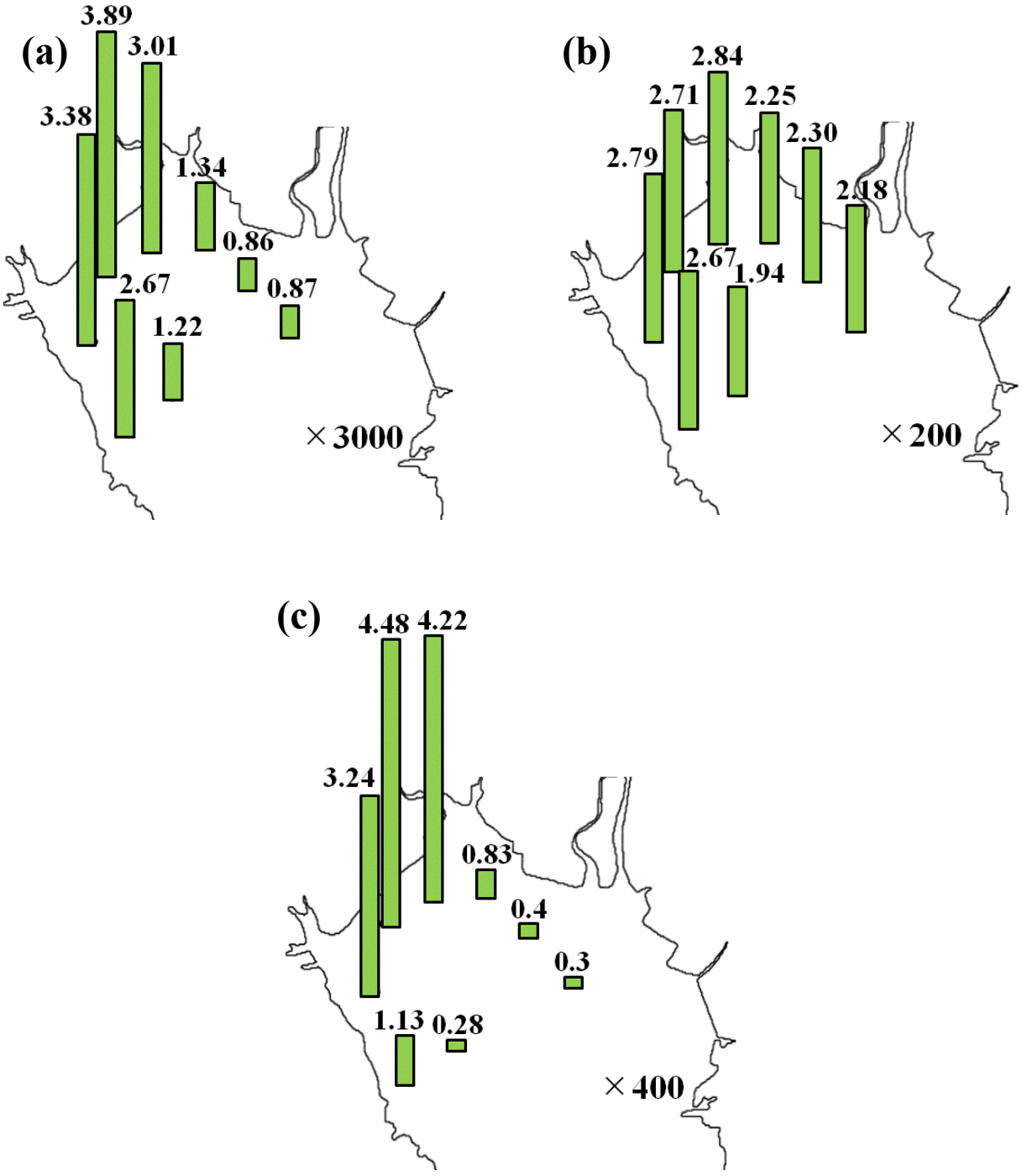

Fig. 4.3 The *RI* distributions of (a) *Skeletonema* spp., (b) *E. zodiacus* and (c) *A. karianus*.

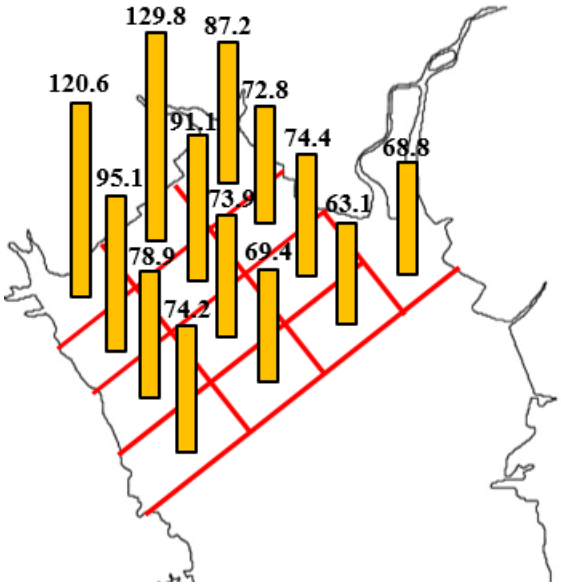

Fig. 4.4 Horizontal distribution of residence time in 13 boxes.

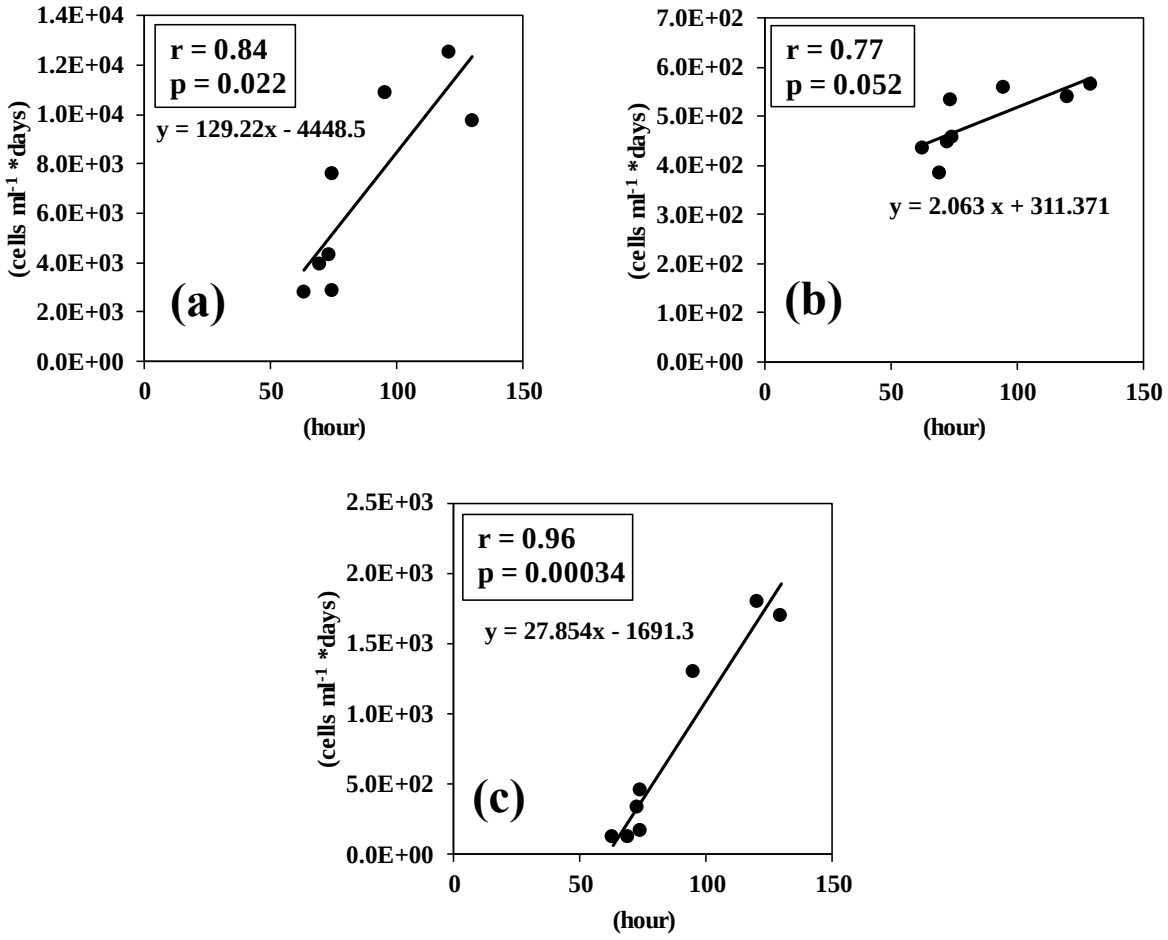

Fig. 4.5 Relationship between the *RI* and residence time for (a) *Skeletonema* spp., (b) *E. zodiacus* and (c) *A. karianus*.

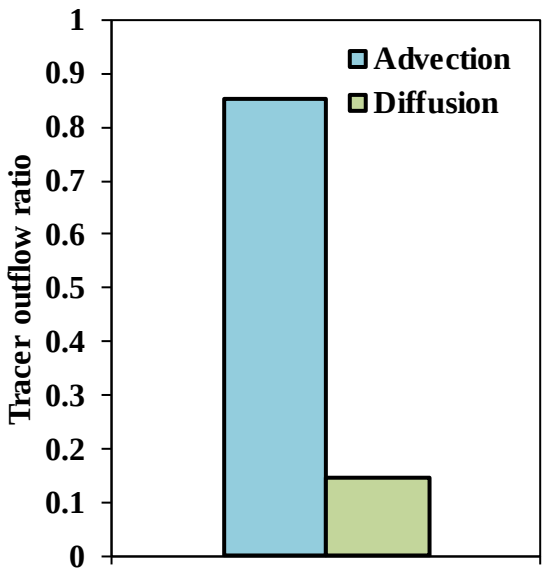

Fig. 4.6 The contribution rate of advection and diffusion in tracer concentration flushing out of BOX B.

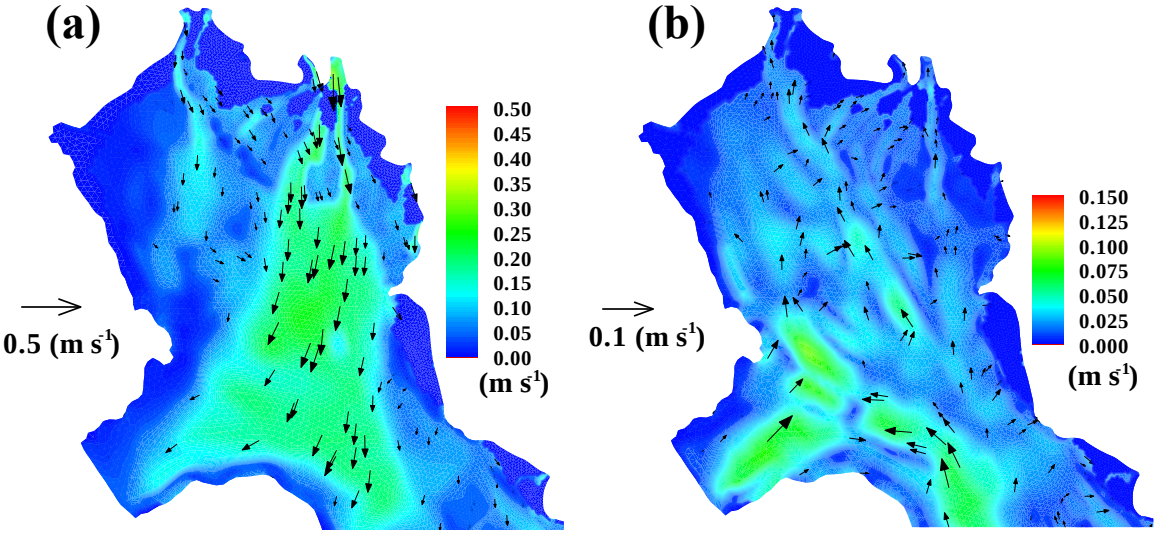

Fig. 4.7 Horizontal distributions of residual current (a) in the sea surface and (b) near the bottom layer (1 m above the sea bed) at neap tide.

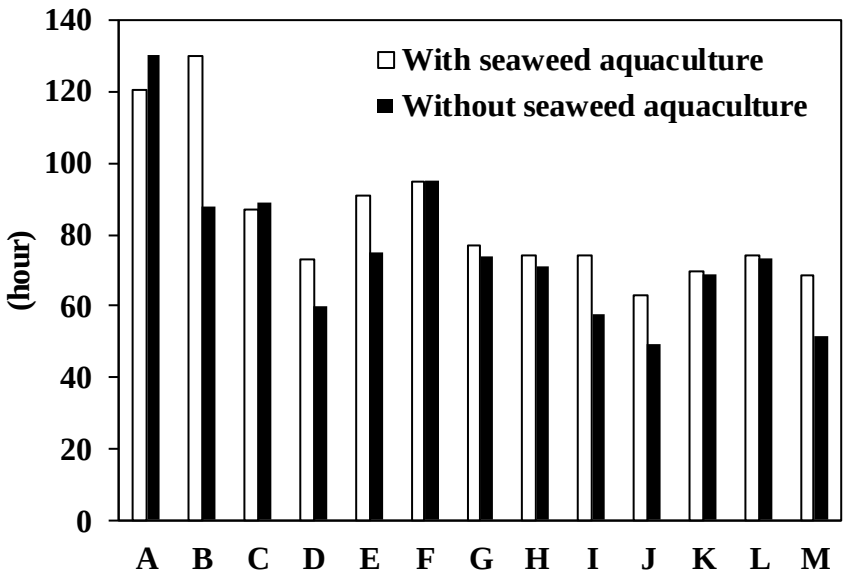

Fig. 4.8 The change of residence time of each box by seaweed aquaculture (With seaweed aquaculture: Consider seaweed aquaculture, without seaweed aquaculture: Not consider seaweed aquaculture).

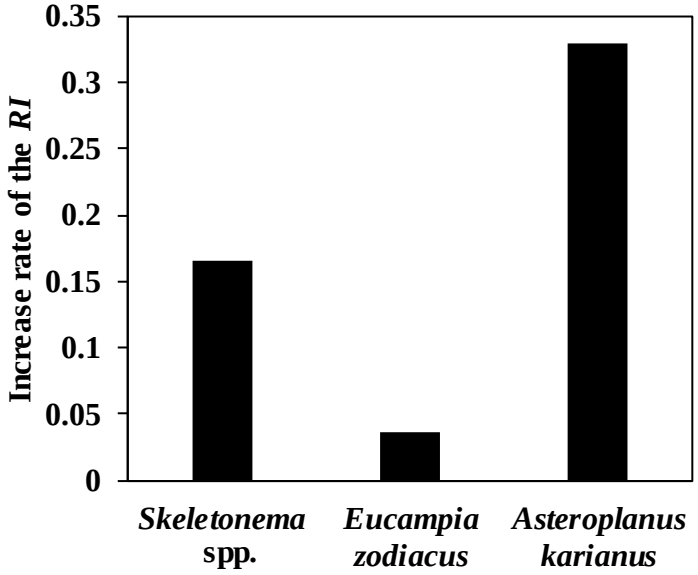

Fig. 4.9 The increase rate of the *RI* of three phytoplankton species by seaweed aquaculture.

References

Chen C, Liu H, Beardsley RC (2003) An unstructured grid, finite-volume, three-dimensional, primitive equations ocean model: Application to coastal ocean and estuaries. Journal of Atmospheric and Oceanic Technology 20:159-186

Davies HC (1976) A lateral boundary formulation for multi-level prediction models. Quarterly Journal of the Royal Meteorological Society 102:405–418

Fairall CW, Bradley EF, Hare JE, Grachev AA, Edson JB (2003) Bulk parameterization of airsea fluxes: updates and verification for the COARE Algorithm. Journal of Climate 16:571-591

Hanawa K, Mitsudera H (1985) On daily average of oceanographic data. Bulletin on Coastal Oceanography 23(1):79–87 (**Japanese**)

Ito Y, Katano T, Fujii N, Koriyama M, Yoshino K, Hayami Y (2013) Decreases in turbidity during neap tides initiate late winter blooms of *Eucampia zodiacus* in a macrotidal embayment. Journal of Oceanography 69(4):467-479

Matsubara T, Yoshida Y, Shuto T (2011) Trends in occurrence of phytoplankton in the Ariake Sea off Saga Prefecture during a *porphyra* (nori) cultivation period (1989-2010). Study Report of Saga Prefectural Ariake Fisheries Research and Development Center 25:21-35 (**Japanese with English abstract**)

Matsumoto K, Takanezawa T, Ooe M (2000) Ocean tide models developed by assimilating TOPEX/POSEIDON altimeter data into hydrodynamical model: a global model and a regional model around Japan. Journal of Oceanography 56(5):567-581

Miyazawa Y, Zhang R, Guo X, Tamura H, Ambe D, Lee JS, Okuno A, Yoshinari H, Setou T, Komatsu K (2009) Water mass variability in the western North Pacific detected in a 15-year eddy resolving ocean reanalysis. Journal of Oceanography 65(6):737-756

Pietrzak J, Jakobson JB, Burchard H, Vested HJ, Petersen O (2002) A three-dimensional hydrostatic model for coastal and ocean modelling using a generalized topography following co-ordinate system. Ocean Modelling 4(2):173-205

Takeoka H (1984) Exchange and transport time scales in the Seto Inland Sea. Continental Shelf Research 3(4):327-341

Tsutsumi H, Okamura E, Ogawa M, Takahashi T, Yamaguchi H, Montani S, Kohashi N, Adachi T, Komatsu T (2003) Studies of the cross section of water in the innermost areas of Ariake Bay with the recent occurrence of hypoxic water and red tide. Oceanography in Japan 12(3):291-305 (**Japanese with English abstract**)

Chapter 5

Development of an ecosystem model and investigation of the effect of physical and chemical-biological environments on phytoplankton growth by numerical simulation

5.1 Introduction

In Chapter 4, we investigated the physical environment for the phytoplankton growth in the western part of the inner Ariake Sea during winter. However, phytoplankton growth is affected also by chemical-biological environments. To investigate the effect of these environments on chronical high concentration of phytoplankton cell in the western part of the inner Ariake Sea during winter, the ecosystem model that incorporate the physiological characteristics of phytoplankton dynamics is effective method. However, the seaweed aquaculture in coastal areas changes the light environment and takes in nutrients in water column, so it is essential that these effects considered in this ecosystem model.

The purpose of this Chapter is to apply an ecosystem model to investigate the physical and chemical-biological environments favorable for the phytoplankton growth in the western part of the inner Ariake Sea during winter. The structure of this Chapter is as follows. In Section 5.2, we describe the method of field observation for the effect of seaweed aquaculture on underwater light environment, development of an ecosystem model and setup of numerical simulation in detail. In Section 5.3, we describe change in light environment due to seaweed aquaculture by field observation data, validation of the ecosystem model and results of numerical simulation. Section 5.4 discusses the physical and chemical-biological environments favorable for the phytoplankton growth. Section 5.5 provides conclusion from this Chapter.

5.2 Methods

5.2.1 Field observation

Field observation was conducted in the seaweed aquaculture in the inner Ariake Sea owned by the Saga Prefectural Ariake Fisheries Research and Development Center (observation station is near Sta. 8 in Fig. 2.1). Fig. 5.1 shows schematic diagram of this field observation system. This observation was measured light intensity and water depth at 0.5 m below the sea surface under the seaweed net, and light intensity, water depth, water temperature, salinity and turbidity at 0.5 m below the sea surface in the sea area close to the seaweed aquaculture without the seaweed net from 15 January to 25 January, 2019. The light intensity and water depth were measured every 5 seconds (DEFI2-L and DEFI2-D10 by JFE Advantec Co.), and the water temperature, salinity and turbidity were measured every 10 minutes (INFINITY ACTW-USB and INFINITY ACLW-USB by JFE Advantec Co.). The turbidity value (*Turb*) at 0.5 m below the sea surface was converted to suspended sediment (*SS*; mg l^{-1}) concentration in the sea surface using the relationship of $SS = 2.52 \times Turb - 19.61$ (*SS* was measured by the same method in Section 2.2). The light attenuation coefficient was calculated by the following equation (Ministry of the environment 2002):

$$K_d = 0.0702 \times SS + 0.3128 \tag{5.1}$$

where K_d is the light attenuation coefficient (m^{-1}). To examine the relationship between seaweed growth and its effect on light environment in the water column, length of seaweed leaf (LL; cm) was measured.

Additionally, weekly monitoring data of phytoplankton cell number of *Skeletonema* spp., transparency and dissolved inorganic nitrogen (DIN) at stations from Sta. 1 to Sta. 8 in Fig. 2.1 for January, February and December from 1997 to 2018 was used in the present study.

5.2.2 Numerical simulation

Physical model in numerical simulation was used as the same as model in Chapter 4 (see Section 4.2). We incorporated suspended sediment transport model based on Hamada et al. (2009) into the numerical simulation, but sediment resuspension equation in this model was modified to improve light environment in water column. This modified sediment resuspension equation from the seabed was expressed as below:

$$\begin{aligned} E &= 0 && \tau < \tau_{ce} \\ E &= M_0(\tau - \tau_{ce}) && \tau \geq \tau_{ce} \end{aligned} \tag{5.2}$$

where E is an erosion flux (g m^{-2} s^{-1}), M_0 is a parameterized erosion velocity coefficient (s m^{-1}), τ is sheer stress at the seabed (g m^{-1} s^{-2}) and τ_{ce} is critical sheer stress at the seabed (g m^{-1} s^{-2}). Here, the M_0 (s m^{-1}) was parameterized by field observation data in the inner Ariake Sea (Yamamoto et al. 2008, 2009; Hamada et al. 2009) as follow (Fig. 5.2):

$$M_0 = \frac{mud \cdot M}{\tau_{ce}} = 0.0014 \cdot exp(0.8356 \cdot Md\varphi) \tag{5.3}$$

where *mud* is mud content, *M* is an erosion velocity coefficient (g m^{-2} s^{-1}) and $Md\varphi = log_2 D$ is value by median diameter of particle size (*D*; mm) at the seabed. The spatial distribution of this $Md\varphi$ was mapped as the same of Hamada et al. (2009) in the Ariake Sea.

Ecosystem model based on Yamaguchi and Hayami (2018) was applied in the numerical simulation. Fig. 5.3 shows the ecosystem diagram, and Table 5.1 and 5.2 show definition of model variables and description of each material flux in the present ecosystem model. The phytoplankton specie in the present ecosystem model considered *Skeletonema* spp. which have emerged frequently in the inner Ariake Sea during winter. Especially, it was based on the physiological parameters of *Skeletonema costatum* in *Skeletonema* spp., which many physiological data have been reported (Table 5.3). Furthermore, in the present study, the effect of seaweed aquaculture on light environment (described in detail in the next section) and the effect of nutrient uptake by seaweed in the aquaculture field was incorporated in the ecosystem model. This uptake kinetics for nitrate and ammonium (BSN_{NO3} and BSN_{NH4}; μM) by seaweed based on previous studies (Yamamoto and Takao 1988; Kawaguchi et al. 2005) were modeled in the present ecosystem model as follows:

$$BSN_{NO3} = \alpha_{NO3}^{S} \cdot \mu_{NO3}^{S} \cdot \mu_{S}^{S} \cdot SB \quad (5.4)$$

$$BSN_{NH4} = \alpha_{NH4}^{S} \cdot \mu_{NH4}^{S} \cdot \mu_{S}^{S} \cdot SB \quad (5.5)$$

where *SB* is the seaweed biomass (mg m^{-2}). The α_{NO3}^{S} and α_{NH4}^{S} are the maximum nitrate and ammonium uptake term (h^{-1}), μ_{NO3}^{S} and μ_{NH4}^{S} are the nitrate and ammonium limitation term, and μ_{S}^{S} is the salinity limitation term defined as below:

$$\alpha_{NO3}^{S} = 10^{-32.464X^2+227.45X-401.36} \tag{5.6}$$

$$\alpha_{NH4}^{S} = 10^{-29.642X^2+206.93X-363.23} \tag{5.7}$$

$$\mu_{NO3}^{S} = \frac{NO_3}{K_{NO3}^{S} + NO_3} \tag{5.8}$$

$$\mu_{NH4}^{S} = \frac{NH_4}{K_{NH4}^{S} + NH_4} \tag{5.9}$$

$$\mu_{S}^{S} = 0.013 + \left(\frac{33.01}{26.73\sqrt{\frac{\pi}{2}}}\right) exp\left(\frac{-2(S_S - 28.98)^2}{26.73^2}\right) \tag{5.10}$$

where *NO3* and *NH4* are nitrate and ammonium concentration (μM), and S_S is salinity in the surface layer. The *X* and half saturation constant for nitrate and ammonium (K_{NO3}^{S} and K_{NH4}^{S}; μM) are defined as:

$$K_{NO3}^{S} = 10^{-37.051X^2+257.5X-445.69} \tag{5.11}$$

$$K_{NH4}^{S} = 10^{-39.556X^2+276.17X-479.77} \tag{5.12}$$

$$X = \left(\frac{1}{T_S + 273.15}\right) \times 10^3 \tag{5.13}$$

where T_S is water temperature in the surface layer (℃). The present study incorporated this nutrient uptake by seaweed in the ecosystem model considering the occupancy rate of the seaweed aquaculture facilities per unit area (34%) and the occupancy rate of the seaweed net in the aquaculture field. Details other formulations and parameters in the present ecosystem model are described in Table 5.6 and 5.7 (see Appendix 5.A and 5.B).

The numerical simulation aims to reproduce the physical and chemical-biological environments, and investigate the phytoplankton growth environment in the western part of the

inner Ariake Sea during winter. The simulation was initialized with resting state for water. The initial spatial distribution of temperature and salinity fields were used seasonally averaged values for January, February and December. These data in the Ariake Sea were used monthly monitoring data taken by the Saga Prefectural Ariake Fisheries Research and Development Center, Fukuoka Fisheries and Marine Technology Research Center and Kumamoto Prefectural Fisheries Research, and outside the Ariake Sea were used FRA-JCOPE2 reanalysis data (Miyazawa et al. 2009). The initial spatial distribution of biochemical variables (excluding POC_B, PHY_B and *SB*) were used monitoring data taken by the Ministry of the Environment (2002). The initial spatial distribution of POC_B and PHY_B variables were set to zero, and *SB* was constant value based on the report of Masuda et al. (2014) because of the steady state calculation. The boundary conditions (weather, river discharge and loads, etc.) were used seasonally averaged constant values for January, February and December. The simulation results were validated by the data after reaching a steady state.

To investigate the phytoplankton growth environment in the western area, we divided this area into 13 boxes (Fig. 4.2a) and conducted a phytoplankton budget analysis in each box. This analysis calculated temporal change of phytoplankton concentration (B) fluxes by physical and biochemical processes in water column at each box in the unit tons of carbon per day as following advection-diffusion equation:

$$\frac{\partial B}{\partial t} + u\frac{\partial B}{\partial x} + v\frac{\partial B}{\partial y} + w\frac{\partial B}{\partial z} = K_h\left(\frac{\partial^2 B}{\partial x^2} + \frac{\partial^2 B}{\partial y^2}\right) + \frac{\partial}{\partial z}\left(K_z\frac{\partial B}{\partial z}\right) + \left(\frac{\partial B}{\partial t}\right)_{bc} \qquad (5.14)$$

where x, y, and z are eastward, northward and upward directions; u, v and w are velocity in x, y and z direction; t is time; K_h is horizontal diffusion coefficient parameterized by Smagorinsky (1963); K_z is vertical diffusion coefficient parameterized by Mellor-Yamada 2.5 turbulent closure scheme (Mellor and Yamada 1982; Galperin et al. 1988). In the Eq. (5.14), the first term in the left-hand side is temporal change; sum of the second and third term in the left-hand side is horizontal advection term (HorAdv); fourth term in the left-hand side is vertical advection (VerAdv); the sum of the first and second term in the right-hand side is horizontal diffusion (HorDif); the third term in the right-hand side is vertical diffusion (VerDif); the fourth term in the right-hand side is chemical-biological processes. These chemical-biological processes include growth by photosynthesis (Photosynthesis), extracellular release by phytoplankton (Extracellular), respiration of phytoplankton (Respiration), natural mortality of phytoplankton (NaturalMortality), sinking on the seabed (Deposition), feeding by zooplankton (ZOO) and resuspension from the seabed (Resuspension). In this budget analysis calculation, to exclude the effect of initial phytoplankton distribution, the initial condition of phytoplankton variable (PHYC) was only used horizontally and vertically uniform value (80.85 mgC m^{-3}) at all nodes. This value was the monitoring data taken by the Ministry of the Environment (2002) the nearest outside the Ariake Sea. The budge analysis results were analyzed over the period from the minimum to the maximum value at flood tide for phytoplankton concentration in each box after reaching a steady state.

5.3 Results

5.3.1 Effect of the seaweed aquaculture on light environment in water column

The effect of the seaweed aquaculture on light environment in water column was analyzed

by filed observation data. Fig. 5.4 shows the temporal variation of light intensity just under the seaweed net and in the sea area close to the aquaculture without the seaweed net. Because the water depth of the light intensity under and without the seaweed net was difference, these light intensities were converted to the value at the sea surface by using Eq. (2.1). The K_d was estimated by SS concentration by using the Eq. (5.1). To evaluate the effect of light environment in water column by the seaweed aquaculture, attenuation rate which was calculated as light intensity under the seaweed net divided by light intensity without the seaweed net was calculated from these converted light intensities. The relationship between the attenuation rate and LL provided that the attenuation rate was defined as a function of LL by exponential approximation as following (Fig. 5.5).

$$Attenuation\ \ rate = 0.9571 \cdot exp(-0.105 \cdot LL) \tag{5.15}$$

This equation indicated that the longer LL was, the smaller this attenuation rate was detected. The average LL during the observation period was 14.12 cm, and when applied to the Eq. (5.15), the attenuation rate was 0.23. Thus, the present result revealed that the seaweed net blocked light intensity about 77% on average. The present study incorporated this attenuation effect in the numerical simulation considering the occupancy rate of the seaweed aquaculture facilities per unit area (34%) and the occupancy rate of the seaweed net in the aquaculture field as the same as nutrient uptake by seaweed. Because the numerical simulation in the present study was steady state calculation, LL was set to be constant value of 14.12 cm.

5.3.2 Numerical analysis

The calculation results were validated by comparison with observation data. Fig. 5.6 shows comparison of surface phytoplankton, transparency and surface DIN, limiting nutrients for phytoplankton growth in the Ariake Sea (Kawaguchi et al. 2005; Katano et al. 2013), at monitoring stations (Sta. 1 to Sta. 8 in Fig. 2.1) between observation and calculation data. The observation data was averaged for January, February and December from 1997 to 2018. The calculation data was averaged for spring-neap tide cycle (15 days) after the hydrographic fields achieved steady-state. This calculation data was used at high tide because the observation data was obtained at this timing. For comparison of surface phytoplankton, these phytoplankton data were converted by standardization because unit of each data is difference (observation data is cells ml^{-1} and calculation data is mgC m^{-3}). The scatter plots of surface phytoplankton, transparency and surface DIN show high correlations between the observed and calculated data, although the trend of calculated DIN is slightly underestimated in low concentration area and overestimated in high concentration area (Fig. 5.6, the black dashed line is one-to-one straight line). These results show that the numerical simulation in the present study accurately reproduced the environment in the western part of the inner Ariake Sea during winter.

The physical and chemical-biological environments favorable for the phytoplankton growth in the western area was investigated by phytoplankton budget analysis. We comprised between analysis results of BOX B (western area), BOX J (eastern area) and BOX K (offshore area). Fig. 5.7 shows the phytoplankton concentration in three boxes. The amount of phytoplankton concentration in BOX B was the highest in three boxes after about 190.0 day in calculation time (reaching steady-state condition). The budget analysis period was conducted from 243.542 to 248.833 day in calculation time for BOX B and from 244.625 to 249.875 day in calculation time for BOX J and BOX K (near the black hatched-area in Fig. 5.7). Fig. 5.8

shows contribution of physical and chemical-biological processes to change in phytoplankton fluxes in BOX B, J and K. These values are averaged during each budget analysis period. Among these fluxes, comparing the fluxes of three boxes, increasing phytoplankton flux due to horizontal advection and photosynthesis in BOX B is especially higher than that in BOX J and K. Thus, increasing phytoplankton concentration in BOX B during budget analysis period was caused by photosynthesis and horizontal advection.

The phytoplankton photosynthesis in the present ecosystem model are controlled by light limitation term, nutrient limitation term (nitrate in the Ariake Sea) and water temperature (see Photosynthesis term B_1 in Table 5.6). Table 5.4 shows these photosynthesis components averaged during budget analysis period in each box. In these components, the water temperature and nutrient limitation value in BOX K was the highest in three boxes, but the light limitation value in BOX B was the highest in three boxes. Because the photosynthesis term in BOX B is the highest in three boxes, this result indicates that the western area has the suitable light environment in water column for phytoplankton growth.

The structure of flow that caused change in phytoplankton concentration due to horizontal advection was investigated. Fig. 5.9 shows the change in phytoplankton fluxes due to horizontal advection in each direction and layer in three boxes. These values are averaged during each budget analysis period. The horizontal advection in BOX B was dominated by the outflow flux in the upper layer and inflow flux in the lower layer from the LINE B2. The horizontal advection in BOX J was dominated by the outflow flux from the LINE J1 and inflow flux from the LINE J3. The horizontal advection in BOX K was dominated by the inflow flux in the upper layer and outflow flux in the lower layer from the LINE K1, and the outflow flux in the upper layer and inflow flux in the lower layer from the LINE K3. These results indicate that increasing

phytoplankton concentration in BOX B is caused by supply due to horizontal advection in the lower layer from offshore area.

5.4 Discussion

5.4.1 Phytoplankton growth environment in the western part of the inner Ariake Sea

We developed the ecosystem model incorporated into the effect of the seaweed aquaculture on surrounding the surrounding environment. The numerical simulation with this ecosystem model reproduced coastal environment accurately in the western part of the inner Ariake Sea during winter (Fig. 5.6). The phytoplankton budget analysis by this numerical simulation showed that the favorable conditions for phytoplankton growth in the western area resulted from photosynthesis and horizontal advection (Fig. 5.8). This photosynthesis was caused by suitable light environment (Table 5.4) and horizontal advection was caused by supply in the lower layer from offshore area (Fig. 5.9).

We evaluated how the difference in light environment in water column occurred by relationship between active mixing layer depth (AML) and euphotic layer depth (ELD). AML was defined as the depth at which dissipation rate of turbulent kinetic energy approached $1.0 \times 10^{-8.5}$ W kg^{-1} (Hopkins et al. 2021). This AML represents the depth at which phytoplankton concentration is almost the same from the sea surface. ELD was defined as the same as Section 2.1 and calculated by using Eq. (2.1). The threshold value of the minimum PAR intensity is 5.9 $\mu mol\ m^{-2}\ s^{-1}$ (Table 5.3). This ELD represents the depth at which phytoplankton can grow by photosynthesis from the sea surface. Thus, the ELD/AML ratio represents light environment for phytoplankton growth by photosynthesis in water column, so the higher this value, the more

available the light for phytoplankton in the water column to grow. Table 5.5 shows the AML, ELD and ELD/AML ratio averaged during each budget analysis period in BOX B, J and K (Fig. 4.2a). Comparison of three boxes, the AML in BOX B is the lowest value and the ELD in BOX B is the highest value, so the ELD/AML ratio in BOX B is highest value. Thus, BOX B have favorable light conditions in water column for phytoplankton growth by photosynthesis, and this environment caused the high photosynthesis value in BOX B (Fig. 5.8).

The structure of change in phytoplankton concentration due to horizontal advection in BOX B is similar to that of BOX K but different from that of BOX J (Fig. 5.9). To evaluate these differences of flow structure, we calculated along-bay direction residual current (along the white dash line in right panel in Fig. 5.9a) at the spring and neap tide by using a 48-hour tide-killer filter (Hanawa and Mitsudera 1985, Fig. 5.10). These residual currents showed the surface outflow and bottom inflow patterns. Especially, this surface outflow was strong in shallow water area and bottom inflow was strong above submarine channel area. Kasai et al. (2000) indicated that estuarine circulation in ROFIs was characterized different patterns depending on the Ekman number (*Ek*) defined as following:

$$Ek = \frac{KM}{f \times H^2} \tag{5.16}$$

where *KM* is vertical eddy viscosity coefficient ($m^2\ s^{-1}$), *f* is Coriolis parameter (s^{-1}) and *H* is water depth (m). In the present study, the *Ek* was calculated the mean value of the cross section. This *Ek* of the 25 hour running mean was 0.66 at the spring tide and 0.18 at the neap tide. In the case of $Ek \sim 0.1$, residual current in the lower layer of the central part of the bay is inflow due to the effect of viscosity and in the upper layer is outflow due to geostrophic flow (Kasai

et al. 2000). This indicates that BOX B and K located deep of the central part of the cross section perpendicular to the along-bay direction are dominated by surface outflow and bottom inflow due to estuarine circulation, and BOX J located shallow near the end of the cross section perpendicular to the along-bay direction is dominated by outflow/inflow in water column due to geostrophic flow. Therefore, the differences of flow structure in three boxes are caused by the differences of location in cross section perpendicular to the along-bay direction.

5.4.2 Limitation of the present numerical simulation

The present ecosystem model considered only *Skeletonema costatum* in *Skeletonema* spp. as the phytoplankton compartment. The composition of *Skeletonema* spp. has been subdivided some species (Zingone et al. 2005; Sarno et al. 2005, 2007), and each species has had different physiological characteristics (Kaeriyama et al. 2011). In fact, the dominant specie was *Skeletonema dohrnii* in *Skeletonema* spp. for FY2020 in Chapter 2 (Yoshida K. personal communication). However, field observation data sets and physiological data for each specie subdivided *Skeletonema* spp. are remained unclear. Furthermore, the inner Ariake Sea during winter not only the *Skeletonema* spp. but also various species have appeared, such as *Eucampia zodiacus* and *Asteroplanus karianus* in Chapter 4. Future studies should consider these phytoplankton species.

Phytoplankton growth may be also related to seed population. For *Skeletonema* spp. and *Asteroplanus karianus*, resting cells in bottom sediment behave as seed population (Matsubara et al. 2014). The resting cells of *Skeletonema* spp. distribute highly in the western part of the inner Ariake Sea (Ministry of Agriculture, Forestry and Fisheries 2003). Nothing have been known about distribution of the resting cells of *Asteroplanus karianus*, but Yamaguchi et al.

(2017) suggested that this specie increased in the Shiota and Kashima river estuaries and the increase may be because of the seed population on the seabed there. Although further discussion is difficult since there is not enough information on seed population at the present, further investigation is needed for the relationship between the seed population and phytoplankton outbreaks.

5.5 Conclusions

This Chapter applied an ecosystem model to investigate the physical and chemical-biological environments favorable for the phytoplankton growth in the western part of the inner Ariake Sea during winter. In order to develop the ecosystem model, we conducted field observation in the seaweed aquaculture filed and incorporated the effects of the seaweed aquaculture on the surrounding environment into the model. The seaweed aquaculture blocked light intensity about 77% on average, and this attenuation rate can be defined as a function of the LL. The numerical simulation with the developed ecosystem model reproduced coastal biochemical environment with high accuracy during winter. The phytoplankton budget analysis results by this numerical simulation showed that the favorable conditions for phytoplankton growth in the western part were caused firstly by optimal photosynthesis environment in terms of light conditions and secondly by supply due to horizontal advection in the lower layer from offshore area.

Appendix 5.A

Table 5.6 shows the formulations of biochemical processes in the ecosystem model. These formulations are based on Yamaguchi and Hayami (2018).

Appendix 5.B

Table 5.7 shows the values of biochemical parameters excluding phytoplankton (see Table 5.3) in the ecosystem model. These parameters are based on Yamaguchi and Hayami (2018).

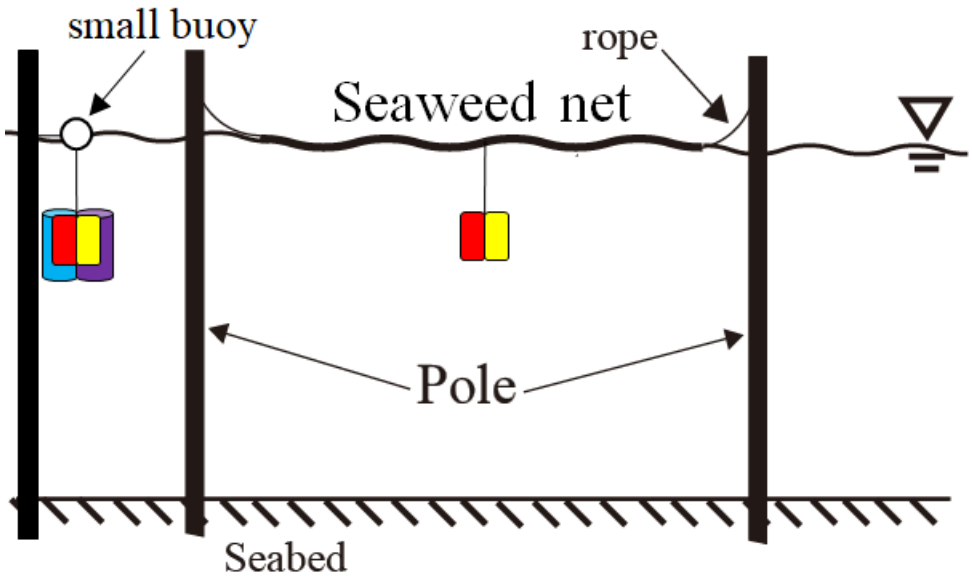

Fig. 5.1 Schematic diagram of the observation system in the seaweed aquaculture. Yellow square is light intensity measuring equipment (DEFI2-L by JFE Advantec Co.), red square is water depth measuring equipment (DEFI2-D10 by JFE Advantec Co.), light blue cylindrical column is water temperature and salinity measuring equipment (INFINITY ACTW-USB by JFE Advantec Co.) and purple cylindrical column is turbidity measuring equipment (INFINITY ACLW-USB by JFE Advantec Co.).

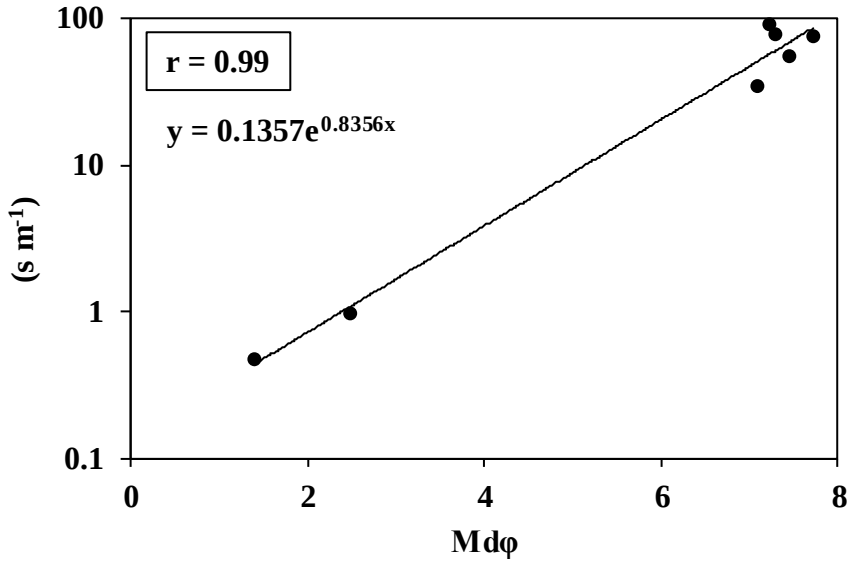

Fig. 5.2 Relationship between the parameterized erosion velocity coefficient and $Md\varphi$.

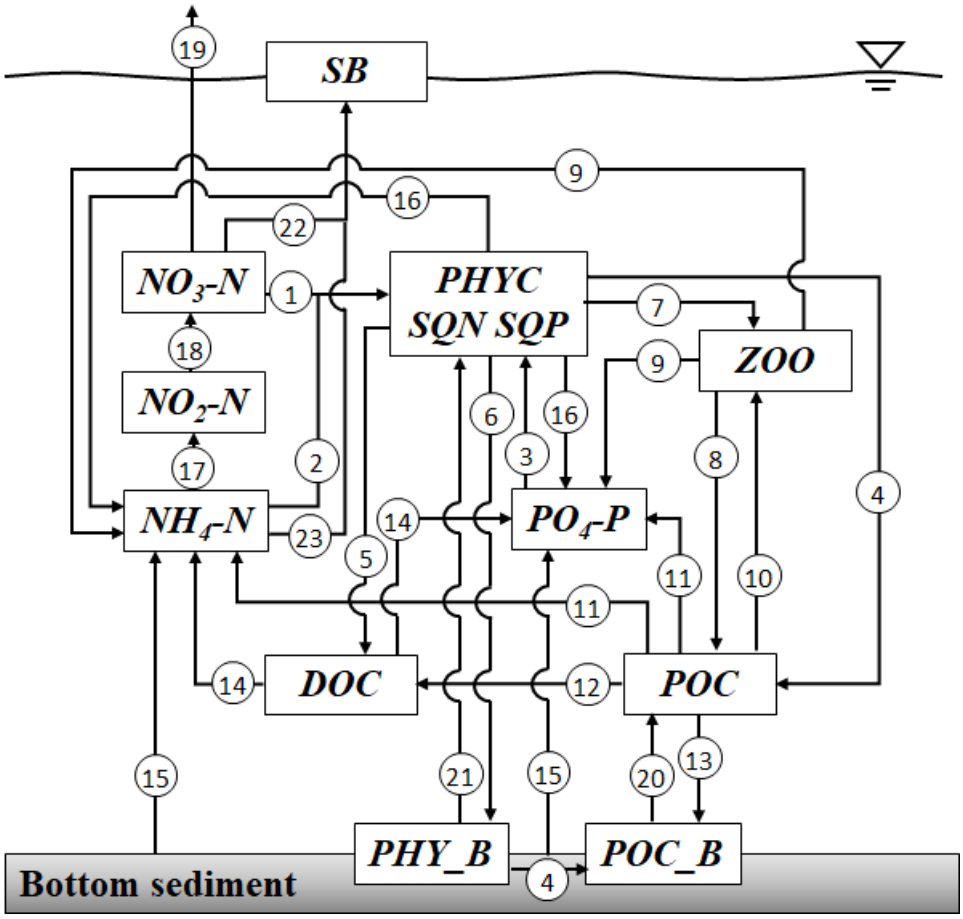

Fig. 5.3 Ecosystem diagram in the present ecosystem model. Model variables in boxes and arrows are defined in Table 5.1 and 5.2.

Table 5.1 Model variables in the present ecosystem model.

Variables	Definition	Unit
PHYC	Phytoplankton in C unit	mgC m^{-3}
SQN	Cell quota of phytoplankton nitrogen	mgN m^{-3}
SQP	Cell quota of phytoplankton phosphorus	mgP m^{-3}
ZOO	Zoo plankton	mgC m^{-3}
POC	Particulate organic matter in C unit	mgC m^{-3}
DOC	Dissolved organic matter in C unit	mgC m^{-3}
NO_3-N	Nitrate	μM
NO_2-N	Nitrite	μM
NH_4-N	Ammonium	μM
PO_4-P	Phosphate	μM
DO	Dissolved oxygen	mg l^{-1}
PHY_B	PHYC deposited on the seabed	mgC m^{-2}
POC_B	POC deposited on the seabed	mgC m^{-2}
SB	Seaweed	mg m^{-2}

Table 5.2 Description of each material process in the present ecosystem model.

No.	Definition
1	Uptake of nitrate by phytoplankton
2	Uptake of ammonia nitrogen by phytoplankton
3	Uptake of phosphate by phytoplankton
4	Natural mortality of phytoplankton
5	Extracellular release of DOC by phytoplankton
6	Sinking of phytoplankton
7	Grazing of phytoplankton by zooplankton
8	Natural mortality of zooplankton
9	Excretion of zooplankton
10	Grazing of POC by zooplankton
11	NH_4-N or PO_4-P release by decomposition of POC
12	DOC creation by decomposition surplus of POC
13	Sinking of POC
14	NH_4-N or PO_4-P release by decomposition of DOC
15	Release of nutrients from the seabed
16	Release of cell quota of phytoplankton by grazing of zooplankton
17	Nitrification of NH_4-N
18	Nitrification of NO_2-N
19	Denitrification
20	Resuspension of POC from the seabed
21	Resuspension of phytoplankton from the seabed
22	Uptake of nitrate by seaweed
23	Uptake of ammonia nitrogen by seaweed

Table 5.3 Parameters for phytoplankton in the present ecosystem model (References: [1] Eppley (1972), [2] Kaeriyama et al. (2011), [3] Yamaguchi and Hayami (2018), [4] Ono et al. (2006), [5] Tarutani (1999) and [6] Lomas and Glibert (2000). The asterisk mark (*) is the estimated value referred to the literature).

Parameters	Definitions	Unit	Value	References
[Phytoplankton]				
α_1	Maximum growth rate	day^{-1}	0.59	[1]
β_1	Temperature coefficient for growth		0.0633	[1]
α_2	Resporation rate	day^{-1}	0.083	[1]
β_2	Temperature coefficient for respiration		0.032	[1]
I_0	Threshold value of irradiance	$\mu mol\ m^{-2}\ s^{-1}$	5.9	[2]
K_S	Half saturation constant for irradiance	$\mu mol\ m^{-2}\ s^{-1}$	30	[2]
$[P:C]_{PHYC}$	Carbon:Phosphorus ratio		0.000806	[3]
$[N:C]_{PHYC}$	Carbon:Nitrogen ratio		0.011429	[3]
$[Chla:C]_{PHYC}$	Carbon:Chlorophyll-a ratio		0.0105	[3]
W_P	Sinking velocity	$m\ day^{-1}$	0.54	[4]*
m	Natural mortality rate	day^{-1}	0.05	[3]
β_m	Temperature coefficient for death		0.0693	[3]
UP_{MAX}	Maximum uptake rate for phosphorus	day^{-1}	240	[5]
UN_{MAX}	Maximum uptake rate for nitrogen	day^{-1}	2.4	[6]
$[TOD:C]_{PHYC}$	Carbon:DO ratio		0.00347	[3]
SQP_{MAX}	Maximum cell quota for phosphorus	µM	16	[3]
SQN_{MAX}	Maximum cell quota for nitrogen	µM	8	[3]
K_{PO4}	Half saturation constant for phosphorus uptake	µM	0.68	[5]
K_{NH4}	Half saturation constant for NH_4-N uptake	µM	0.8	[6]*
K_{NO3}	Half saturation constant for NO_3-N uptake	µM	0.4	[6]

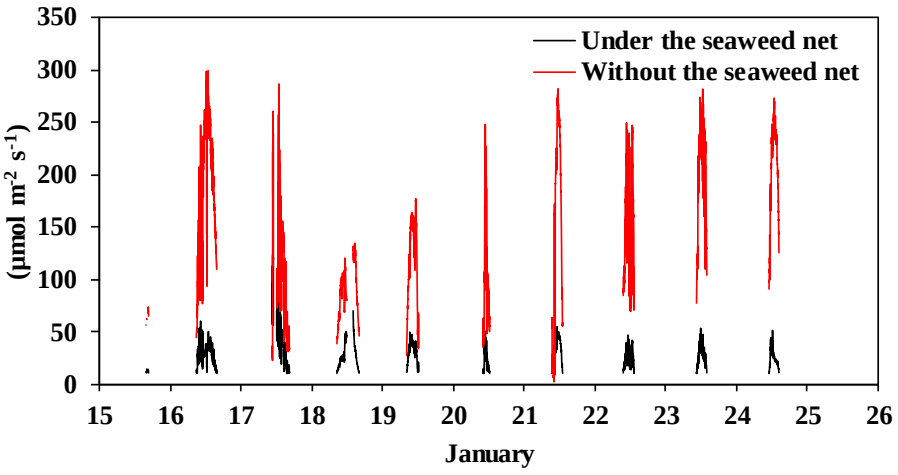

Fig. 5.4 Time series of the light intensity under the seaweed net and without the seaweed net.

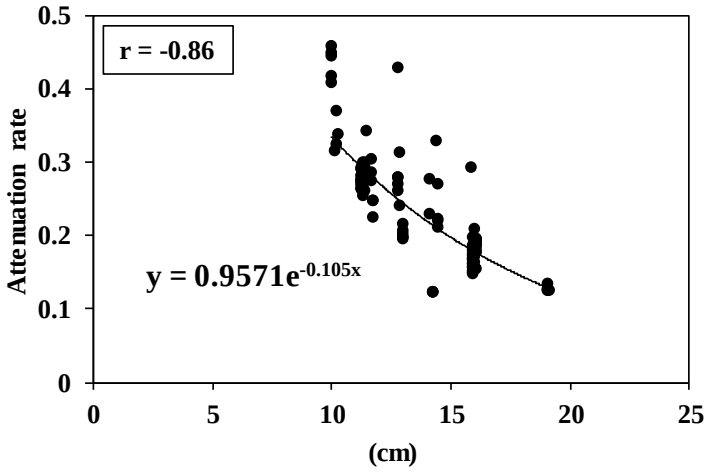

Fig. 5.5 Relationship between the attenuation rate and LL.

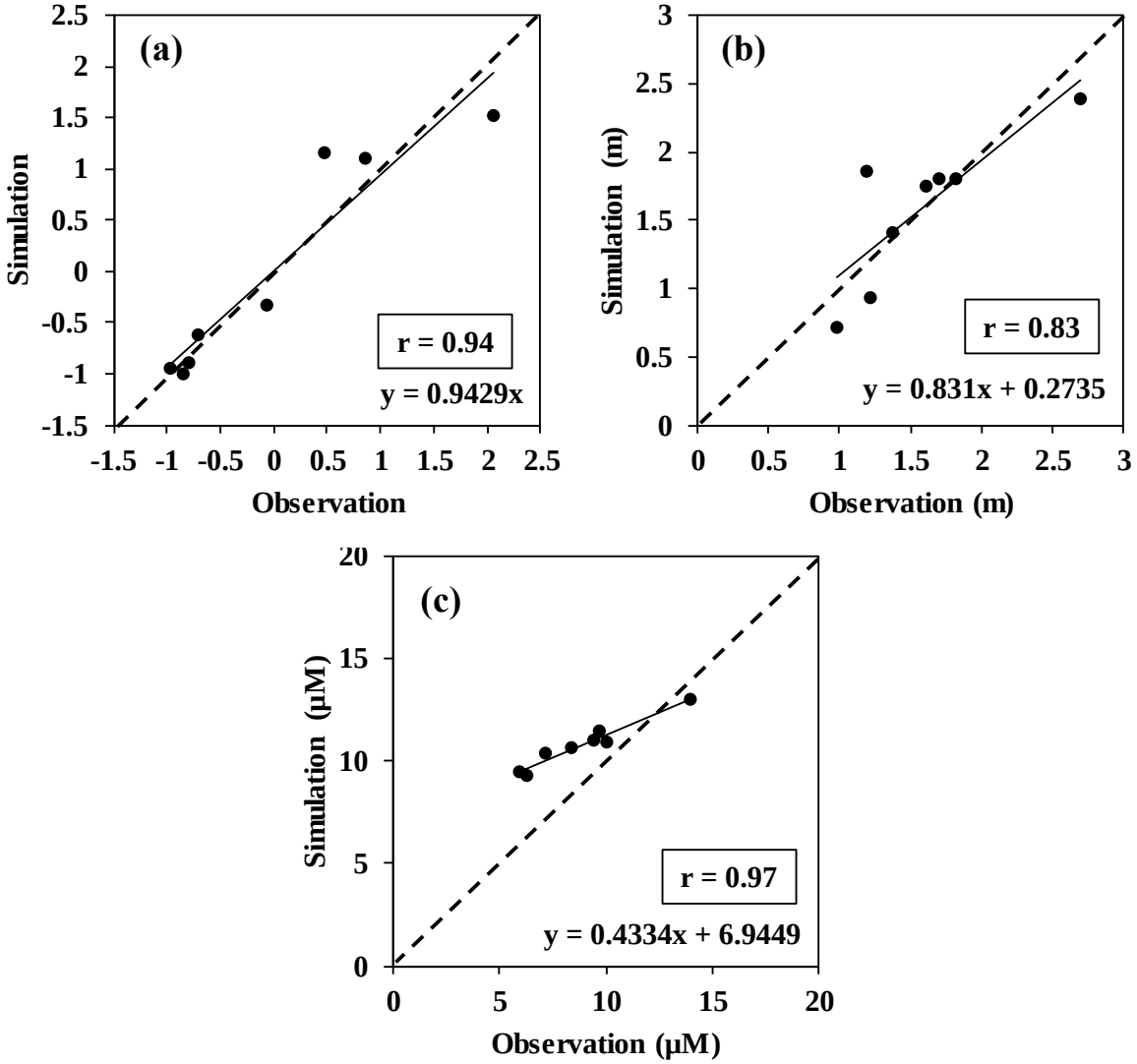

Fig. 5.6 Comparison of (a) surface phytoplankton, (b) transparency and (c) surface DIN between calculation and observation data. The surface phytoplankton data is transformed by standardization. The black dashed line is one-to-one straight line.

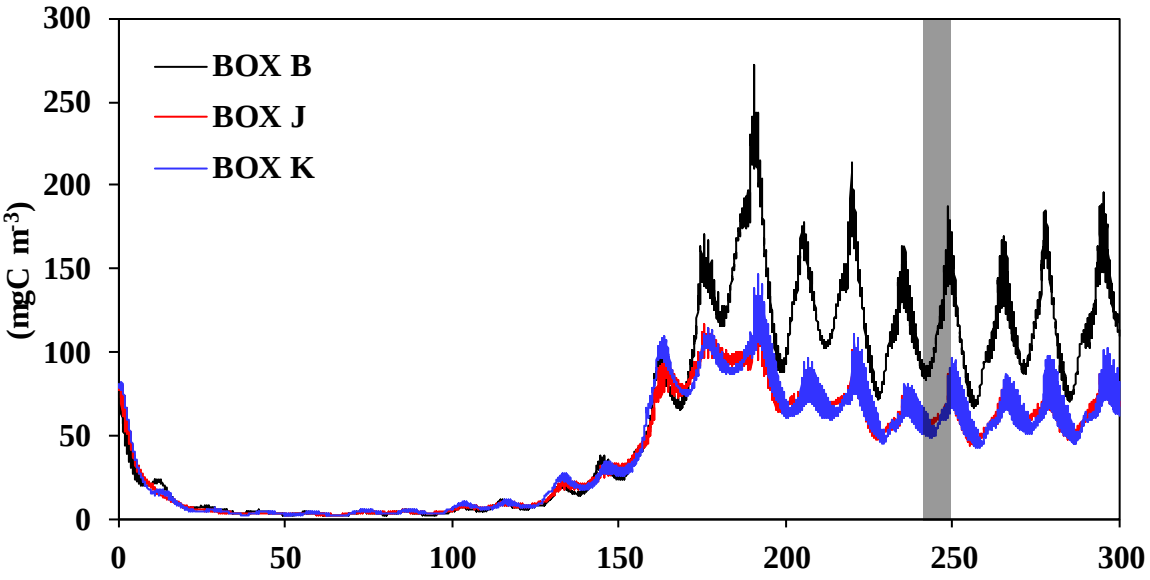

Fig. 5.7 Time series of the phytoplankton concentration in BOX B (black line), BOX J (red line) and BOX K (blue line) in the budge analysis calculation. Black-hatched area is time range for budget analysis.

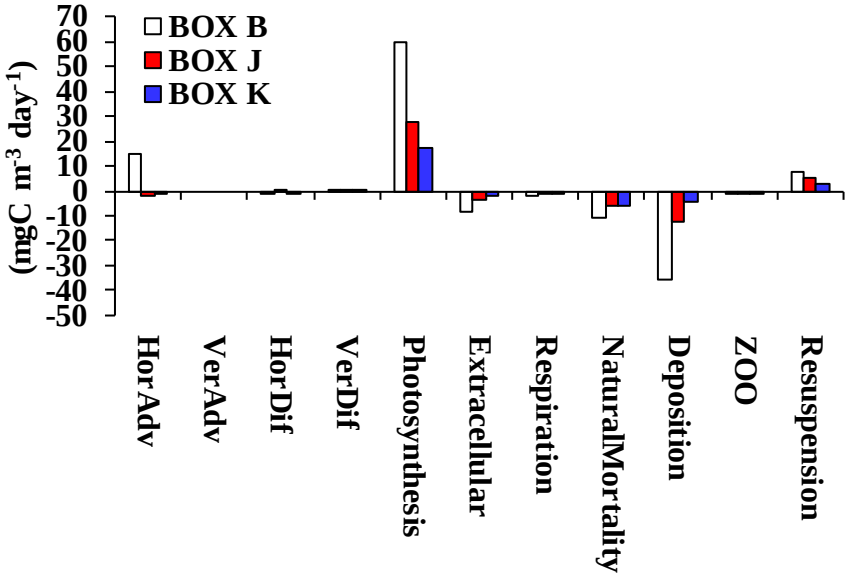

Fig. 5.8 Results of phytoplankton budget averaged during budget analysis period per day in BOX B (white bar), J (red bar) and K (blue bar). Positive (negative) value is inflow (outflow) or production (consumption) of phytoplankton.

Table 5.4 Comparison of the photosynthesis components (temperature, nutrient limitation and light limitation) averaged during budget analysis period in BOX B, J and K.

	Temparature	Nutrient Limitation	Light Limitation
BOX B	8.66	0.65	0.79
BOX J	9.73	0.66	0.63
BOX K	9.88	0.66	0.37

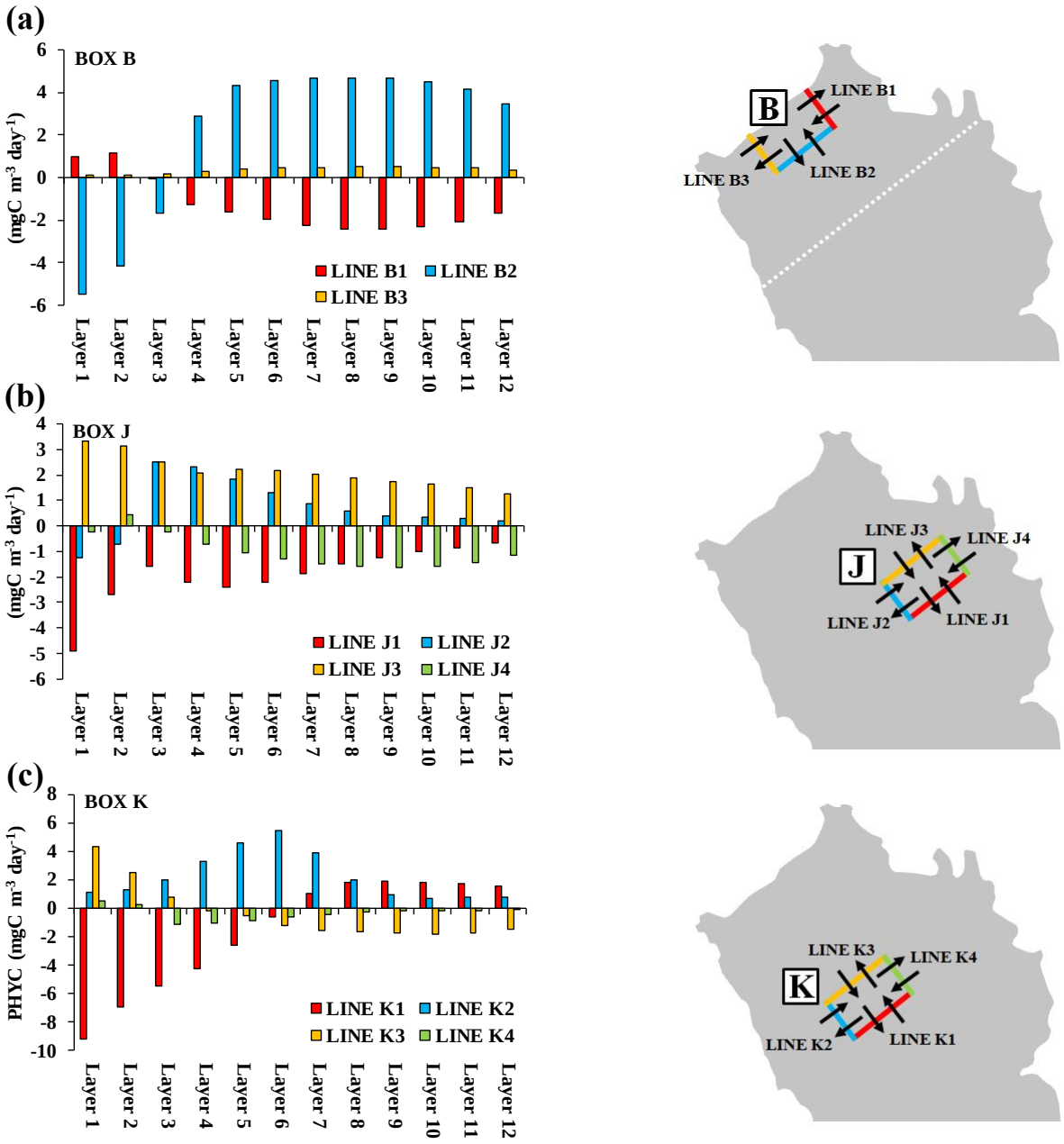

Fig. 5.9 Change in phytoplankton concentration due to horizontal advection in each direction and layer of (a) BOX B, (b) J and (c) K. Left panels are results of change in phytoplankton concentration and right panels are location of calculation lines. Positive (negative) value is inflow (outflow) of phytoplankton concentration in each box.

Table 5.5 Comparison of the AML, ELD and ELD/AML ratio averaged during each budget analysis period in BOX B, J and K.

	AML	ELD	ELD/AML raito
BOX B	1.93	7.74	4.01
BOX J	1.99	5.65	2.84
BOX K	5.79	6.70	1.16

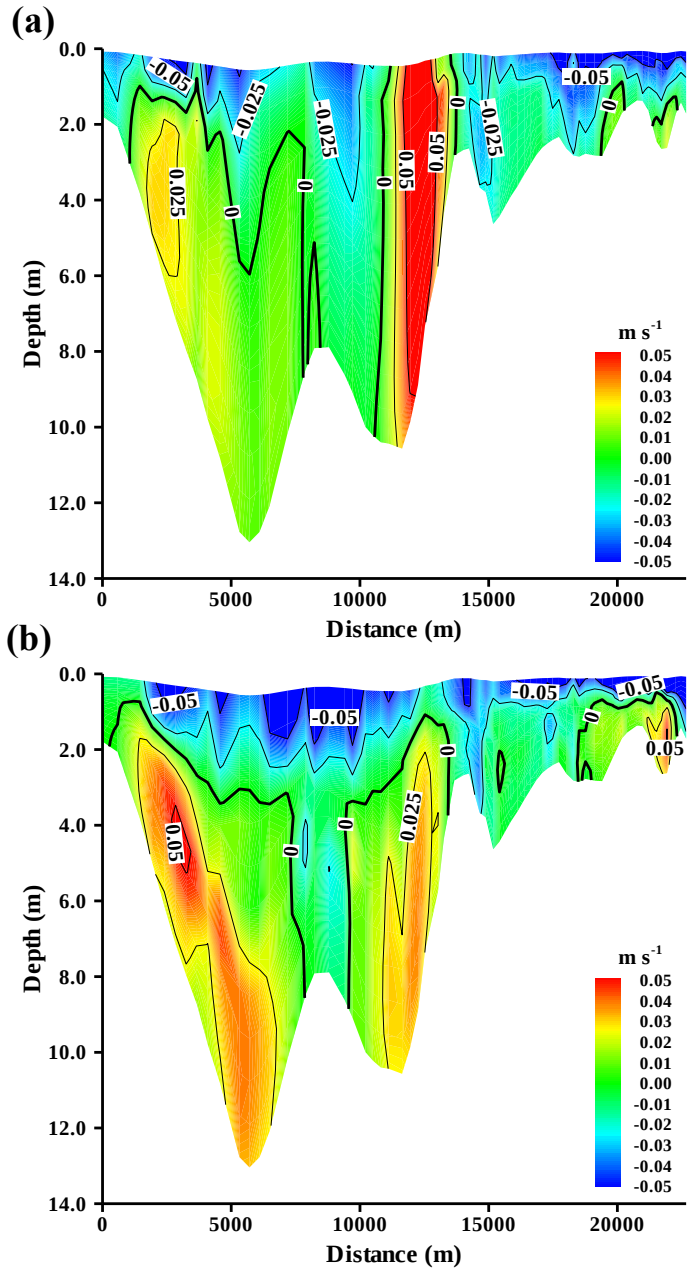

Fig. 5.10 Cross section of the residual current along the white dash line in Fig. 5.9a at the (a) spring and (b) neap tide. Positive (negative) value is inflow (outflow) in the inner Ariake Sea.

Table 5.6 Formulations of the present ecosystem model.

Processes	Formulations	Parameters (Table B)
[Phytoplankton in water colume: PHYC]	$\frac{\partial PHYC}{\partial t} = B_1 - B_3 - B_4 - B_5 - B_7 - B_8 + B_{24}$	
B_1: Phytosynthesis	$B_1 = \alpha_1 \cdot \exp(\beta_1 \cdot T) \cdot \mu_1 \cdot \mu_2 \cdot PHYC$	α_1, β_1
Nutrient limitation	$\mu_1 = \min\left(\frac{SQP}{SQP + [P:C]_{PHYC} \cdot PHYC}\right), \left(\frac{SQN}{SQN + [N:C]_{PHYC} \cdot PHYC}\right)$	$[P:C]_{PHYC}$, $[N:C]_{PHYC}$
Light limitation	$\mu_2 = \left(\frac{I - I_0}{(K_S - I_0) - (I - I_0)}\right)$	I_0, K_S
Light intensity	$I = I_{SUR} \cdot \exp(-K \cdot dep)$ I_0 : Threshold value of irradiance (μmol m^{-2} s^{-1}) K_S : Half saturation constant for irradiance (μmol m^{-2} s^{-1}) I_{SUR} : Light intensity at the sea surface (μmol m^{-2} s^{-1}) K : Attenuation coefficient (m^{-1}) dep : Depth (m)	
B_3: Extracellular release	$B_3 = 0.135 \cdot \exp(-0.00201 \cdot [Chla:C]_{PHYC} \cdot PHYC) \cdot PHYC$	$[Chla:C]_{PHYC}$
B_4: Feeding by zooplankton	See zooplankton section in this table	
B_5: Respiration	$B_5 = \alpha_2 \cdot \exp(\beta_2 \cdot T) \cdot PHYC$	α_2, β_2
B_7: Natural mortality	$B_7 = m \cdot \exp(\beta_m \cdot T) \cdot PHYC$	m, β_m
B_8: Sinking	$B_8 = W_P \cdot \frac{\partial PHYC}{\partial z}$	W_P
B_{24}: Resuspention from the seabed	See PHY_B section in this table	
[Phytoplankton on the seabed: PHY_B]	$\frac{\partial PHY\_B}{\partial t} = B_8 - B_{24} - B_{26}$	
B_{24}: Resuspention from the seabed	$B_{24} = PHY\_B \cdot \frac{RBS}{TBS}$ TBS: Total bottom sediment deposited on the seabed (mg l^{-1}) RBS: Resuspended sediment (mg l^{-1})	
B_{26}: Natural mortality	$B_{26} = m \cdot \exp(\beta_m \cdot T_B) \cdot PHY\_B$ T_B: Water temperature in the lowest σ layer (℃)	
[Cell quota of Nitrogen:SQN]	$\frac{\partial SQN}{\partial t} = B_2^{NO3} + B_2^{NH4} - [N:C]_{PHYC} \cdot B_1 - (B_4 + B_7 + B_8) \cdot \frac{SQN}{PHYC} + B_{32n}$	
[Cell quota of Phosphorus:SQP]	$\frac{\partial SQP}{\partial t} = B_2^{PO4} - [P:C]_{PHYC} \cdot B_1 - (B_4 + B_7 + B_8) \cdot \frac{SQP}{PHYC} + B_{32p}$	
B_2: Uptake of nutrients		
Nitrate	$B_2^{NO3} = UN_{MAX} \cdot \frac{NO_3}{K_{NO3} + NO_3} \cdot \exp(-1.462 \cdot NH_4 \cdot 14.0) \cdot \left(SQN_{MAX} - \frac{[N:C]_{PHYC} \cdot PHYC + SQN}{[N:C]_{PHYC} \cdot PHYC} / (SQN_{MAX} - 1)\right) \cdot PHYC$	UN_{MAX}, K_{NO3}, SQN_{MAX}
Ammonia	$B_2^{NH4} = UN_{MAX} \cdot \frac{NH_4}{K_{NH4} + NH_4} \cdot \left(SQN_{MAX} - \frac{[N:C]_{PHYC} \cdot PHYC + SQN}{[N:C]_{PHYC} \cdot PHYC} / (SQN_{MAX} - 1)\right) \cdot PHYC$	K_{NH4}
Phosphorus	$B_2^{PO4} = UP_{MAX} \cdot \frac{PO_4}{K_{PO4} + PO_4} \cdot \left(SQP_{MAX} - \frac{[P:C]_{PHYC} \cdot PHYC + SQP}{[P:C]_{PHYC} \cdot PHYC} / (SQP_{MAX} - 1)\right) \cdot PHYC$	UP_{MAX}, K_{PO4}, SQP_{MAX}
B_{32n}, B_{32p}: Resuspended from the seabed	See SQN_B, SQP_B section in this table	
[SQN on the seabed: SQN_B]	$\frac{\partial SQN\_B}{\partial t} = B_{8n} - B_{26n} - B_{32n}$	
B_{8n}: Deposition of SQN on seabed	$B_{8n} = [N:C]_{PHYC} \cdot B_8$	
B_{26n}: Natural mortality	$B_{26n} = m \cdot \exp(\beta_m \cdot T_B) \cdot PHY\_B \cdot [N:C]_{PHYC}$	
B_{32n}: Resuspention from the seabed	$B_{32n} = SQN\_B \cdot \frac{RBS}{TBS}$	
[SQP on the seabed: SQP_B]	$\frac{\partial SQP\_B}{\partial t} = B_{8p} - B_{26p} - B_{32p}$	
B_{8p}: Deposition of SQP on seabed	$B_{8p} = [P:C]_{PHYC} \cdot B_8$	
B_{26p}: Natural mortality	$B_{26p} = m \cdot \exp(\beta_m \cdot T_B) \cdot PHY\_B \cdot [P:C]_{PHYC}$	
B_{32p}: Resuspention from the seabed	$B_{32p} = SQP\_B \cdot \frac{RBS}{TBS}$	

Table 5.6 (continued).

Processes	Formulations	Parameters (Table B)
[Zooplankton: ZOO]	$\frac{\partial ZOO}{\partial t} = B_4 + B_9 - B_{10} - B_{11} - B_{12} - B_{13}$	
B_4: Grazing of PHYC	$B_4 = E_{ZOO} \cdot \frac{PHYC}{PHYC + POC} \cdot V_4 \cdot ZOO$ $V_4 = \alpha_3 \cdot \exp(\beta_3 \cdot T) \cdot [1 - \exp\{\lambda(\Pi^* - PHYC - POC)\}]$	E_{ZOO}, α_3, β_3, λ, Π^*
B_9: Grazing of POC	$B_9 = E_{ZOO} \cdot \frac{POC}{PHYC + POC} \cdot V_4 \cdot ZOO$	
B_{10}: Faces	$B_{10} = (1 - E_{ZOO}) \cdot (B_4 + B_9)$	
B_{11}: Excretion	$B_{11} = (\alpha_4 \cdot \exp(\beta_4 \cdot T) + \eta \cdot V_4) \cdot ZOO$	α_4, β_4, η
B_{12}: Natural mortality	$B_{12} = \delta_Z \cdot \exp(\delta_T \cdot T) \cdot ZOO$	δ_Z, δ_T
B_{13}: Diel vertical migration	$B_{13} = W_{ZOO} \cdot \frac{\partial ZOO}{\partial Z}$ $Day\ Time:\ W_{ZOO} = W_{DOWN} \cdot \sin\left(\frac{\pi}{DL} \cdot t\right)$ $Night\ Time:\ W_{ZOO} = W_{UP} \cdot \sin\left(\frac{\pi}{1 - DL} \cdot (t - DL)\right)$	W_{DOWN}, W_{UP}
[Particulate organic carbon: POC]	$\frac{\partial POC}{\partial t} = B_7 + B_{10} + B_{12} - B_9 - B_{14} - B_{15} - B_{16} + B_{25} + Q_{POC}$ Q_{POC}:Load from rivers	
B_{14}: Mineralization	$B_{14} = \alpha_5 \cdot \exp(\beta_5 \cdot T) \cdot \frac{DO}{DO0 + DO} \cdot POC$	α_5, β5, DO0
B_{15}: Decomposition surplus	$B_{15} = \kappa \cdot B_{14}$	κ
B_{16}: Sinking	$B_{16} = W_{POC} \cdot \frac{\partial POC}{\partial z}$	W_{POC}
B_{25}: Resuspended from the seabed	See POC_B section in this table	
[POC on the seabed: POC_B]	$\frac{\partial POC\_B}{\partial t} = B_{16} + B_{26} - B_{25} - B_{27}$	
B_{16}: Sinking in the lowest σ layer	See POC section in this table	
B_{25}: Resuspended from the seabed	$B_{25} = POC\_B \cdot \frac{RBS}{TBS}$	
B_{27}: Decomposition	$B_{27} = \alpha_5 \cdot \exp(\beta_5 \cdot T_B) \cdot \frac{DO_B}{DO0 + DO_B} \cdot POC\_B$ DO_B: DO in the lowest σ layer (mg l^{-1})	
[Dissolved organic carbon: DOC]	$\frac{\partial DOC}{\partial t} = B_3 + B_{15} - B_{17} + Q_{DOC}$ Q_{DOC}: Load from rivers	
B_{17}: Mineralization	$B_{17} = \alpha_6 \cdot \exp(\beta_6 \cdot T) \cdot \frac{DO}{DO1 + DO} \cdot DOC$	α_6, β_6, DO1
[Dissolved inorganic phosphorus: DIP]	$\frac{\partial PO_4}{\partial t} = -B_2^{PO_4} + [P:C]_{ZOO} \cdot B_{11} + [P:C]_{POC} \cdot B_{14}$ $+[P:C]_{DOC} \cdot B_{17} + (B_4 + B_7) \cdot \frac{SQP}{PHYC} + B_{28} + Q_{PO_4}$ Q_{PO4}: Load from rivers	$[P:C]_{ZOO}$, $[P:C]_{POC}$, $[P:C]_{DOC}$
B_{28}: Release from bottom sediment	$B_{28} = \alpha_9 \cdot IL^{\gamma_P} \cdot \frac{\exp\left(\beta_9 \cdot (T_B - T_{EXP\_P})\right)}{h_B}$ IL: Ignition loss of bottom sediment h_B: Thickness of lowest σ layer T_{EXP_P}: Temperature at experimental time for phosphorus (℃)	α_9, γ_P, β_9, T_{EXP}
[Dissolved inorganic nitrogen: DIN]	$\frac{\partial NH_4}{\partial t} = -B_2^{NH4} + [N:C]_{ZOO} \cdot B_{11} + [N:C]_{POC} \cdot B_{14}$ $+[N:C]_{DOC} \cdot B_{17} + (B_4 + B_7) \cdot \frac{SQN}{PHYC} - B_{18} + B_{29} - BLN_{NH4} + Q_{NH4}$ $\frac{\partial NO_2}{\partial t} = B_{18} - B_{19} + Q_{NO_2}$ $\frac{\partial NO_3}{\partial t} = -B_2^{NO3} + B_{19} - B_{20} - BLN_{NO3} + Q_{NO3}$ Q_{NH4},Q_{NO2},Q_{NO3}: Load from rivers	$[N:C]_{ZOO}$, $[N:C]_{POC}$, $[N:C]_{DOC}$
B_{18}: Nitrification of ammonia	$B_{29} = \alpha_{10} \cdot IL^{\gamma_N} \cdot \frac{\exp\left(\beta_{10} \cdot (T_B - T_{EXP\_N})\right)}{h_B}$ T_{EXP_N}: Temperature at experimental time for NH_4 (℃)	α_{11}, β_{11}, DO2
B_{29}: Release from bottom sediment	$B_{18} = \alpha_{11} \cdot \exp(\beta_{11} \cdot T) \cdot \frac{DO}{DO2 + DO} \cdot NH_4$	α_{10}, γ_N, β_{10}, T_{ave}
B_{19}: Nitrification of nitrite	$B_{19} = \alpha_{12} \cdot \exp(\beta_{12} \cdot T) \cdot \frac{DO}{DO3 + DO} \cdot NO_2$	α_{12}, β_{12}, DO3
B_{20}: Denitrification (DO < DO4)	$B_{20} = \alpha_{13} \cdot \exp(\beta_{13} \cdot T) \cdot NO_3$	α_{13}, β_{13}, DO4
B_{33}: Uptake of nutrients from seaweed	See SB section in this table	

Table 5.6 (continued).

Processes	Formulations	Parameters (Table B)
[Dissolved oxygen: DO]	$\frac{\partial DO}{\partial t} = D_1 - D_2 - D_3 - D_4 - D_5 - D_6 - D_7 - D_8 + D_9 - D_{10}$	
D_1: Production by photosynthesis	$D_1 = [TOD:C]_{PHYC} \cdot B_1$	$[TOD:C]_{PHYC}$
D_2: Respiration by phytoplankton	$D_2 = [TOD:C]_{PHYC} \cdot B_5$	
D_3: Respiration by zooplankton	$D_3 = [TOD:C]_{ZOO} \cdot B_1$	$[TOD:C]_{ZOO}$
D_4: Decomposition of POC	$D_4 = [TOD:C]_{POC} \cdot B_1$	$[TOD:C]_{POC}$
D_5: Decomposition of DOC	$D_5 = [TOD:C]_{DOC} \cdot B_1$	$[TOD:C]_{DOC}$
D_6: Ammonia nitrification	$D_6 = 0.048 \cdot B_{18}$	
D_7: Nitrite nitrification	$D_7 = 0.016 \cdot B_{19}$	
D_8: Bottom sediment	$D_8 = \alpha_D \cdot \exp(\beta_D \cdot (T_B - 28.0)) \cdot \frac{\exp(\beta_I \cdot IL)}{h_R} \cdot \frac{DO_B}{DO5 + DO_B}$	α_D, β_D, β_I, DO5
D_9: Reaeration at sea surface	$D_9 = K_R \cdot \frac{(DOS - DO)}{h_S}$	K_R
	$DOS = \frac{32 \cdot O2}{22.4 \cdot \left(1 + \frac{T_S}{273}\right)}$ h_S: Thickness of surface σ layer; DOS: Saturated concentration of DO (mg l^{-1})	
	$O2 = 10.291 - 0.2809 \cdot T_S + 0.006009 \cdot T_S^2 - 0.000063 \cdot T_S^3 - Cl \cdot (0.1161 - 0.003922 \cdot T_S + 0.0000631 \cdot T_S^2)$ CL: Chlorinity	
[Seaweed: SB]	Not consider the change of seaweed density because of the steady state calculation	
BSN: Uptake of nutrients		
Nitrate	$BSN_{NO3} = \alpha^S_{NO3} \cdot \mu^S_{NO3} \cdot \mu^S_S \cdot SB$ SB: Seaweed density (mg m^{-2})	
	$\alpha^S_{NO3} = 10^{-32.464X^2 + 227.45X - 401.36}$	
	$\mu^S_{NO3} = \frac{NO_3}{K^S_{NO3} + NO_3}$	
	$K^S_{NO3} = 10^{-37.051X^2 + 257.5X - 445.69}$	
Ammonia	$BSN_{NH4} = \alpha^S_{NH4} \cdot \mu^S_{NH4} \cdot \mu^S_S \cdot SB$	
	$\alpha^S_{NH4} = 10^{-29.642X^2 + 206.93X - 363.23}$	
	$\mu^S_{NH4} = \frac{NH_4}{K^S_{NH4} + NH_4}$	
	$K^S_{NH4} = 10^{-39.556X^2 + 276.17X - 479.77}$	
	$X = \left(\frac{1}{T_S + 273.15}\right) \times 10^3$	
	$\mu^S_S = 0.013 + \left(\frac{33.01}{26.73\sqrt{\frac{\pi}{2}}}\right) \exp\left(\frac{-2(S_S - 28.98)^2}{26.73^2}\right)$ T_S: Water temperature in the surface σ layer (℃); S_S: Salinity in the surface σ layer	

Table 5.7 Parameters of the present ecosystem model excluding phytoplankton.

Parameters	Definitions	Unit	Value
[Zooplankton]			
E_{ZOO}	Assimilation efficiency		0.7
α_3	Maxmum growth rate	day^{-1}	0.18
β_3	Temperature coefficient for growth		0.0693
λ	Ivlev's constant		0.01
Π^*	Threshold value for food concentration	$mgC\ m^{-3}$	50
α_4	Resporation rate	day^{-1}	0.0214
β_4	Temperature coefficient for respiration		0.0637
η	Energy consumption for respiration		0.4
δ_Z	Death rate	day^{-1}	0.02
δ_T	Temperature coefficient for death		0.0693
W_{UP}	Velocity of diurnal vertical movement (upward)	$m\ day^{-1}$	0
W_{DOWN}	Velocity of diurnal vertical movement (downward)	$m\ day^{-1}$	0
$[P:C]_{ZOO}$	Carbon:Phosphorus ratio		0.02857
$[N:C]_{ZOO}$	Carbon:Nitrogen ratio		0.22222
$[TOD:C]_{ZOO}$	Carbon:DO ratio		0.00351
[Particulate organic carbon]			
α_5	Decomposition rate of POC at 0 ℃	day^{-1}	0.0453
β_5	Temperature coefficient for POC decomposition		0.07
DO0	Half saturation constant of DO for POC decomposition	$mg\ l^{-1}$	1
κ	DOC release ratio from POC decomposition		0.25
W_{POC}	Sinking velocity of POC	$m\ day^{-1}$	0.432
$[P:C]_{POC}$	Carbon:Phosphorus ratio in POC		0.0005048
$[N:C]_{POC}$	Carbon:Nitrogen ratio in POC		0.009921
$[TOD:C]_{POC}$	Carbon:DO ratio in POC		0.0033
[Dissolved organic carbon]			
α_6	Decomposition rate of DOC at 0 ℃	day^{-1}	0.00434
β_6	Temperature coefficient for DOC decomposition		0.0693
DO1	Half saturation constant of DO for DOC decomposition	$mg\ l^{-1}$	1
$[P:C]_{DOC}$	Carbon:Phosphorus ratio in DOC		0.0002581
$[N:C]_{DOC}$	Carbon:Nitrogen ratio in DOC		0.007143
$[TOD:C]_{DOC}$	Carbon:DO ratio in DOC		0.00312

Table 5.7 (continued).

Parameters	Definitions	Unit	Value
[Dissolved inorganic phosphorus]			
α_9	Release rate of phosphorus from the seabed at 28 ℃	$mgP \cdot m^{-2} \cdot day^{-1}$	0.0453
β_9	Temperature coefficient for phosphorus release from the seabed		0.1353
γ_P	Coefficient of ignition loss for phosphorus release from the seabed		1.8434
T_{EXP_P}	Temperature at the time of experiment for phosphorus		21.6
[Dissolved inorganic nitrogen]			
α_{10}	Release rate of NH_4-N from the seabed at 28 ℃	$mgN \cdot m^{-2} \cdot day^{-1}$	0.3372
β_{10}	Temperature coefficient for NH_4-N release from the seabed		0.0392
γ_N	Coefficient of ignition loss for NH_4-N release from the seabed		2.3749
T_{EXP_N}	Temperature at the time of experiment for NH_4-N		26
α_{11}	Nitrification rate of NH_4-N at 0 ℃	day^{-1}	0.003
β_{11}	Temperature coefficient for NH_4-N nitrification		0.0693
DO2	Half saturation constant of DO for NH_4-N nitrification	$mg\ l^{-1}$	0.5
α_{12}	Nitrification rate of NO_2-N at 0 ℃	day^{-1}	0.0035
β_{12}	Temperature coefficient for NO_2-N nitrification		0.0693
DO3	Half saturation constant of DO for NO_2-N nitrification	$mg\ l^{-1}$	0.5
α_{13}	Denitrification rate of NO_3-N at 0 ℃	day^{-1}	0.00155
β_{13}	Temperature coefficient for denitrification		0.0932
DO4	Threshold of DO for denitrification	$mg\ l^{-1}$	2.5
[Dissolved oxygen]			
α_D	DO consumption rate of bottom sediment at 28 ℃	day^{-1}	0.00155
β_D	Temperature coefficient for DO consumption of bottom sediment		0.0932
β_I	Temperature coefficient for ignition loss		0.1794
DO5	Half saturation constant of DO for DO consumption by seabed		0.0377
K_R	Reaeration rate constant	day^{-1}	0.7

References

Eppley RW (1972) Temperature and phytoplankton growth in the sea. Fishery Bulletin 70(4):1067-1085

Galperin B, Kantha LH, Hassid S, Rosati A (1988) A quasi-equilibrium turbulent energy model for geophysical flows. Journal of the Atmospheric Science 45:55-62

Hamada T, Yamamoto K, Hayami Y, Yoshino K, Ohgushi K, Yamaguchi S, Katano T, Yoshida M (2009) Numerical simulation of sediment transport in the Ariake Sea with erosion property mapping. Journal of Japan Society of Civil Engineers, Series B2 (Coastal Engineering) 65(1):986-990 (**Japanese with English abstract**)

Hanawa K, Mitsudera H (1985) On daily average of oceanographic data. Bulletin on Coastal Oceanography 23(1):79-87 (**Japanese**)

Hopkins JE, Palmer MR, Poulton AJ, Hickman AE, Sharples J (2021) Control of a phytoplankton bloom by wind-driven vertical mixing and light availability. Limnology and Oceanography 66:1926-1949

Kaeriyama H, Katsuki E, Otsubo M, Yamada M, Ichimi K, Tada K, Harrison PJ (2011) Effects of temperature and irradiance on growth of Strains belonging to seven *Skeletonema* species isolated from Dokai Bay, southern Japan. European Journal of Phycology 46(2):113-124

Kasai A, Hill AE, Fujiwara T, Simpson JH (2000) Effect of the Earth's rotation on the circulation in regions of freshwater influence. Journal of Geophysical Research 105(7) 16961-16969

Katano T, Yoshino K, Ito Y, Hayami Y (2013) Seasonal changes in phytoplankton community in the inner part of Ariake Sea: occurrence of harmful blooms in summer and winter with reference to environmental conditions. Bulletin on Coastal Oceanography 51(1):53-64 (**Japanese with English abstract**)

Kawaguchi O, Yamamoto T, Matsuda O, Hashimoto T (2005) Evaluation of various environmental factors on the nutrient uptake competition between nori laver and planktonic diatoms in Ariake Bay, Japan. Oceanography in Japan 14(3):411-427 (**Japanese with English abstract**)

Lomas MW, Glibert PM (2000) Comparisons of nitrate uptake, storage, and reduction in marine diatoms and flagellates. Journal of Phycology 36:903-913

Masuda Y, Yamada H, Yokoo K, Kawamura Y (2014) Changes of the water content rate and the thickness of cell wall in Nori Thalli on every harvest. Study Report of Saga Prefectural Ariake Fisheries Research and Development Center 27:55-59 (**Japanese**)

Matsubara T, Yokoo K, Kawamura Y (2014) The role of environmental factors in the population dynamics of the harmful diatom *Asteroplanus karianus* in the Ariake Sea, off Saga Prefecture, Japan. Nippon Suisan Gakkaishi 80(2):222-232 (**Japanese with English abstract**)

Mellor GL, Yamada T (1982) Development of a turbulence closure model for geophysical fluid problem. Reviews of Geophysics and Space Physics 20(4):851-875

Ministry of Agriculture, Forestry and Fisheries (2003) The 5th mid and long-term opening survey meeting document 1: The distributions of resting cell in harmful phytoplankton in Ariake Sea. https://www.maff.go.jp/j/study/other/kaimon/05/pdf/data1.pdf (**Japanese**)

Ministry of the Environment (2002) Report of supplemental survey on water quality in Ariake Sea. p 129 (**Japanese**)

Miyazawa Y, Zhang R, Guo X, Tamura H, Ambe D, Lee JS, Okuno A, Yoshinari H, Setou T, Komatsu K (2009) Water mass variability in the western North Pacific detected in a 15-year eddy resolving ocean reanalysis. Journal of Oceanography 65(6):737-756

Ono A, Ichimi K, Tada K (2006) The standing stock and sinking rate of the large diatom *Coscinodiscus wailesii* causing Nori (*Porphyra*) discoloration. Bulletin of the Society of Sea Water Science, Japan 60:253-259 (**Japanese with English abstract**)

Sarno D, Kooistra W, Medlin LK, Percopo I, Zingone A (2005) Diversity in the genus *Skeletonema* (Bacillariophyceae). II. An assessment of the taxonomy of *S. costatum*-like species with the description of four new species. Journal of Phycology 41:151-176

Sarno D, Kooistra W, Balzano S, Hargraves PE, Zingone A (2007) Diversity in the genus *Skeletonema* (Bacillariophyceae): III. Phylogenetic position and morphological variability of *Skeletonema costatum* and *Skeletonema grevillei*, with the description of *Skeletonema ardens* sp. nov. Journal of Phycology 43:156-170

Smagorinsky J (1963) General circulation experiments with the primitive equations, I. The basic experiment. Mon Weather Rev 91:99-164

Tarutani K (1999) Ecophysiological studies on the population dynamics of toxic dinoflagellate *Alexandrium tamarense*. Bulletin of Fisheries and Environment of Inland Sea 1:63-96 (**Japanese with English abstract**)

Yamaguchi A, Matsubara T, Masuda Y, Mine T, Ito S (2017) The role of a high nutrient and high chlorophyll water mass in the Kashima estuary on the dynamics of winter diatom blooms in coastal areas in the inner western part of Ariake Bay. Bulletin on Coastal Oceanography 54(2):193-201 (**Japanese with English abstract**)

Yamaguchi S, Hayami Y (2018) Impact of Isahaya dike construction on DO concentration in the Ariake Sea. Journal of Oceanography 74(6):565-586

Yamamoto K, Yoshino K, Hayami Y, Kasagi T, Harada H, Hamada T, Ohgushi K, Yamada F, Yamaguchi S, Yokoyama K (2008) Study of bottom sediment in the inner part of the Ariake

Sea - For the modelling of suspended sediment transport and explanation of the accumulation of fine particles -. Report of Ariake Sea Research Project, Saga University 4:1-8 (**Japanese with English abstract**)

Yamamoto K, Hayami Y, Kasagi T, Hamada T, Yoshino K, Ohgushi K, Hirakawa R, Yokoyama K (2009) Estimation of the parameters for erosion of the cohesive sediment in the inner part of the Ariake Bay and Isahaya Bay. Environmental Engineering Research 46:613-621 (**Japanese with English abstract**)

Yamamoto T, Takao M (1988) Effect of temperature on the uptake kinetics of ammonia-N and nitrate-N by *Porphyra yezoensis* thalli. The Japanese Journal of Phycology 36(1):37-42 (**Japanese with English abstract**)

Zingone A, Percopo I, Sims PA, Sarno D (2005) Diversity in the genus *Skeletonema* (Bacillariophyceae). I. A reexamination of the type material of *S. costatum* with the description of *S. grevillea* sp. nov. Journal of Phycology 41:140-150

Chapter 6

Summary and Conclusions

The purpose of this study was to reveal the mechanism of phytoplankton outbreaks in the western part of the inner Ariake Sea by using both of field observations and numerical simulations. In order to clarify the mechanism, we established a new observation approach to grasp the detailed spatial distribution of phytoplankton outbreaks, and developed a numerical ecosystem model to estimate such phenomena accurately. The results and findings obtained from this study are summarized as follows:

In Chapter 1, we described the background, purpose and outline of this thesis. We also stated the importance of revealing the mechanism of phytoplankton outbreaks, and the contents in the respective chapters in this thesis.

In Chapter 2, we investigated the mechanism of phytoplankton outbreaks which occurred at the first neap tide after the annual minimum water temperature by continuous mooring observation in the western part of the inner Ariake Sea during winter. The formation of two physical environmental factors favorable for phytoplankton proliferation was found to play a trigger role in the outbreaks. The first factor was the stabilization of water column due to net heat flux transition at the sea surface from cooling to heating in mid-winter. After mid-January, the atmosphere stabilized as the air temperature exceeded the water temperature, and the sea surface cooling due to the latent heat weakened. In addition, with the increase in the solar radiation, the sea surface heat flux changed from negative to positive, and their actions made the water column stabilized. The second factor was the improvement of light condition by deepening of euphotic layer up to or exceeding the water depth with the decrease in suspended

sediment concentration at the neap tide.

In Chapter 3, a high spatial resolution observation for sea surface chlorophyll-a concentration was newly established by the use of a Fixed-wing type Unmanned Aerial Vehicles (FUAV) equipped with two multi-spectral radiometer sensors capable of being on board for detection of upward radiance and downward irradiance in an estuary under high human influence. It can grasp the detailed spatial information about phytoplankton outbreaks in the western part of the inner Ariake Sea during winter. As a result, a robust FUAV-based remote sensing technology of retrieving sea-surface chlorophyll-a concentration based on the spectral reflectance at three wave-lengths from red to near infrared was successfully developed and validated under different hydro-meteorological conditions and different phytoplankton specie dominance for two years. We found out the patchy distribution of high chlorophyll-a concentration in the seaweed aquaculture field by the spatially high-resolution observation due to FUAV. The spatial distributions of chlorophyll-a concentration taken for two years showed that the phytoplankton proliferated locally in the central region of the western part of the inner Ariake Sea in the early stage, and then it expanded further along the northern coast.

In Chapter 4, we investigated the physical environment for chronical high concentration of phytoplankton cell in the western part of the inner Ariake Sea through the numerical simulation. The field observation data from 2000 to 2017 during autumn and winter indicated that three phytoplankton species of diatom, i.e., *Skeletonem* spp., *Eucampia zodiacus* and *Asteroplanus karianus*, were chronically high in the western area. The numerical simulation showed that the favorable environment for these species resulted from weakness of the water exchange in the western area due to low buoyancy flux.

In Chapter 5, an ecosystem model was applied to investigate the chemical-biological

environments favorable for the phytoplankton growth in the western part of the inner Ariake Sea during winter. In order to develop the ecosystem model, we incorporated the effects of the seaweed aquaculture on the surrounding environment into the model. The numerical simulation reproduced accurately the coastal biochemical environment during winter. The results concluded that the favorable conditions for phytoplankton growth in the western part were caused firstly by optimal photosynthesis environment in terms of light conditions and secondly by supply due to horizontal advection in the lower layer from offshore area.

The results from this thesis revealed that the mechanism of phytoplankton outbreaks in the western part of the inner Ariake Sea during winter was caused by two significant conditions. First, the western part of the inner Ariake Sea was the chronical high concentration of phytoplankton cell due to the weakening the strength of water exchange, optimal photosynthesis environment in terms of light conditions and supply due to horizontal advection in the lower layer from offshore area. Second, in the western area during first neap tide just after reaching the minimum water temperature, phytoplankton outbreaks occurred by stabilization of the water column due to conversion from cooling to heating in the sea surface and improvement of the underwater light condition. Therefore, this thesis suggests that phytoplankton outbreaks in the western part of the inner Ariake Sea during winter is caused by stabilization of the water column and improvement of the underwater light condition under the conditions that phytoplankton concentration is chronically high in this area.